Towards an improved treatment of unresolved cloud-radiation interaction in weather and climate models

Nina Črnivec

Munich 2020

Towards an improved treatment of unresolved cloud-radiation interaction in weather and climate models

Nina Črnivec

Dissertation
at the Faculty of Physics
Ludwig–Maximilians–University
Munich

by
Nina Črnivec
from Ljubljana, Slovenia

Munich, October 2020

First Examiner: Prof. Dr. Bernhard Mayer
Second Examiner: Prof. Dr. George Craig
Date of submission: 23.10.2020
Date of oral examination: 18.12.2020

Parts of this dissertation are contained in:

Črnivec, N. and Mayer, B. (2019). Quantifying the bias of radiative heating rates in numerical weather prediction models for shallow cumulus clouds. *Atmos. Chem. Phys.*, **19(2)**, 8083-8100, doi:10.5194/acp-19-8083-2019.

Črnivec, N. and Mayer, B. (2020a). The incorporation of the Tripleclouds concept into the δ-Eddington two-stream radiation scheme: solver characterization and its application to shallow cumulus clouds. *Atmos. Chem. Phys.*, **20(17)**, 10733-10755, doi:10.5194/acp-20-10733-2020.

Črnivec, N. and Mayer, B. (2020b). Towards an improved treatment of cloud-radiation interaction in weather and climate models: exploring the potential of the Tripleclouds method for various cloud types using libRadtran 2.0.4. *Geosci. Model Dev.*, in review.

- Chapter 1 is published in Črnivec and Mayer (2019, 2020b).
- Section 2.5 of Chapter 2 is published in Črnivec and Mayer (2020a).
- Sections 3.1 and 3.4 of Chapter 3 are published in Črnivec and Mayer (2019, 2020a,b), Section 3.2 is partly published in Črnivec and Mayer (2019, 2020a), whereas Section 3.3 is published in Črnivec and Mayer (2020b).
- Section 4.1 of Chapter 4 is published in Črnivec and Mayer (2019), whereas Section 4.2 is published in Črnivec and Mayer (2020a,b).
- Chapter 5 is published in Črnivec and Mayer (2019, 2020b).
- Chapter 6 is published in Črnivec and Mayer (2020a,b).

It should be noted that the content of Črnivec and Mayer (2019, 2020a,b) was only slightly adapted when incorporated to the present dissertation to avoid repetition and maintain clearity.

Zusammenfassung

Die Wechselwirkung zwischen Strahlung und Wolken ist eine Unsicherheitsquelle bei der numerischen Wetter- und Klimavorhersage. Wolken sind komplexe meteorologische Phänomene, die in einer immensen Vielfalt geometrischer Formen auftreten und sehr unterschiedliche Heterogenitätsgrade aufweisen. Eine physikalisch konsistente und rechenzeiteffiziente Kopplung dreidimensionaler Wolkenstrukturen mit dem solaren und thermischen Strahlungsfeld bleibt daher eine der größten Herausforderungen in der atmosphärischen Wissenschaft. Die vorliegende Arbeit zielt darauf ab, die Parametrisierung von unaufgelösten Wechselwirkungen zwischen Wolken und Strahlung für regionale und globale Modellierungsanwendungen zu verbessern.

Das erste Ziel dieser Arbeit ist die Fehlerquantifizierung der Strahlungstransportrechnung in regionalen Modellen für ein sich realistisch entwickelndes flaches Kumuluswolkenfeld. Die Abhängigkeit des Fehlers von verschiedenen Eingangsparametern der Strahlungsschemata wie dem Sonnenzenitwinkel, der Bodenalbedo, dem Wolkenbedeckungsgrad und dem Flüssigwasserweg wird untersucht. Die systematischen Fehler in der Wolkenschicht und am Boden während der Nacht beziehungsweise tagsüber werden im Detail untersucht und anhand einer hochauflösenden dreidimensionalen Berechnung bewertet. Der Schwerpunkt liegt auf der Quantifizierung des Fehlers, der sich aus zwei Hauptmängeln regionaler Modelle ergibt. Erstens, die schlechte Darstellung der unaufgelösten Bewölkung, die normalerweise als eine Abfolge horizontal homogener Schichten angenähert wird. Zweitens, die intrinsische Beschränkung eindimensionaler Strahlungsschemata, bei denen lediglich zwei Ströme zum Erfassen des aufwärts- und abwärtsgerichteten Strahlungsflusses verwendet werden, der horizontale gridskalige und subgridskalige Photonenfluss jedoch vollständig vernachlässigt wird. Es ist unklar, welche Fehlerquelle auf der Skala der regionalen Modellierung dominiert, auf der sich vielfältige Probleme überschneiden. Deshalb wird gleichzeitig der Fehler bewertet, der sich aus dem zweiten Hauptmangel ergibt. Die Ergebnisse unterstreichen die Bedeutung einer verbesserten Darstellung von Wolken schon auf der regionalen Skala.

Das zweite Ziel der vorliegenden Arbeit besteht darin, die Parametrisierung der Wolken-Strahlung-Wechselwirkung in globalen Modellen mit grober Auflösung zu verbessern, wobei die mangelhafte Darstellung der horizontalen Inhomogenitäten von Wolken im Fokus liegt. Dieses Thema wird mit dem hochmodernen Tripleclouds-Strahlungstransportlöser angegangen, dessen grundlegendes Merkmal die Einteilung der Wolke in einen optisch dickeren und einen optisch dünneren Bereich ist. Die Herausforderung besteht darin,

das Wolkenkondensatpaar, das die beiden wolkigen Regionen charakterisiert, und die entsprechende geometrische Aufteilung der Schichtbewölkung optimal einzustellen. Für die Analyse wurde ein vielfältiger Wolkendatensatz gesammelt, der Fallstudien von Kumulus, Stratokumulus, Zirrus und Kumulonimbus umfasst. Primäres Ziel ist es, die Schätzung der globalen Wolkenvariabilität zusammen mit verschiedenen Annahmen zur Kondensatverteilung auf ihre Gültigkeit zu testen. Anschließend werden komplexere Parametrisierungen evaluiert, die die Behandlung von bedeckter Szenen sowie extrem heterogener Bewölkung optimieren. Die Strahlungsdiagnostik, welche die atmosphärische Heizrate und den Nettobodenfluss einschließt, wird erstmals konsequent mit der Tripleclouds-Methode untersucht. Die Leistung von Tripleclouds übertrifft die herkömmliche Berechnung mit horizontal homogener Bewölkung meist erheblich. Der Effekt des horizontalen Photonentransports wird zusätzlich quantifiziert. Die allgemeinen Schlussfolgerungen sind für jeden untersuchten Wolkentyp grundsätzlich verschieden. Das regt zu Bemühungen an, die vom Wolkenregime abhängigen Methoden für die Verwendung in atmosphärischen Modellen der nächsten Generation zu verbessern.

Der größte technische Aufwand der vorliegenden Arbeit bestand in der Entwicklung der klassischen Zweistrommethode für homogene partielle Bewölkung und ihrer anschließenden Erweiterung um das Tripleclouds-Konzept. Beide Algorithmen wurden in die Strahlungsbibliothek *libRadtran* implementiert und stehen somit zur weiteren Entschlüsselung wissenschaftlicher Fragestellungen im Hinblick auf das Zusammenspiel von Wolken und Strahlung bereit.

Abstract

The interaction between radiation and clouds represents a persistent source of uncertainty in numerical weather and climate prediction. Clouds are inherently complex meteorological phenomena, appearing in an immense variety of geometrical shapes and exhibiting highly variable degrees of heterogeneity. A physically consistent and computationally efficient coupling of three-dimensional cloud structures with the solar and thermal radiative field thereby remains one of the greatest challenges in the atmospheric science community. The present thesis aims to make progress towards an improved treatment of the unresolved cloud-radiation interchange for both regional and global modeling applications.

The first dissertation objective is to quantify the radiative bias in regional models for a realistically evolving shallow cumulus cloud field. The bias dependence on various input parameters of radiation schemes such as solar zenith angle, surface albedo, cloud cover and liquid water path is examined. Nighttime and daytime biases within the cloud-layer and at the surface are thoroughly investigated and evaluated against a high-resolution three-dimensional benchmark computation. The focus is laid on quantifying the regional-scale model bias arising from two chief shortcomings. First, the poor representation of unresolved cloudiness, which is normally approximated as a series of horizontally homogeneous partially cloudy layers. Second, the intrinsic constraint of one-dimensional radiation schemes, employing merely two streams for capturing the upward and downward radiative flux, but entirely neglecting the grid- and subgrid-scale horizontal photon flow. Since it is unclear which error source is dominant at the scale of regional modeling where these multiple issues intersect, the bias stemming from the latter drawback is simultaneously assessed. The principal findings highlight the importance of an improved cloud representation even at the regional scale.

The second dissertation objective is to advance the cloud-radiation interaction parameterization in coarse-resolution global models, focusing on the issues related to misrepresentation of cloud horizontal inhomogeneity. This subject is tackled with the state-of-the-art Tripleclouds radiative solver, the fundamental feature of which is the inclusion of the optically thicker and thinner cloud fraction. The research challenge is to optimally set the pair of cloud condensates characterizing the two cloudy regions and the corresponding geometrical split of layer cloudiness. A diverse cloud field data set was collected for the analysis, comprising case studies of cumulus, stratocumulus, cirrus and cumulonimbus. The primary goal is to test the validity of global cloud variability estimate along with various condensate distribution assumptions. More sophisticated parameterizations are subsequently explored,

optimizing the treatment of overcast as well as extremely heterogeneous cloudiness. The radiative diagnostics including atmospheric heating rate and net surface flux are for the first time consistently studied using the Tripleclouds method. The performance of Tripleclouds mostly significantly surpasses the conventional calculation on horizontally homogeneous cloudiness. The effect of horizontal photon transport is further quantified. The overall conclusions are intrinsically different for each particular cloud type examined, encouraging endeavors to enhance the use of cloud regime dependent methodologies in next-generation atmospheric models.

The major technical effort undertaken within the scope of this work was the design of the classic two-stream radiation scheme supporting homogeneous partial cloudiness and its subsequent extension to incorporate the Tripleclouds concept. Both algorithms were implemented in the *libRadtran* radiative library, promoted to be utilized for further unraveling of key scientific mysteries related to cloud-radiation interplay.

Contents

Chapter 1

Introduction

1.1 Background and motivation

The fundamental role of clouds and their interaction with radiation in weather and climate can hardly be overemphasized (e.g., Randall et al., 2007; Boucher et al., 2013; Stevens and Bony, 2013; Bony et al., 2015; Schneider et al., 2017). Clouds are complex phenomena, since they exhibit an immense variety of shapes and sizes (Randall et al., 2003) and highly variable degrees of inhomogeneity (Shonk et al., 2010; Hill et al., 2012, 2015; Boutle et al., 2014; Ahlgrimm and Forbes, 2016, 2017). When interacting with solar and thermal radiation, the most common effects are radiatively induced cooling at cloud top and warming at cloud base, which promotes convective instabilities within the cloud (Webster and Stephens, 1980). This radiative destabilization of the cloud layer is impelled primarily by thermal radiation, whereas during daytime solar radiation generally has a stabilizing tendency, albeit the latter strongly depends on solar zenith angle (Črnivec and Mayer, 2019). In the bottommost part of the troposphere, called the planetary boundary layer, the atmosphere and thereby clouds are directly influenced by the presence of the Earth's surface, via the transition of heat, moisture and momentum (Baur et al., 2018). The net (difference between downward and upward) surface radiative flux is a key component of surface energy budget (Manabe, 1969). Although solar surface flux is customarily markedly larger than its thermal counterpart and thus mostly dominates during daytime (Črnivec and Mayer, 2019), the latter is important during nighttime when solar forcing is absent. All in all, radiatively induced temperature changes in clouds and at the surface are firmly linked to a broad range of atmospheric moist thermodynamic, turbulent and microphysical processes, e.g. formation of precipitation (Harrington et al., 2000; Klinger et al., 2019). A skillful representation of these processes in numerical models as well as of their mutual interplay still poses many grand challenges to atmospheric scientists across the world (Stevens and Bony, 2013; Schneider et al., 2017) (Fig. 1.1).

The present dissertation aspires to make progress on the treatment of unresolved cloud-radiation interaction in regional and global weather and climate models. The latter global models are often referred to as the large-scale atmospheric models (LSAMs) or general

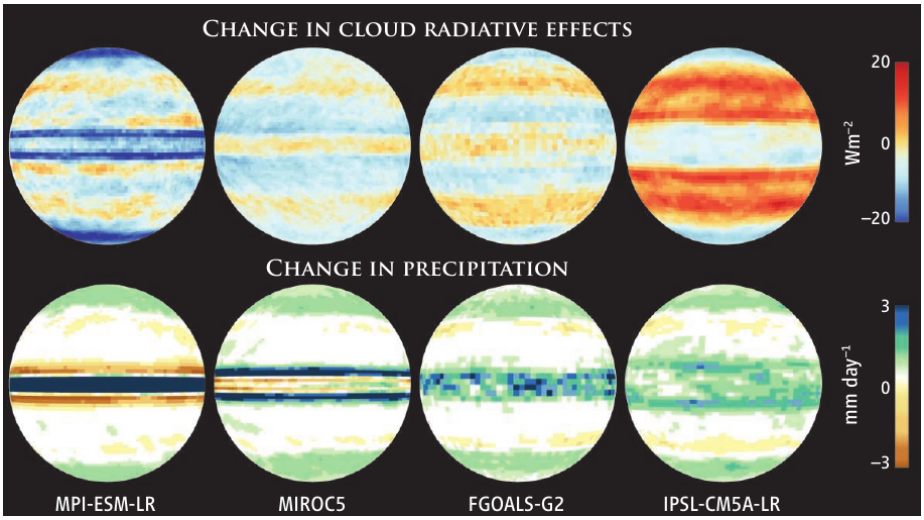

Figure 1.1: *Inadequate representation of the broad spectrum of cloud processes is recognized as the major source of uncertainty in climate model projections. This uncertainty underlies wide variation in the response of the climate system to warming: shown are changes in cloud-radiative effects (top row) as well as in precipitation (bottom row) accompanying a warming of 4˚C for four models from the Coupled Model Intercomparison Project (Phase 5; CMIP5). Source: Stevens and Bony (2013).*

circulation models (GCMs), commonly abbreviated as GCMs in the remainder of this work. Despite significant advances in the last few decades, the radiation schemes of these coarse-resolution models still only crudely represent the interchange between clouds and radiation, being impaired by the poor representation of model cloudiness itself in the first place (Randall et al., 2003). A handy way to tackle the above-mentioned shortcomings is by means of explicit cloud modeling. Over the past decades, large-eddy simulation (LES) and cloud-resolving models (CRMs) (e.g., Klemp and Wilhelmson, 1978; Tao and Simpson, 1993; Khairoutdinov and Randall, 2003; Stevens et al., 2005) have established themselves as a well-acknowledged tool in cloud physics research (Guichard and Couvreux, 2017). Apart from unresolved cloud microphysics, these models claim to resolve macrophysical cloud structures and are therefore a trusted tool to discover missing puzzle pieces for weather and climate models. The idea of the so-called superparameterization (Grabowski, 2001, 2003), where a two-dimensional (2-D) CRM is embedded in individual column of a host GCM model, has recently been revisited by applying fully three-dimensional (3-D) LES model as a superparameterization, albeit on massively parallel computers (Grabowski, 2016). Short-term global predictions using direct LES/CRM simulations extending up to a few months or even years are beginning to be feasible (Bretherton and Khairoutdinov, 2015). Long-term climate projections utilizing coupled atmosphere-ocean systems in a direct high-resolution mode, however, will not be possible for a next couple of decades even on most powerful supercomputers (Schneider et al., 2017). Similarly, despite remarkable advancements in numerical weather prediction (NWP), which is burdened by the users'

demand for real-time forecasts, both global and regional NWP at a subkilometer scale will stay challenging in the near future (Bauer et al., 2015).

Bearing the above-mentioned limitations in mind, there remains an ongoing joint scientific effort to improve traditional physical parameterization schemes, which lie at heart of every weather and climate model. To that end, LES and CRM models provide valuable high-resolution 3-D cloud field data, on which cloud-radiation interplay can be studied either offline (e.g., Jakub and Mayer, 2015; Klinger and Mayer, 2014, 2016; Črnivec and Mayer, 2019) or interactively (e.g., Jakub and Mayer, 2016, 2017; Klinger et al., 2017; Hartmann et al., 2018). In addition, stochastic cloud models (STMs), capable of quickly generating realistic 3-D cloud structures were developed by cloud modeling communities worldwide (e.g., model introduced by Di Giuseppe and Tompkins, 2003a for stratocumulus; Evans and Wiscombe, 2004 for cumulus; Hogan and Kew, 2005 for cirrus). Whereas the disadvantage of stochastic models compared to LES or CRMs might be that interactive studies of cloud-radiative feedbacks are not possible, our present work is restricted to offline radiative transfer experiments, based on high-resolution cloud field data stemming from diverse LES, CRM and STM models.

A number of studies took advantage of this approach in the past. They often compared offline radiative transfer experiments performed on a pregenerated well-resolved cloud field (Fig. 1.2, top right panel) including the exact 3-D radiation calculation (such as computationally expensive Monte Carlo technique, Mayer, 2009; or SHDOM, Evans, 1998), the Independent Column Approximation (ICA; Stephens et al., 1991), where the radiative transfer problem is solved in each vertical grid column separately, and the one-dimensional (1-D) GCM-type radiation calculation. The latter was carried out on the derived horizontally homogeneous cloud representation, where fractional cloudiness was assumed to overlap vertically in accordance with the maximum-random rule (Geleyn and Hollingsworth, 1979; Tian and Curry, 1989) − a configuration which persisted in the majority of GCMs for many decades (Fig. 1.2, bottom left panel). The disparity between the latter conventional GCM calculation and the 3-D benchmark was used to assess the overall bias of GCM radiative quantities. The comparison between the ICA and 3-D experiment served to quantify the portion of the overall bias stemming from neglected horizontal photon transport, whereas the comparison between the conventional GCM configuration and the ICA measured the bias associated with neglected subgrid cloud variability.

In this way the radiative transfer was extensively studied for cumulus (Davies, 1978; Kobayashi, 1988; Welch and Wielicki, 1989), stratocumulus (Cahalan et al., 1994a,b; Cahalan et al., 1995; Zuidema and Evans, 1998; Di Giuseppe and Tompkins, 2003a), cirrus (Fu et al., 2000a; Carlin et al., 2002; Hogan and Kew, 2005; Zhong et al., 2008; Fauchez et al., 2014) as well as deep convective and anvil clouds (Barker et al., 1999; Fu et al., 2000b; Di Giuseppe and Tompkins, 2003b, 2005; Tompkins and Di Giuseppe, 2003), although some of the earliest work used either very idealized cuboid, single-layered or 2-D clouds. Moreover, some of these studies assessed solely either the ICA or the subgrid cloud variability bias and therefore did not shed any light on their relative contribution. Nevertheless, it was commonly found that classic 3-D radiative effects associated with horizontal photon flow manifest most pronouncedly in regions characterized by notable horizontal

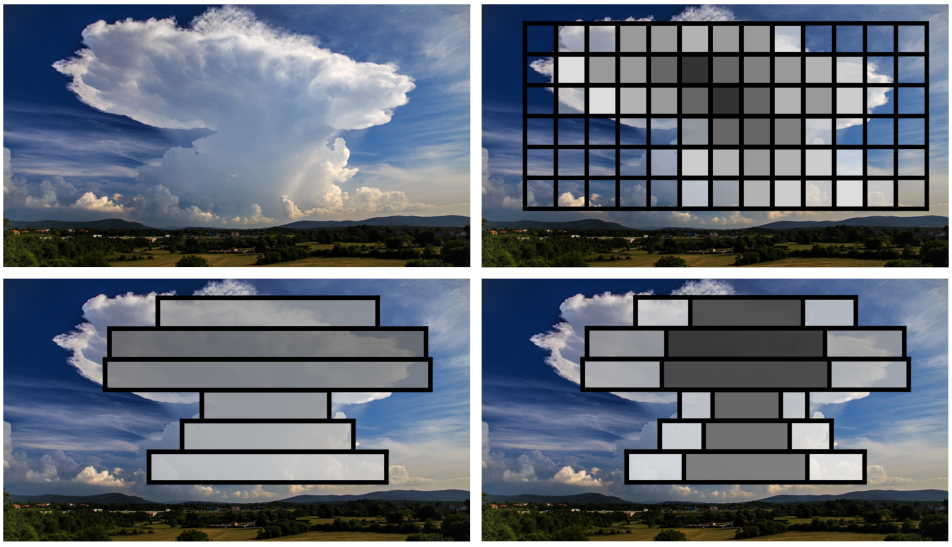

Figure 1.2: *Top left: an explosive storm near Divača, Slovenia (Marko Korošec Weather Photography). Top right: a representation of such storm in a cloud-resolving model (lighter/darker grey shading denotes smaller/larger optical thickness). Bottom left: a traditional storm representation in coarse-resolution weather and climate models. Bottom right: the state-of-the-art Tripleclouds methodology.*

gradients of optical properties and are thus regularly related to cloud side boundaries. But also the in-cloud horizontal variations of optical depth were found to impact the 3-D radiative transfer and especially the GCM-type approximation. Due to aforementioned reasons, conflicting claims can be found in the literature regarding the magnitude and sign of these biases. Better understanding of these effects is required in order to advance the parameterization of cloud-radiation interaction.

Another important issue is the resolution dependence of the two error sources. There is a general consensus within the experienced radiative transfer community that classic 3-D radiative effects become increasingly more important as the model resolution progresses, whereas the issues arising from unresolved cloudiness concurrently naturally diminish. Thus in vast climate model grid boxes extending for several hundreds of kilometers, the unresolved cloud variability is recognized as the dominant error source, whereas the effect of horizontal photon flow is frequently assumed to be negligible. Contrarily, in high-resolution research modeling, where cloud structures are considered as resolved, the subgrid cloud variability bias vanishes and solely the problematic related to neglected horizontal photon transport remains to be tackled. In between these two extremes there lies atmospheric modeling at the regional scale, where these multiple issues intersect, and it is unclear, which error source is prevailing at this scale. Until now this scale has not received much attention, since various intersecting problems are especially challenging to solve. Better knowledge and quantification of regional-scale bias sources is desired to proceed the cloud-radiation interchange parameterization.

1.2 Scientific objectives and scope of this work

This dissertation endeavours to take two important steps paving the way towards an improved treatment of the unresolved cloud-radiation interaction in weather and climate models for both regional- and global-scale modeling applications. The corresponding scientific objectives and aims are more specifically outlined in the subsequent paragraphs.

Regional-scale modeling research subject tackling shallow cumulus clouds

Although the uncertainty related to the inaccurate treatment of radiation-cloud interaction in numerical models depends, inter alia, on cloud type, the study tackled within the first part of this dissertation is restricted to shallow cumulus clouds. The importance of shallow convection for the redistribution of atmospheric heat and moisture is well acknowledged (e.g., Albrecht et al., 1988, 1995a; Tiedtke, 1989; Zhao and Austin, 2005). Small-scale fluctuations in microphysical, dynamical and thermodynamical parameters observed in boundary layers containing cumuli (Austin et al., 1985) indicate the complexity of a proficient coupling of cumulus cloud fields with a full 3-D radiative field.

As indicated in the preceding section, the LES models have become an important tool in boundary layer research (Neggers et al., 2003). If an accurate 3-D radiation (e.g., Monte Carlo) calculation is performed on 3-D highly resolved LES cumulus cloud, which is considered to be the best proximity for the 3-D cloud-radiation interaction occurring in the real world ("benchmark experiment" or "truth"), the following is observed. In the solar spectral range, the largest heating is at the illuminated cloud side and the shadow of the cloud at the ground is shifted according to solar zenith angle (Wapler and Mayer, 2008; Wissmeier et al., 2013; Jakub and Mayer, 2015, 2016). In the thermal spectral range, there is a strong cooling of cloud top and cloud sides and modest warming of cloud bottom (Kablick et al., 2011; Klinger and Mayer, 2014, 2016). In the associated ICA approximation, which suppresses the horizontal photon flow, the 3-D radiative effects mainly related to cloud sides are misrepresented; the chief shortcomings are as follows. In the solar spectral range the heating is always at cloud top and the shadow at the surface lies directly underneath the cloud, which is fundamentally wrong unless the Sun is at zenith (Jakub and Mayer, 2015, 2016). In the thermal spectral range, the ICA approximation only captures cloud top cooling and cloud base warming, but entirely neglects the cooling of cloud sides (Kablick et al., 2011; Klinger and Mayer, 2014, 2016). When fast and sufficiently accurate 3-D radiation parameterizations for resolved scales are coupled to an LES model, the above-mentioned shortcomings of ICA on the cumulus cloud evolution can be studied. Jakub and Mayer (2017), as an illustration, showed that interactive 3-D solar radiative transfer may induce formation of cloud streets similar to the known roll clouds caused by wind shear, whereas the ICA approximation produces randomly positioned clouds. In a recent study by Klinger et al. (2017) it was shown that interactive 3-D thermal radiation affects cloud circulation by enhancing cloud-core updrafts and surrounding subsiding shells. In addition, it alters the organization of clouds (convective self-aggregation).

As previously suggested we are presumably at least a decade away from the desired

resolution before these effects can be directly simulated within regional NWP and climate modeling. Today's regional (limited-area) models with horizontal grid spacing on the order of few kilometers – $\mathcal{O}(1-5$ km) (e.g., the operational model of German Weather Service in its convection-permitting configuration COSMO-D2 with grid spacing of 2.2 km) mostly resolve deep convection and have a parameterization for shallow convection. Depending on cloud parameterization scheme, subgrid-scale cloudiness (cloud fraction) within a model grid box is usually diagnosed from the grid-scale relative humidity (Sundqvist et al., 1989; Quaas, 2012). Shallow cumulus clouds in state-of-the-art regional atmospheric models are thus represented as horizontally homogeneous layers of partial cloudiness, entirely missing their 3-D geometrical structure and small-scale variability of optical properties. Further, an assumption is required of how partial cloudiness is distributed in the vertical direction, which is generally another deficiency of radiation schemes (Barker et al., 2003; Barker, 2008; Wu and Liang, 2005). The widely employed assumption is the aforementioned maximum-random overlap (Geleyn and Hollingsworth, 1979), which, implemented in the two-stream framework, gives the so called two-stream method with maximum-random overlap assumption for partial cloudiness (Ritter and Geleyn, 1992), commonly used as regional model radiation solver. The principal property of the analytical computationally efficient 1-D two-stream solver is the usage of solely two directional streams capturing the upward and downward radiative flux, whereby the horizontal photon transport is intrinsically neglected.

To summarize, the interaction between radiation and shallow cumulus clouds represents a source of uncertainty in regional numerical models due to both intrinsic problems of 1-D radiation schemes neglecting horizontal photon transport at a grid-scale and subgrid-scale level and poor representation of unresolved clouds. The underlying questions of the present study are as follows. How large is the radiative bias of atmospheric heating rate and net surface flux in regional models for shallow cumulus clouds? How does this bias depend on various input parameters of radiation schemes, such as solar zenith angle (SZA), surface albedo (A), cloud cover (CC) and cloud liquid water path (LWP)? Further, how much of this bias is stemming directly from the neglected horizontal photon transport? The latter question is highly relevant, since broken shallow cumulus cloud fields generally exhibit a considerable amount of cloud side area, where the horizontal photon transport most markedly comes into play. Systematic quantification of radiative biases as well as physical understanding of their origins is a necessary first step towards an improved treatment of cloud-radiation interaction in regional atmospheric models. To the author's knowledge, this is the first study that assesses radiative biases for a realistically evolving shallow cumulus cloud field at the scale of regional models for atmospheric heating rate and net surface flux consistently as a function of a wide range of parameters governing the radiative transfer.

The experiments are performed with the offline stand-alone radiative transfer package *libRadtran* (Mayer and Kylling, 2005; Emde et al., 2016), the main advantage of which is the accurate 3-D benchmark radiative model. At the time when the author of this dissertation started her doctoral studies, however, no radiative solver representative of those currently used in regional-scale models was available in *libRadtran*. Therefore the classic δ-Eddington two-stream method was extended to support partial cloudiness for the purpose of this research subject.

Global-scale modeling research subject tackling various cloud types

The second aspect of this dissertation aims to reinforce earlier studies by establishing 3-D benchmarks and further exploring the validity of ICA for various cloud types at the scale of GCMs. In particular, we intend to assess the ICA suitability when the GCM resolution refines to the mesoscale – $\mathcal{O}(10-100$ km). Di Giuseppe and Tompkins (2003b), as an illustration, showed that 3-D radiative effects increase as the GCM resolution approaches the mesoscale. In addition, we strive to investigate more realistic cloud morphologies, as we apply finer horizontal grid spacing in cloud-generating models compared to the previous research (e.g., Di Giuseppe and Tompkins, 2003b; Hogan and Kew, 2005; Zhong et al., 2008). Furthermore, we aim to consistently analyze atmospheric heating rate and net surface flux, which has received considerably less attention in the previous debates.

The novelty and therefore the prime focus of the current work, however, is the utilization of the state-of-the-art Tripleclouds (TC) radiative solver for use in coarse-resolution weather and climate models. The TC method was primarily suggested by Shonk and Hogan (2008) (hereafter abbreviated as SH08) and operates with two regions in each vertical model layer to represent the cloud: one region represents the optically thicker part of layer cloudiness, while the other region represents the remaining optically thinner part. The added value of the Tripleclouds scheme compared to its conventional GCM predecessor is thus the capability of accounting for horizontal cloud heterogeneity in the simplest possible and therefore computationally efficient manner. Following the idea of SH08, a second cloudy region has been incorporated into the δ-Eddington two-stream method with maximum-random overlap assumption for partial cloudiness within the scope of this thesis. The inclusion of a second cloudy region in the two-stream framework requires an extension of vertical overlap rules. This task was accomplished exploiting the core-shell model for convective clouds (Heus and Jonker, 2008; Heiblum et al., 2019), where the convective core associated with updrafts and condensate loading is located in the geometrical center of the cloud, surrounded by the shell associated with downdrafts and condensate evaporation. In the terminology of radiative transfer, the maximum-random overlap is thus retained for the entire fractional cloudiness and additionally applied for optically thicker part of the cloud. This vertical overlap formulation implicitly places the optically thicker cloudy region towards the interior of the cloud in the horizontal plane, while the optically thinner region resides at cloud periphery, as depicted in Fig. 1.2 (bottom right panel).

An important purpose of the present study is to present our version of the Tripleclouds scheme and its subsequent implementation in *libRadtran*. The another major aim is to evaluate the TC method by examining case studies of cumulus, stratocumulus, cirrus and cumulonimbus, since cloud horizontal heterogeneity strongly depends on cloud type (Pincus et al., 1999; Oreopoulos and Cahalan, 2005; Shonk et al., 2010; Shonk and Hogan, 2010; Hill et al., 2012, 2015; Boutle et al., 2014; Ahlgrimm and Forbes, 2016, 2017). These cloud field case studies are deliberately chosen in a way, that cloud vertical arrangement tends towards the assumed maximally-overlapped scenario, thus focusing on radiative effects associated with cloud horizontal inhomogeneity and eliminating the error arising from the misrepresentation of assumed vertical overlap as would be expected to occur in conditions

with strong vertical wind shear (Naud et al., 2008; Di Giuseppe and Tompkins, 2015).

Once two-stream radiative fluxes are imposed onto a system of three-region atmospheric layers in accordance with vertical overlap rules, the research challenge is to optimally set the pair of liquid/ice water content characterizing the two cloudy regions and the corresponding geometrical split of layer cloudiness. The answer to the posed scientific question is critically dependent on the characteristic of the underlying subgrid cloud horizontal variability. The latter is conveniently defined in terms of the fractional standard deviation (FSD) of cloud liquid/ice condensate as well as the shape of its distribution. Since this information is generally not available in GCMs, Shonk et al. (2010) derived a global FSD estimate based upon diverse cloud observational studies (Cahalan et al., 1994a; Barker et al., 1996; Pincus et al., 1999; Smith and Del Genio, 2001; Rossow et al., 2002; Hogan and Illingworth, 2003; Oreopoulos and Cahalan, 2005; SH08). The prime objective of the present study is to assess the validity of the global FSD estimate in the TC radiative solver for four inherently contrasting cloud types in conjunction with various assumptions for the subgrid cloud condensate distribution, which are commonly applied in cloud modeling (Gaussian, gamma, lognormal). Along the above lines, a further goal of the study is to inspect the actual in-cloud water content distribution based on high-resolution LES/CRM data, as this is the keystone for a well-designed self-consistent TC parameterization. The majority of previous studies examining the cloud condensate distribution, namely, adopted cloud data simulated on smaller domains with coarser horizontal grid spacing. The final aim of the study is to explore more sophisticated FSD parameterizations, characterizing systematic departures from the global mean. These refined TC configurations refer to distinctive improvements desired in the case of overcast as well as extremely heterogeneous cloud scenarios. All in all, this work presents the first usage of Tripleclouds to consistently study the atmospheric heating rate and net surface flux.

1.3 Dissertation outline

The remainder of this thesis is structured as follows. Chapter 2 commences with the scientific background highlighting the role of radiation and clouds in numerical weather and climate prediction. Some theoretical concepts on the model representation of clouds, atmospheric radiation as well as of their mutual interplay, that were briefly touched upon in the preceding introductory section, are further elucidated. In the subsequent Chapter 3 the cloud field data, radiative transfer models as well as experimental design of radiation calculations is introduced. The focus is laid on the characterization of both two-stream solvers, which were constructed within the scope of this thesis: the δ-Eddington two-stream method with maximum-random overlap and its upgrade referred to as the Tripleclouds radiation scheme, which represents the major technical challenge accomplished. The results of the radiative transfer experiments at the scale of regional and global models are thoroughly discussed in Chapter 4. Summary and concluding remarks are given in Chapter 5. Finally, some interesting ideas for the extension of the present work building upon the main findings gained and utilizing tools developed herein are suggested in Chapter 6.

Chapter 2

Scientific Background

2.1 A preface on weather and climate

Life on Earth has ever since been influenced by weather and climate. *Weather*, a short-term state of the atmosphere on time scales of a few hours to several days, comprises a vast range of various meteorological phenomena: from casual sunny or rainy days, affecting human decision making on a daily basis, to rarer but hazardous high-impact weather events (Craig et al., 2010), posing a serious threat to human life and prosperity. Similarly, a longer-term mean state of weather − generally an average over a few decades (30 years) − or *climate* exerts a profound influence on the evolution of mankind (and vice versa; Lüthi et al., 2008; Neokum et al., 2019b,a). In the last few decades, changes of climate are faster than ever, bringing many devastating consequences to planet Earth, if not handled properly (IPCC, 2014, 2018). Accurate weather and climate predictions are therefore of fundamental importance for comfort and welfare of today's and future generations.

Radiation, the ultimate driver of weather and climate

The ultimate driver of global atmospheric and oceanic circulation is the radiation stemming from the Sun and entering the Earth's atmosphere at its top. Sun heats the Earth differentially, meaning that the equatorial tropical areas receive more heat than the polar regions. The resulting temperature gradient between the tropics and the poles is the largest at midlatitudes. This drives the atmosphere away from its balanced state by the process referred to as the baroclinic instability. All global winds, associated cloud systems and weather patterns strive to bring the atmosphere back towards its equilibrium, transporting the surplus heat from the equatorial to polar regions. Since the Earth's atmosphere is a complex, non-linear, chaotic, multi-scale system, the precise nature of its response to the differential solar heating is by no means trivial.

2.1.1 Numerical weather and climate prediction

Simulating weather and climate is a challenging task. Continuous behavior of the atmosphere needs to be discretized in space and time (Fig. 2.1). The heart of every weather and climate model is its dynamical core, consisting of the governing equations (Bauer et al., 2015), based on conservation principles of momentum, mass and thermodynamic energy. For a given initial atmospheric state, defined on a finite grid mesh, this fundamental equation set is integrated forward in discrete time steps to generate future weather and climate scenarios. The grid mesh size, determining the model spatial resolution, is closely tied to the integration time step, controlling the model temporal resolution (to ensure numerical stability finer grids generally require shorter integration time steps). So what eventually directs the model resolution?

In practice, there are many factors affecting the choice of model resolution: the spatial domain extent, the length of the integration, the availability of computational resources as well as the efficiency and complexity of the employed numerical model. Broadly speaking, global climate models simulating future scenarios for a few decades or even centuries ahead use a horizontal grid mesh size of about 50 to 300 km. Global operational weather models that run for days to weeks employ horizontal grid mesh sizes of about 10 to 50 km[1], whereas regional (limited-area) weather forecast models utilize finer horizontal grid box sizes of 1 to 5 km typically[2].

2.1.2 Resolved versus unresolved scales

Atmospheric processes span a wide range of temporal and spatial scales. As a rule of thumb, it takes at least eight grid points to represent any wave-like feature (Stensrud, 2007 and references therein) and the process is considered to be explicitly *resolved* by the dynamical core equations. Physical processes occurring on smaller scales are referred to as being *unresolved* and need to be parameterized. Similarly, processes that are too complex to be directly represented by the governing equations have to be parameterized. This is achieved by the physical parameterization schemes (Stensrud, 2007; Warner, 2011). The primary task of the latter is therefore to represent the impact of unresolved scales on resolved variables. Some typical processes requiring parameterization in weather and climate models are clouds, radiation, turbulence and surface processes. A larger scope of these processes is illustrated in Fig. 2.3. Physical parameterizations generally operate either in individual grid boxes or grid columns (Fig. 2.2) of a host dynamical model, which is highly desirable for parallel machines. A specific parameterization scheme within a host atmospheric model frequently serves several purposes, interacting also with other parameterizations. A

[1]Current global weather forecast models and their operational horizontal grid mesh sizes: ECMWF-IFS (European, HRES $\sim$ 9 km, ENS $\sim$ 18 km); ICON (German, $\sim$ 13 km); UKMO (British, $\sim$ 17 km); GFS (American, $\sim$ 22 km); GEM (Canadian, $\sim$ 22 km); ARPEGE (French, $\sim$ 46 km).

[2]Regional weather forecast models and their operational horizontal grid mesh sizes: COSMO-D2 (German model, 2.2 km); COSMO-DE (former German model, in service until recently, 2.8 km); ALADIN-SI (Slovenian model, 4.4 km).

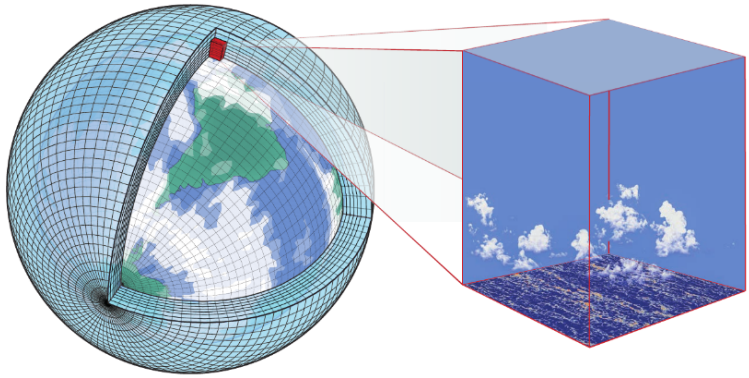

Figure 2.1: *Grid cells in a global weather or climate model (left schematic) and an illustration of the possible subgrid phenomena occurring within an individual grid cell (right schematic): shown is a large-eddy simulation of shallow cumulus clouds at 5 m resolution. The color shading at the ground indicates the buoyancy of near-surface air, which fuels shallow convection. Source: Schneider et al. (2017).*

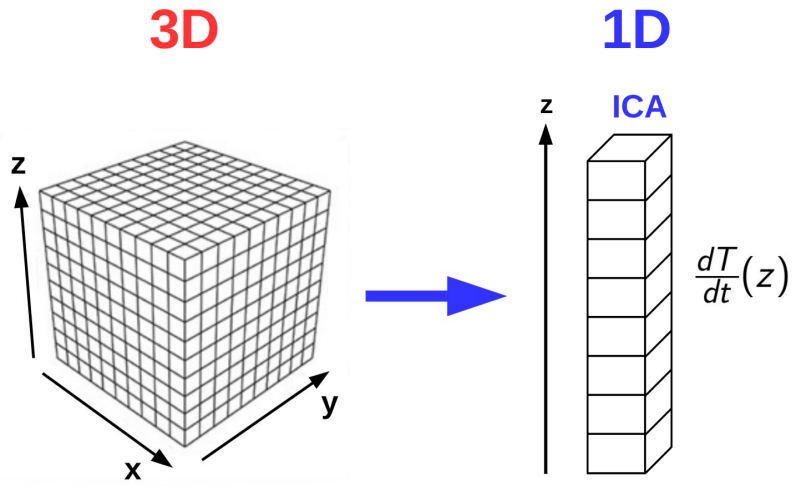

Figure 2.2: *The concept of the Independent Column Approximation (ICA), which is the basis for radiative transfer parameterization (e.g., heating rate calculation). The main difference between global- and regional-scale modeling in this respect: the assumption that individual vertical domain columns might be treated independently is adequate for global model horizontal grid mesh sizes of 10 km and more. In regional modeling, on the contrary, the 3-D radiation parameterization should in principle account for horizontal radiative transport within each individual column as well as between the various columns across the domain (at both subgrid and grid-scale level).*

radiation parameterization scheme, for example, accomplishes a twofold task: apart from the calculation of the radiative heating rate distribution within the atmosphere entering the diabatic heating term in the prognostic temperature equation, it supplies the net surface radiative flux for the proper evaluation of the surface energy budget. The present

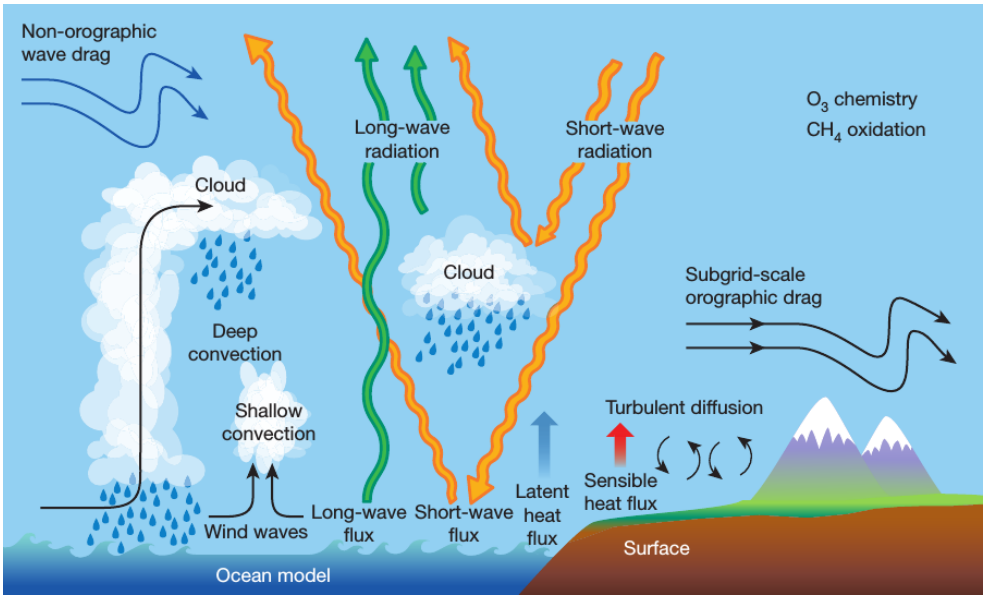

Figure 2.3: *Schematic depicting a broad range of physical processes that occur on small scales and generally require parameterization in weather and climate models. Source: Bauer et al. (2015).*

thesis aims at improving model treatment of unresolved cloud-radiation interaction. To that end, the challenges regarding the cloud and radiation parameterization are outlined briefly hereafter.

Cloud parameterization

Undoubtedly, parameterization of clouds is one of the toughest tasks in the present atmospheric science community (e.g., Randall et al., 2003; Arakawa, 2004; Stevens and Bony, 2013; Schneider et al., 2017). The cloud parameterization problem is often referred to as being "deadlocked" (Randall et al., 2003), in the sense that despite putting a tremendous effort into it, the rate of progress is immensely slow. There are multiple reasons why properly handling clouds in weather and climate models is so burdensome. Firstly, clouds are *complex* (a glimpse into admirable cloud diversity is given by the photographies in Fig. 2.4): cloud processes occur on a variety of temporal and spatial scales, ranging from the cloud particle scale at $\mathcal{O}$ (1 μm), through the scale of individual clouds at $\mathcal{O}$ (1 km), to the scale of cloud systems at $\mathcal{O}$ (100 km). Depending on the resolution thus larger cloud systems can partially be explicitly represented on the model grid, whereas the major component of cloud-related processes generally requires parameterizations. Secondly, clouds are *unknown*. Due to their overwhelming complexity, a vast portion of cloud processes still remains unknown (Randall et al., 2003).

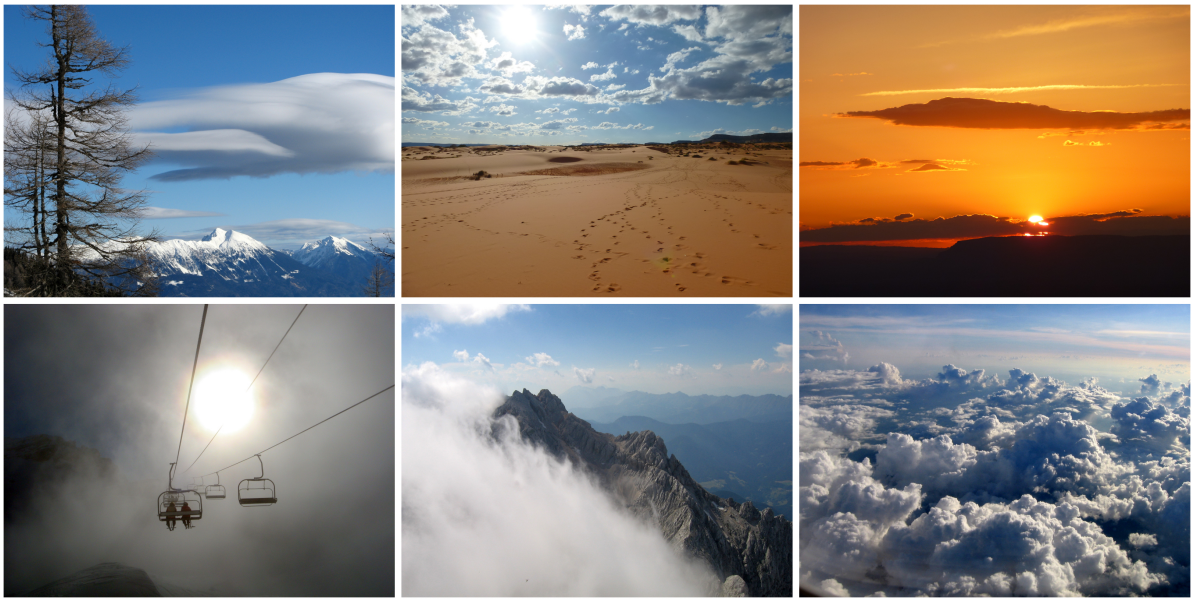

Figure 2.4: *Photographies highlighting diverse cloud phenomena across the globe, demonstrating the complexity of three-dimensional cloud-radiation interaction occurring in the real world.*

Radiation parameterization

The interaction of radiation with the atmosphere occurs at a molecular scale and always requires parameterization in numerical models regardless of the resolution. In principle, for a given atmospheric state the radiative processes are *known in detail*, but parameterizing them exactly would imply enorm computational cost, which is not affordable within constraints of numerical weather and climate prediction. One challenge when parameterizing radiation is therefore to reduce the complexity of radiative transfer problem with a minimal loss of accuracy, whereby correlated-k methods (e.g., Mlawer et al., 1997) are commonly employed to facilitate the spectral integration. The another great challenge of radiation parameterization schemes is related to their treatment of unresolved cloudiness (e.g., Randall et al., 2003, Hogan et al., 2017). This is the key challenge that will be tackled within this thesis.

Epilogue

This dissertation aims to provide the theoretical foundation for an improved treatment of unresolved cloud-radiation interaction in weather and climate models. In order to accomplish this task, the underlying knowledge about clouds as well as their representation in numerical models is required and is outlined in Section 2.2. Similarly, the necessary atmospheric radiative transfer theory is established in Section 2.3. The cloud-radiation interaction is addressed in Section 2.4. The treatment of unresolved cloud inhomogeneity in model radiation parameterization schemes is further reviewed in Section 2.5.

2.2 Clouds

This section first demonstrates the diversity of clouds occuring in the real atmosphere, which makes their representation in numerical models, as explained subsequently, such a demanding task. If not stated otherwise, the following description is based mainly on the books of Houze (1993), Lamb and Verlinde (2011), Warner (2011) and Lohmann et al. (2016).

2.2.1 Clouds in the real atmosphere

Clouds are striking features in the sky and always interesting to look at. Trailing a definition for a cloud, however, which is a synonym for complexity in the meteorological community, might not be straightforward. In simple words, a cloud is a mixture of liquid droplets, ice crystals and aerosol particles suspended in the atmosphere. Whereas the background clear-sky molecules preferentially scatter the blue light, the larger cloud particles more equally scatter the sunlight spectrum, making it possible to observe clouds visually, giving them typical white color. Since particles forming a cloud generally span a wide range of sizes and shapes and are highly variable in concentrations, which all determines the precise characteristics of cloud scattering processes, the visual appearance of each individual cloud is a unique experience.

Visual observation of clouds from the ground for meteorological and climatological applications has a long-standing tradition reaching in the 18th century. The basic nomenclature for identification of clouds suggested by early observers later developed into well-established cloud classification system (International Cloud Atlas of the World Meteorological Organization). The vast majority of clouds occur in the lowest part of the atmosphere, where the predominance of water vapour, a necessary prerequisite for cloud formation, is stored. These tropospheric clouds, which can be spotted visually by a ground observer, are divided into ten mutually exclusive cloud genra. Depending on typical cloud base height, they are further classified as low, middle and high clouds. This dissertation aims to advance conceptual understanding of radiative transfer for four of these intrinsically different cloud types, namely the cumulus, stratocumulus, cirrus and cumulonimbus.

The task of a weather observer is to provide a description of the sky at a certain time. Looking at the sky for longer than just a glimpse, however, it is obvious that clouds are dynamically evolving. Figure 2.5 shows temporal evolution of fair-weather shallow cumuli during a five-hour paragliding flight. Since a vast part of the present thesis focuses on shallow cumulus clouds, this group of clouds is considered in a bit more detail. Thus cumulus clouds occur as warm, moist buoyant air rises, eventually becomes saturated and consequently water vapour condenses to form droplets. The liquid water content subsequently builds up by diffusional process, characterizing the initial cloud growth. Cumulus clouds might be either precipitating or non-precipitating, whereby the latter eventually evaporate. The cloud evolution often undergoes several well-defined stages, such as cumulus humilis, mediocris and congestus (Fig. 2.5). Similarly, a shallow cumulus layer can progress into

Figure 2.5: *Evolution of fair-weather shallow cumulus cloud field during five hours of paragliding across the border between Slovenia and Italy. Fair-weather shallow cumuli, an artifact of thermal convection, are, inter alia, indicators of good conditions for paragliding. Paragliders rely on them as indicators of rising thermals. They usually start forming in the late morning after sufficient surface heating. Often the first thermal maximum occurs at about 1−3 pm. The resulting ground shadowing weakens the buoyant updraft and causes partial cumulus dissipation. In favorable conditions a second thermal maximum occurs a few hours later in the afternoon, providing less turbulence and top experience for paraglider and hangglider pilots.*

forming a stratocumulus, capturing the transition from individual clouds to larger clusters. Such evolving shallow cumulus cloud field will be investigated in this thesis.

2.2.2 Cloud parameterization problem

Clouds exert multiple effects on the dynamic and thermodynamic state of the atmosphere. Besides interacting with radiation, they transport mass, heat and moisture as well as produce precipitation. All these effects need to be properly represented in atmospheric models. For the interaction of clouds with radiation, it is important to properly simulate microphysical and macrophysical structure of clouds. Further, there are two principal challenges regarding the conventional parameterization of unresolved cloud macrophysics (geometry) in weather and climate models that are crucial for radiative transfer calculations. These are the cloud fraction and vertical overlap parameterization and will as well be described in the following.

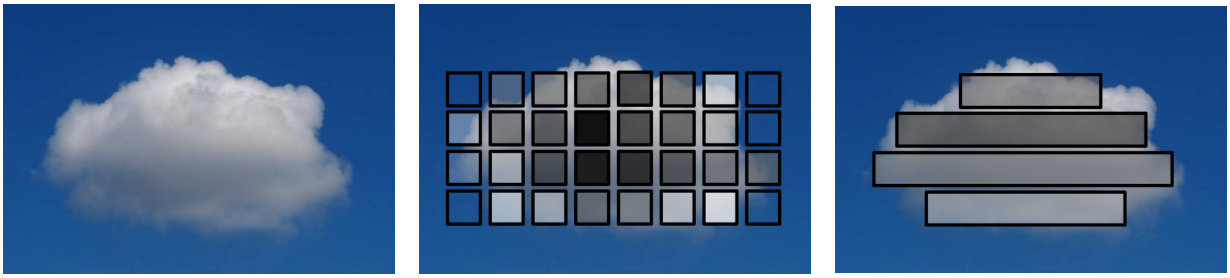

Figure 2.6: *Cloud parameterization problem: cloud macrophysical structure resolved (middle panel) and unresolved (right panel). Cloud microphysics is always unresolved, regardless of model resolution. The grey shading mirrors cloud optical thickness, with darker/lighter grey rendering larger/smaller values.*

Cloud microphysics parameterization

Water is the only substance in the atmosphere that exists in all three phases (gaseous, liquid, solid). Parameterizing cloud microphysics implies parameterizing physical processes that convert water between these various phases. The parameterization of cloud microphysics in atmospheric models again serves multiple tasks. Firstly, it supplies cloud optical properties to the radiation scheme. Secondly, it provides latent heating rates due to water phase changes and thereby directly feeds back on the resolved model dynamics. Thirdly, it provides precipitation rate and type reaching the ground, entering the surface parameterization scheme.

When parameterizing a broad scope of cloud microphysical processes (e.g., droplet formation and growth) that occur in a wide variety of environmental conditions constituting the global atmosphere, it is convenient to distinguish between clouds containing only liquid phase (termed *warm clouds*) and those containing only ice (termed *cold clouds*), since microphysical processes are often intrinsically different in these two circumstances. A special case are *mixed-phase clouds*, where liquid and ice phase coexist and generally require a separate treatment as well. The various microphysical schemes differ heavily in their complexity – e.g., depending on the number of hydrometeor categories (cloud water, cloud ice, rain, snow, graupel, hail), which they include. Whereas the details of microphysical parameterizations are not of main interest for the present work, the most important cloud microphysical properties affecting radiative transfer are highlighted in the next paragraph.

Cloud radiative properties

The cloud microphysical properties impacting radiation crucially depend on the size spectrum of cloud particles. For the radiative transfer simulations, precisely, it is of primary importance to know the second and the third moment of the distribution. The liquid water content and the effective radius can hence be derived as defined in the following. The liquid water content (LWC) is the mass of the entire ensemble of liquid droplets in a unit volume

of air given by:

$$LWC = \frac{4\pi\rho_l}{3}\int_0^\infty r^3 n(r)dr, \tag{2.1}$$

where $n(r)$ is the cloud droplet size distribution and ρ_l is the density of liquid water. The effective radius (R_e) is defined as the ratio between the third and the second moment of the size distribution:

$$R_e = \frac{\int r^3 n(r)dr}{\int r^2 n(r)dr}. \tag{2.2}$$

The LWC and R_e are the essential cloud microphysical properties that define the optical properties and hence how cloud will interact with radiation (Hansen and Travis, 1974). In cumulus clouds, as an illustration, LWC typically ranges between 0.1 and 1.5 g m^{-3} (Warner, 1955), whereas R_e typically lies in the range between 5 and 15 μm (Brenguier et al., 2000). Both LWC and R_e generally increase with height throughout the cloud (Arabas et al., 2009). At a given height in the cloud the LWC is usually found to be highly variable (e.g., Warner, 1955; Shonk and Hogan, 2008), whereas the R_e, on the contrary, is often fairly constant (Blyth and Latham, 1991).

Finally, the integration of LWC with respect to height yields the liquid water path (LWP):

$$LWP = \int_0^\infty LWC(z)dz, \tag{2.3}$$

which is usually specified in [g m^{-2}] and is commonly used to describe the total amount of liquid water within a column above a surface area.

The treatment of the ice phase regarding the ice water content (IWC), the effective radius of ice as well as the ice water path (IWP) is based on analogous considerations. In mixed-phase cloud regions, moreover, the total water content is the sum of LWC and IWC, whence the total water path can be derived.

Cloud fraction parameterization

There are various ways to parameterize partial cloudiness (cloud fraction) within a model grid box. In general, cloud fraction is the result of subgrid variability of temperature and humidity (Tompkins, 2005). The so-called *relative humidity schemes* prescribe a diagnostic relationship between the cloud fraction (C) and the grid box relative humidity (RH), where the former monotonically increases from zero to one after some threshold (critical relative humidity; RH$_{crit}$) is reached. A widely employed function was suggested by Sundqvist et al. (1989) (Fig. 2.7):

$$C = 1 - \sqrt{\frac{1 - RH}{1 - RH_{crit}}}, \tag{2.4}$$

although several variants thereof exist in practice, where RH$_{crit}$ is typically height-dependent, commonly estimated based on field campaign observations (Slingo, 1980), theoretical considerations (Sundqvist et al., 1989), high-resolution cloud numerical modeling

studies (Lohmann and Roeckner, 1996) or satellite data (Quaas, 2012). Whereas the disadvantage of relative humidity schemes might be that they implement a fixed RH_{crit}, which does not depend on local dynamical meteorological conditions, these schemes generally proved to work well being extensively utilized in numerical weather and climate prediction. Besides the above-outlined diagnostic relative humidity schemes an alternative group of parameterizations called statistical schemes (e.g., Sommeria and Deardorff, 1977) as well as computationally more expensive prognostic cloud cover schemes (e.g. Bony and Emanuel, 2001; Tompkins, 2002) were developed by cloud modelers worldwide.

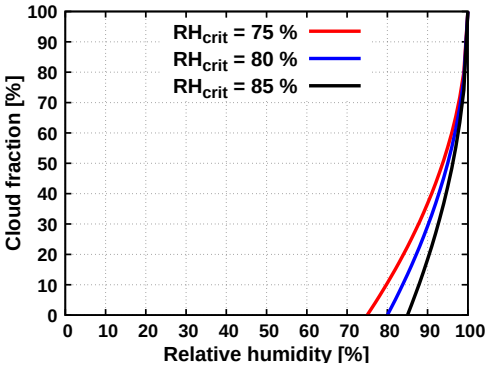

Figure 2.7: *Parameterization of cloud fraction according to Sundqvist et al. (1989) for various values of critical relative humidity.*

Vertical overlap parameterization

For the radiative transfer calculations it is necessary to specify how layer cloudiness overlaps in the vertical direction within an individual grid column of a weather or climate model. Figure 2.8 illustrates elementary overlap assumptions employed in the past and at present: maximum overlap (Fig. 2.8, left panel), random overlap (Fig. 2.8, middle panel) and maximum-random overlap (Fig. 2.8, right panel), which will be explained hereafter.

The maximum overlap is based on the assumption that the entire cloudiness within a grid column is formed by a coherent dynamical process. The partial cloudiness in various model layers therefore maximally overlaps in the vertical direction, which minimizes the total cloud cover. For a pair of arbitrary layers i and j (characterized by their cloud fraction components C_i and C_j) the total cloud cover corresponding to the maximum overlap rule ($C_{i,j}^{max}$) therefore equals to the maximum layer cloud fraction:

$$C_{i,j}^{max} = \max(C_i, C_j). \tag{2.5}$$

The random overlap (Manabe and Strickler, 1964), on the contrary, assumes that horizontal position of the cloud within a layer of interest is completely uncorrelated with the horizontal position of clouds in all other layers. This assumption generally leads to maximum total

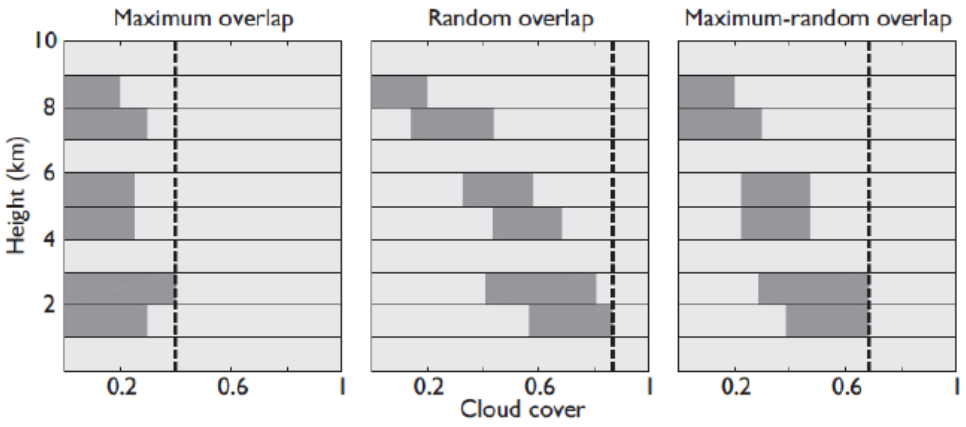

Figure 2.8: *Common vertical overlap parameterizations in weather and climate models. The vertical dotted line indicates the total cloud cover. Source: Hogan and Illingworth (2000).*

cloud cover, whereby for the pair of layers i and j the latter ($C_{i,j}^{rnd}$) is given by:

$$C_{i,j}^{rnd} = C_i + C_j - C_i C_j. \tag{2.6}$$

In the case of maximum-random overlap (Geleyn and Hollingsworth, 1979; Morcrette and Fouquart, 1986; Tian and Curry, 1989; Ritter and Geleyn, 1992) it is assumed that adjacent cloudy layers overlap maximally, whereas clouds separated by at least one cloud-free layer overlap randomly. This idea is physically justified with the following consideration: the cloudiness in contiguous model layers is a result of the same physical process, whereas the cloudiness separated by a cloud-free layer is formed independently and therefore overlaps with other cloud phenomena within the same vertical grid column in a random way. The maximum-random overlap was first introduced and incorporated in the two-stream radiation scheme by Geleyn and Hollingsworth (1979) and gained much in popularity in the following years. By the end of the century it was already well established, being employed in nearly all operational weather and climate models (Hogan and Illingworth, 2000).

The observations and high-resolution numerical modeling investigations show that the maximum-random overlap rule tends to underestimate the total cloud cover primarily in the case of vertically developed cloud systems in strongly sheared environmental conditions (e.g., Hogan and Illingworth, 2000; Bergman and Rasch, 2002; Mace and Benson-Troth, 2002; Naud et al., 2008). For this reason, currently the maximum-random overlap is being gradually replaced by a generalized overlap form, called the exponential-random overlap (e.g., Hogan and Illingworth, 2000; Shonk et al., 2010; Di Giuseppe and Tompkins, 2015). In this more general treatment of overlap it is still assumed that cloudy layers separated by at least one cloud-free layer overlap randomly, whereas cloud overlap within a vertically continuous series of layers is not maximal − instead it decorrelates with vertical layer separation according to a decorrelation scale. Consequently, for the continuous set of cloudy layers the overlap is something between maximum and random and can be expressed

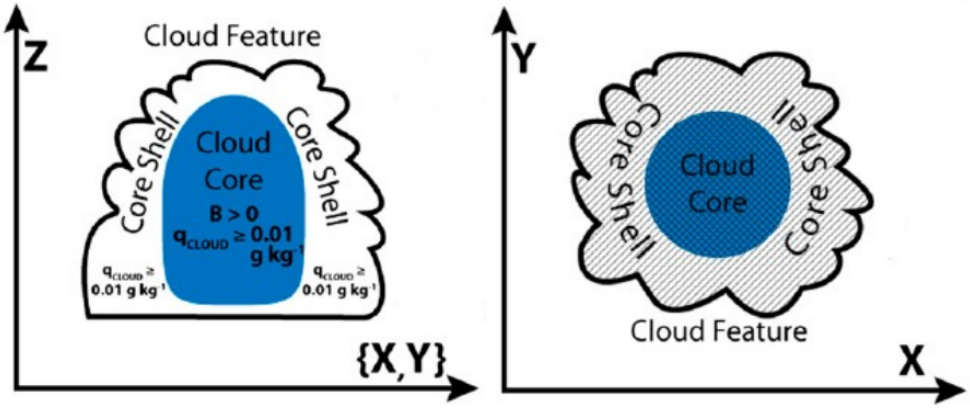

Figure 2.9: *Partitioning of cloud feature into central cloud core and the surrounding shell: the left/right scheme depicts vertical/horizontal cross-section. Source: Seigel (2014) (modified).*

with the aid of overlap parameter α as follows:

$$C_{i,j}^{exp-ran} = \alpha C_{i,j}^{max} + (1-\alpha) C_{i,j}^{ran}. \tag{2.7}$$

The limit of α=1 corresponds to maximum overlap, whereas the limit of α=0 implies random overlap.

The two-stream radiative solvers constructed within the scope of this dissertation, however, are based on the classic maximum-random rule. It should be noted that in regional models the latter is still the most common overlap form − recall that the majority of vertically developed deep convective systems is resolved at regional model grids and is therefore not exposed to any overlap assumptions. The work towards an advancement of Tripleclouds usage in global models carried out in this thesis, moreover, focuses on the issues related to cloud horizontal inhomogeneity misrepresentation, excluding the additional vertical overlap problematics. It should be emphasized in this respect that the maximum-random rule is solely a special case of generalized exponential-random overlap.

Core-shell model for convective clouds

A brief note regarding the horizontal distribution of cloud condensate in convective cloud systems is provided herein. This knowledge will be exploited later when constructing the Tripleclouds radiation scheme. Shallow cumulus, stratocumulus and cumulonimbus clouds are convective clouds, which are often treated with the so-called "core-shell model" (Heus and Jonker, 2008; Heiblum et al., 2019). In this model, the convective cloud "core" associated with updraft motion and increased condensate loading is located in the geometrical center of the cloud, surrounded by the cloud "shell" associated with downdrafts and condensate evaporation (Fig. 2.9). The core-shell model is supported by multiple observational studies (e.g., Heus et al., 2009; Rodts et al., 2003; Wang et al., 2009) and numerical modeling investigations (e.g., Heus and Jonker, 2008; Jonker et al., 2008; Seigel, 2014)

and hence represents the essence of several convection parameterizations. Heiblum et al. (2019) showed that the core-shell model is valid for about 90 % of a typical cloud's lifetime, with the largest discrepancy from the assumed core-shell geometry occurring during the dissipation stage of the cloud. Whereas most of the clouds contain a single core, larger clouds can possess multiple cores. Similarly, clouds in a cloud field have multiple cores, whereby their aggregate effect can be modeled with a core-shell model (Heiblum et al., 2019). In addition to convective cloudiness, also stratiform clouds, such as cirrus clouds, frequently exhibit embedded weaker convective elements, which own core characteristics (Heymsfield, 1977; Mitchell, 1994).

2.3 Atmospheric radiation

This section introduces fundamentals of atmospheric radiation. It begins by establishing the radiative transfer theory in a three-dimensional atmosphere and then derives the one-dimensional (plane-parallel) approximation. The description is based primarily on the books of Marshak and Davis (2005), Wallace and Hobbs (2006), Zdunkowski et al. (2007) and Stensrud (2007).

2.3.1 Radiative transfer theory

Atmospheric radiative spectrum: solar and thermal radiation

Atmospheric radiative transfer (RT) involves an ensemble of electromagnetic waves. Table 2.1 shows the partitioning of atmospheric radiative spectrum into specific bands, where the wavelength of radiation λ is defined as:

$$\lambda = \frac{c}{\nu}, \tag{2.8}$$

with c being the speed of light in [m s^{-1}] and ν being the frequency in [s^{-1}]. The separation of solar (shortwave) and thermal (longwave) radiative spectrum at 3.5 μm has a variety of facilitations in numerical weather and climate prediction, as we shall appreciate later.

Basic radiative quantities

A radiation beam is characterized by its radiant power Φ [W], which is the radiant energy dQ [J] per unit time dt. Other common radiative quantities are radiance L and radiative flux (or irradiance) E. Their spectral definitions read as follows:

$$L = \frac{dQ}{dt\, dA\, dcos\theta\, d\lambda\, d\Omega} \quad [\mathrm{W\ m^{-2}\ nm^{-1}\ sr^{-1}}], \tag{2.9}$$

$$E = \frac{dQ}{dt\, dA\, d\lambda} \quad [\mathrm{W\ m^{-2}\ nm^{-1}}]. \tag{2.10}$$

Abbreviation	Description	Wavelength range	
UV	Ultraviolet	20 nm $< \lambda <$ 400 nm	Solar radiation
VIS	Visible	400 nm $< \lambda <$ 700 nm	
Near IR	Near infrared	0.7 μm $< \lambda <$ 3.5 μm	
IR	Infrared	3.5 μm $< \lambda <$ 100 μm	Thermal radiation

Table 2.1: *Categorization of atmospheric electromagnetic spectrum for the solar and thermal radiation according to Zdunkowski et al. (2007).*

The spectral radiance L is defined as the radiant power per unit area dA perpendicular to the incident radiance direction (with θ representing the angle between propagation direction and area normal) per unit wavelength $d\lambda$ and unit solid angle $d\Omega$. The spectral radiative flux E is the radiant power per unit area dA and unit wavelength $d\lambda$.

Interaction of radiation with the atmosphere

Radiation, once *emitted*, propagates through the atmosphere and interacts with its constituents (molecules, cloud droplets, ice crystals and aerosol particles) via underlying physical processes – *absorption* and *scattering*. These processes generally depend on the wavelength of radiation as well as on various characteristics of radiatively active atmospheric constituents (as illustrated in Fig. 2.10). In order to characterize optical properties of the latter, three basic parameters are used, namely the extinction coefficient k_{ext}, single scattering albedo ω_0 and asymmetry parameter g, defined in the following. Besides, basic radiative laws governing the emission, absorption and scattering as well as other common quantities, which will be used later in the analysis, will be introduced.

Emission

Emission is the source of radiation. The source of solar radiation is the Sun, which emits radiation approximately as a blackbody at a temperature of 5777 K (Thomas and Stamnes, 1999) (Fig. 2.11, left panel). The source of thermal radiation is the Earth's surface and the Earth's atmosphere, which as well emit approximately as blackbodies. The emission of radiation for a blackbody in thermodynamic equilibrium is governed by *Planck's radiation law* (Planck, 1900) (Fig. 2.11, right panel):

$$B_{Planck}(T,\lambda) = \frac{2hc^2}{\lambda^5}\left[\exp\left(\frac{hc}{\lambda k_B T}\right) - 1\right]^{-1}, \tag{2.11}$$

where T is the temperature of the blackbody, h is the Planck constant and k_B is the Boltzmann constant. When observing the spectral radiance distribution according to Planck's

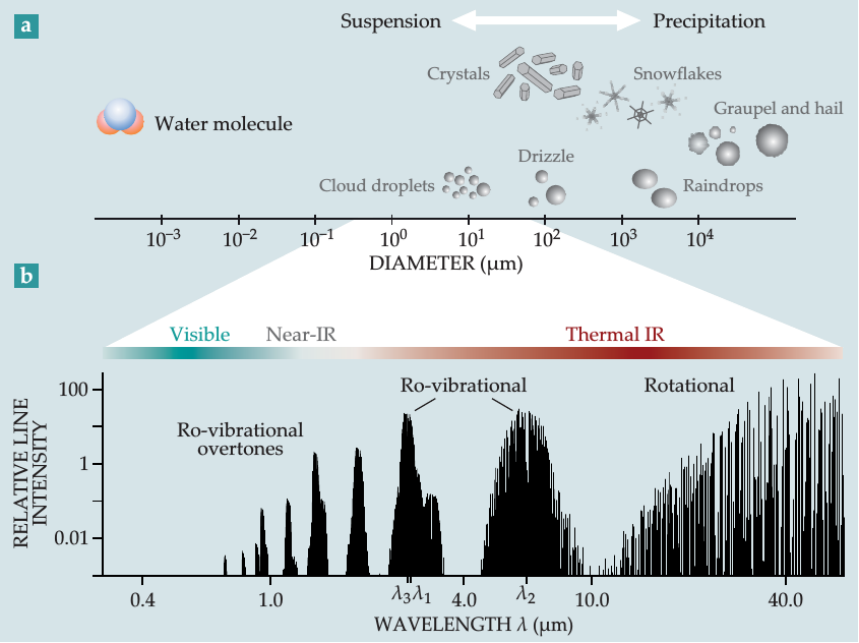

Figure 2.10: *The interaction of radiation and hydrometeors (e.g., cloud droplets, ice crystals) generally depends on the wavelength of radiation as well as on various hydrometeor characteristics (e.g., hydrometeor size and shape). Source: Stevens and Bony (2013).*

law of ideal blackbodies at different temperatures (Fig. 2.11, right panel), the inverse relationship between the temperature and the wavelength of the radiative spectrum maximum (λ_{max}) is found, which is known as *Wien's displacement law* (Wien, 1896). Integrating Planck's radiation law over half space and over the wavelength yields *Stefan-Boltzmann's law* (Stefan, 1879):

$$E_{Planck}(T) = \pi \int_0^\infty B_{Planck}(T, \lambda) d\lambda = \sigma_B T^4, \tag{2.12}$$

which gives the irradiance as a function of blackbody temperature, where $\sigma_B = 2\pi^5 k_B^4 / 15 h^3 c^2$ represents the Stefan-Boltzmann constant.

The actual radiance emitted by a nonblack material (e.g., atmospheric gases) is modified by the absorptivity $\alpha(\lambda)$:

$$\frac{L(\lambda)}{\alpha(\lambda)} = B_{Planck}(T, \lambda). \tag{2.13}$$

Hereby the relationship known as *Kirchhoff's law* (Kirchhoff, 1890) was taken into consideration:

$$\epsilon(\lambda) = \alpha(\lambda), \tag{2.14}$$

which states that for a body in thermal equilibrium the emissivity (ϵ) equals its absorptivity (α) (note that for a blackbody α=1).

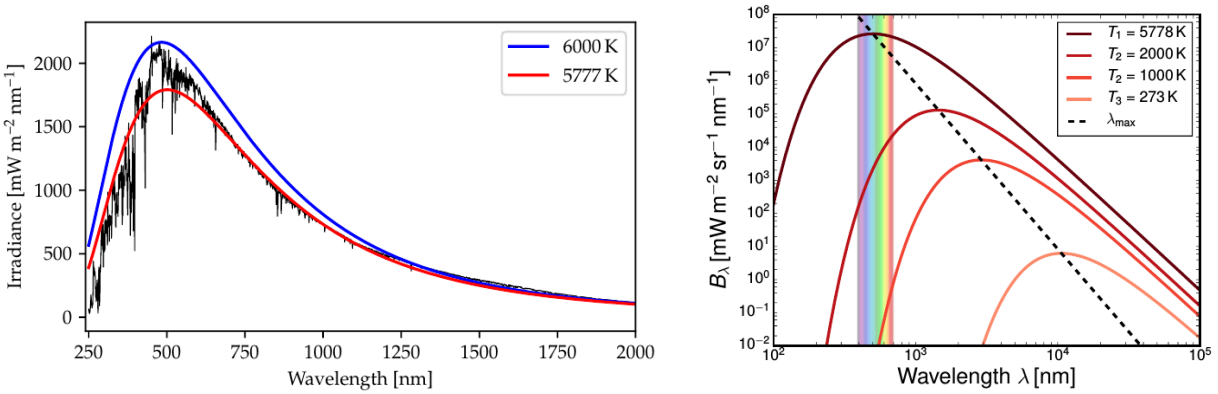

Figure 2.11: *Left panel: the solar spectrum, measured at the top of the atmosphere, based on data from Kurucz (1992) (black line) shows a great similarity to the radiation spectrum of an ideal blackbody with a temperature of 6000 K (Zdunkowski et al., 2007) (blue line) or 5777 K (Thomas and Stamnes, 1999) (red line). Source: Forster (2017). Right panel: spectral radiance distribution according to Planck's law at different blackbody temperatures. For extremely hot blackbodies at temperatures corresponding to those of the Sun, the maximum of the radiation spectrum is located in the VIS range (color shaded), whereas the maximum of radiation emitted at terrestrial temperatures (e.g., 273 K) lies at approximately 10 µm. Source: Ewald (2016).*

For the calculations of atmospheric radiative transfer, one usually specifies the solar flux at the top of the atmosphere (S_0 at TOA) as an external source of atmospheric radiation. Similarly, the thermal radiation source − the emission of the Earth's surface and the atmosphere is modeled according to Planck's radiation law and its derived formulations introduced above. As already mentioned the solar and thermal radiation spectra are separated at 3.5 μm and are customarily treated separately for practical applications. This implies that in the solar spectral range it is justified to omit the Planck function B_{Planck}, whereas in the thermal spectral range S_0 is neglected.

Scattering

The direction of the radiation beam propagating through the atmosphere might be changed via the scattering process. We observe scattering from direction of incidence $\mathbf{\Omega'} = (\theta', \phi')$ to $\mathbf{\Omega} = (\theta, \phi)$, where (θ', ϕ') and (θ, ϕ) are the zenith and azimuth angles of the incident and scattered radiation, respectively. The scattering asymmetry parameter g is defined as follows:

$$g = \frac{1}{2} \int_{-1}^{1} P(\cos\Theta) \cos\Theta d\cos\Theta, \tag{2.15}$$

where $P(\cos\Theta)$ is the normalized angular distribution of the scattered radiation or the *scattering phase function*. The term $\cos\Theta = \mathbf{\Omega'} \cdot \mathbf{\Omega}$ represents the cosine of the scattering angle Θ and means that the scattering is rotationally symmetric around the incident direction (Fig. 2.12). The value of asymmetry parameter spanning the range between $g = 1$

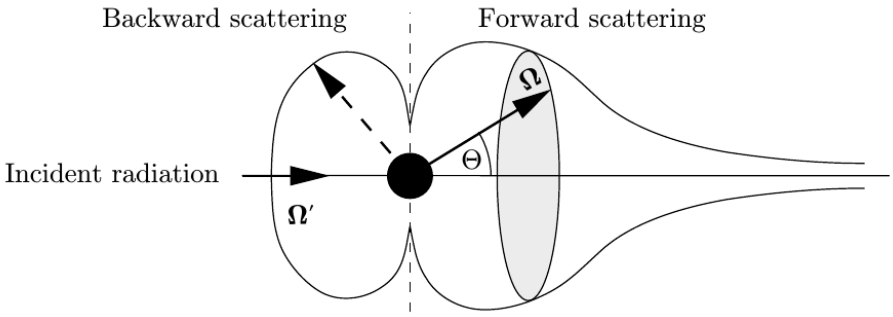

Figure 2.12: *Rotationally symmetric scattering phase function, which is adequate for spherical or randomly oriented particles. Source: Zdunkowski et al. (2007).*

(complete forward scatter) and $g = -1$ (complete backward scatter) implies:

- $g = 0$: isotropic scattering,
- $g > 0$: scattering predominantly into forward direction,
- $g < 0$: scattering predominantly into backward direction.

Typical values of g in the atmosphere range from approximately 0 for molecules, 0.50 for aerosols, 0.80 for ice crystals and 0.85 for cloud droplets (Wallace and Hobbs, 2006).

The exact nature of the scattering process, moreover, is controlled by dimensionless size parameter χ, which depends on particle size and wavelength of the incident radiation:

$$\chi = \frac{2\pi r}{\lambda}, \tag{2.16}$$

where r is the radius of a spherical particle. For non-spherical particles an alternative definition is introduced:

$$\chi = \frac{\pi D}{\lambda}, \tag{2.17}$$

where D is maximum particle dimension. Depending on the value of χ, three basic scattering regimes exist:

- $\chi \ll 1$: Rayleigh scattering (Strutt, 1871),
- $\chi \approx 1$: Mie-Debye theory (Mie, 1908),
- $\chi \gg 1$: Geometric optics limit.

The Rayleigh scattering regime is relevant for the interaction of atmospheric molecules with the radiation in the solar (visible) part of the spectrum. Within this Rayleigh regime, the scattering cross section (efficiency) is inversely proportional to λ^4 (Thomas

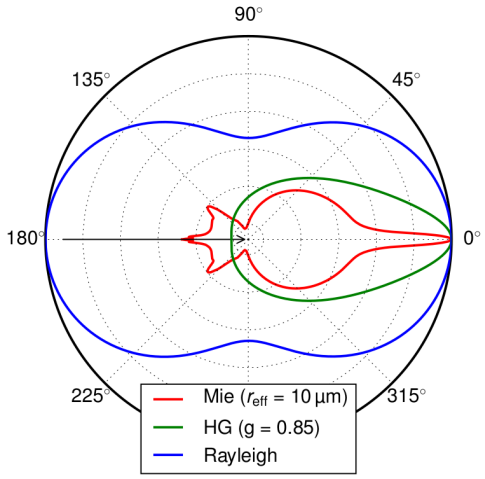

Figure 2.13: *Angular distribution of scattered radiation for different scattering regimes: the Mie scattering phase function (calculated for the interaction of radiation with a wavelength of 2.1 µm and a spherical liquid droplet with a radius of 10 µm), the Henyey-Greenstein scattering phase function (denoted as HG; evaluated for a typical cloud droplet asymmetry parameter of 0.85) and the Rayleigh scattering phase function. Source: Ewald (2016).*

and Stamnes, 1999), which explains the blue color of the sky. The phase function for the Rayleigh scattering (Fig. 2.13) has the following form:

$$P(\cos\Theta) = \frac{3}{4}(1 + \cos^2\Theta), \tag{2.18}$$

which means that the scattered radiation is evenly distributed between the backward and forward hemisphere (i.e., isotropic scattering). Strictly speaking, the Rayleigh scattering applicable for $\chi \ll 1$ is only a special simplified case of the Mie scattering, which can be treated with the mathematical framework of the rigorous Mie-Debye electromagnetic theory. Contrary to the isotropic Rayleigh scattering, the scattering for χ-values equal or greater than 1 (as is the case for larger scattering particles such as aerosols, cloud droplets and ice crystals) is predominantly into the forward direction. For $\chi \approx 1$ the Mie scattering phase function is often approximated by the analytical Henyey-Greenstein function (Henyey and Greenstein, 1941) (Fig. 2.13). The latter can be expressed with the aid of asymmetry parameter in the following way:

$$P(\cos\Theta) = \frac{1 - g^2}{(1 + g^2 - 2g\cos\Theta)^{3/2}}. \tag{2.19}$$

Similarly, for particles much larger than the wavelength yielding the size parameters $\chi \gg 1$, the classical theory of geometric optics can be applied.

Absorption

The absorption is the sink of radiation: when the light hits the particle (molecule), it can get absorbed by it. In similarity to the emission spectra, which at a quantum level are not continuous, also the absorption spectra reveal a discrete form. Precisely, they consist of numerous individual absorption spectral lines with different intensity, which frequently appear as bands of lines. These are characteristic for a particular molecule. The combined effect of absorption and scattering in depleting the radiation along the observed direction is referred to as the extinction. The attenuation of radiance by extinction is given by the *Beer-Bouguer-Lambert's law*:

$$L(s) = L(0) \exp\big[-\int_0^s k_{ext}(s')ds'\big]. \tag{2.20}$$

It is convenient to define the optical thickness τ, a dimensionless quantity describing the medium quality regarding how strong it attenuates the radiation along a tilted path:

$$\tau(s) = \int_0^s k_{ext}(s')ds'. \tag{2.21}$$

The extinction coefficient k_{ext} is the sum of the absorption coefficient k_{abs} and the scattering coefficient k_{sca}:

$$k_{ext} = k_{abs} + k_{sca}, \tag{2.22}$$

or alternatively:

$$k_{ext} = \int_0^\infty n(r)\sigma_{ext}(r)dr, \tag{2.23}$$

where $n(r)$ is the number density of particles which are involved in the absorption and scattering processes and $\sigma_{ext}(r)$ is the corresponding extinction cross section, with r representing the particle radius.

In the limit of geometric optics, $\sigma_{ext}(r) = 2\pi r^2$, hence the cloud optical thickness (usually evaluated along a vertical direction) is approximated as follows:

$$\tau \approx \frac{3LWP}{2\rho_l R_e}. \tag{2.24}$$

The broad spectrum of cloud phenomena generally exhibit a wide range of cloud optical thickness, ranging from less than 0.01 for thin cirrus to more than 100 for deep liquid clouds (Chen et al., 2000). Since the extinction is wavelength dependent, values of cloud optical thickness generally differ when the same cloud volume is interacting with solar and thermal radiation. Throughout this dissertation given values of cloud optical thickness refer to the visible spectral range.

The single scattering albedo ω_0 is defined as the ratio between the scattering and extinction coefficient:

$$\omega_0 = \frac{k_{sca}}{k_{ext}} \tag{2.25}$$

and hence measures the relative importance of scattering and absorption. In the thermal spectral range, the dominant interaction process is absorption ($\omega_0 \approx 0$). The thermal scattering is present only in the atmospheric window region (characterized by weak absorption) between 8 and 14 μm (Stephens, 1984), although it is frequently entirely neglected in the radiative transfer calculations. On the contrary, the most important interaction of solar radiation with the atmosphere is the scattering process.

Radiative transfer equation

At this point, the above-outlined interactions of radiation with the medium (scattering, absorption, emission) can be brought together in the prominent *radiative transfer equation* (RTE), primarily introduced by Chandrasekhar, 1950. In a three-dimensional medium, this linear integro-differential equation for the spectral radiance L has the following form (Zdunkowski et al., 2007):

$$\boldsymbol{\Omega} \cdot \nabla L = \underbrace{-k_{ext} L}_{(1)} + \underbrace{\frac{k_{sca}}{4\pi} \int_{4\pi} P(\boldsymbol{\Omega'} \cdot \boldsymbol{\Omega}) L(\boldsymbol{\Omega'}) d\boldsymbol{\Omega'}}_{(2)} + \underbrace{k_{abs} B_{Planck}}_{(3)}. \tag{2.26}$$

The terms on the right-hand-side of the equation have the following physical meaning:

- (1) Attenuation of radiance by extinction via absorption and scattering of radiation out of the observed direction ("out-scattering").
- (2) Scattering of the radiation from other directions into the direction of interest ("in-scattering").
- (3) Contribution of thermal emission to the radiance in the observed direction.

Solving the RTE in its complete form as formulated above is a demanding task. No analytical solution exists if the scattering (term (2)) is accounted for. If the scattering is omitted as it is a fairly reasonable action in the thermal spectral range, the RTE simplifies to Schwarzschild's equation. A popular technique for solving the radiative transfer equation problem is the Monte Carlo modeling (e.g., Mayer, 2009), which enables an accurate 3-D solution. This is computationally too expensive to be routinely used in weather and climate models, but is suitable for offline research study radiation calculations. It shall be used in this work and will therefore be explained in more detail in the next chapter.

Radiative heating rate

The difference between the absorbed and emitted radiation within an atmospheric air volume leads to temperature change. This radiatively induced temperature tendency is called the *radiative heating rate* [K day^{-1}]:

$$\frac{\partial T}{\partial t} = -\frac{1}{\rho c_p} \nabla \cdot \vec{E}_{net}, \tag{2.27}$$

where $\nabla \cdot \vec{E}_{net}$ is the divergence of the net radiative flux vector. The constants ρ and c_p represent the density and specific heat capacity of the medium, respectively. This quantity will be frequently used in the analysis throughout this dissertation, spectrally integrated over the solar and thermal radiative spectrum, and therefore referred to as the *solar* and *thermal radiative heating (or cooling) rate*. Similarly, we will commonly investigate the *net surface radiative flux* [W m^{-2}] in the solar and thermal spectral range. The latter is defined as the difference between the downward and upward radiative flux at the Earth's surface, thus being directly proportional to the surface heating.

2.3.2 Plane-parallel radiative transfer approximation

Radiative transfer calculations can be markedly simplified by assuming that atmospheric temperature as well as density of radiatively active atmospheric constituents are a function of vertical coordinate z (height) only. In this one-dimensional radiative transfer approximation, the RTE for horizontally homogeneous (plane-parallel) atmosphere attains the following form:

$$\mu \frac{d}{d\tau} L(\tau, \mu, \phi) = L(\tau, \mu, \phi) - \frac{\omega_0}{4\pi} \int_0^{2\pi} \int_{-1}^{1} P(\cos\Theta) L(\tau, \mu', \phi') d\mu' d\phi' - (1 - \omega_0) B_{Planck}(T), \tag{2.28}$$

using $\mathbf{\Omega} \cdot \nabla L = dL/ds$, whereby the path length $ds = dz/\mu$ with $\mu = \cos\theta$ and $d\tau = -k_{ext} dz$. In practice, when the radiative transfer is computed within dynamical models, this implies that the vertical atmospheric profiles from the individual independent column are utilized to build the plane-parallel medium, which is assumed to stretch to infinity in horizontal directions. The plane-parallel approximation serves well if atmospheric vertical gradients are notably larger than the corresponding horizontal gradients. In other words, the plane-parallel assumption is fairly reasonable in clear-sky conditions, whereas it is generally inadequate in the presence of clouds (e.g., Schmetz, 1984; O'Hirok and Gautier, 1998a,b, 2005; Di Giuseppe and Tompkins, 2003a,b, 2005; Tompkins and Di Giuseppe, 2007; Wissmeier et al., 2013).

In the plane-parallel theory the net radiative flux vector divergence simplifies: $\nabla \cdot \vec{E}_{net} = \partial E_{net,z}/\partial z$, hence the radiative heating rate can be derived solely from vertical radiative fluxes:

$$\frac{\partial T}{\partial t} = -\frac{1}{\rho c_p} \frac{\partial E_{net,z}}{\partial z}. \tag{2.29}$$

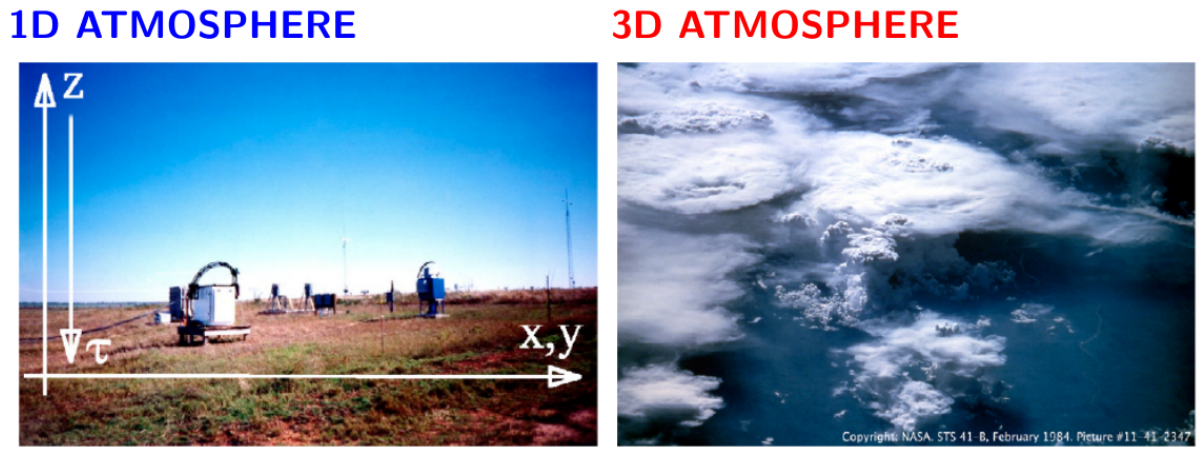

Figure 2.14: *Examples of one-dimensional (left panel) and three-dimensional (right panel) atmosphere. Source: Mayer (2009).*

As a standard technique for the RTE solution in the plane-parallel medium, computationally efficient analytical two-stream methods (TSMs) are widely employed. They have a more than a century long tradition (Schuster, 1905; Schwarzschild, 1906) and are now broadly used in weather and climate models. The common feature of the various TSMs is the representation of the entire radiative field with two directional streams − one governing the upwelling part of radiation and the other governing the downwelling part. Another convenient TSM convention is to further split the downwelling radiation into direct (unscattered) and diffuse (scattered) component. When TSM methods are applied in weather and climate models, which distinguish between the cloudy and the cloud-free portion of the grid box, they are further modified to incorporate the partial cloudiness. Although a wide collection of TSMs exists at the present time, in the subsequent paragraph the popular δ-Eddington approximation to the two-stream radiative flux approach is introduced, since we will later utilize this methodology.

δ-Eddington approximation

The main problem when solving the RTE is the treatment of scattering in the solar part of the spectrum. As highlighted previously, the solar scattering on cloud droplets and ice crystals is highly asymmetric, being strongly forward peaked. Classic two-stream methods thereby frequently yield insufficient results, because the forward scattering peak is not properly accounted for. This issue is practically tackled by applying the δ-scaling methodology, where the original scattering phase function is replaced with a δ-function in the forward direction and a smoothed function in other directions. In the following we explain how the δ-scaling is introduced into the Eddington approximation, yielding the widely utilized δ-Eddington approximation (Joseph et al., 1976).

In the Eddington approximation the radiance is independent of the azimuth angle:

$$L(\tau, \mu, \phi) = L_0(\tau) + \mu L_1(\tau). \tag{2.30}$$

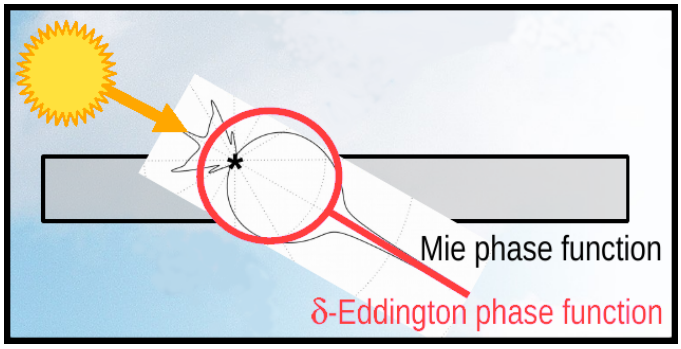

Figure 2.15: *The δ-Eddington phase function compared with the proper Mie scattering phase function. Source: Prof. Dr. Robin Hogan (modified).*

A consequence of this approximation is that the phase function, which is expanded in a series of orthogonal Legendre polynomials, is truncated after the linear term:

$$P(\cos\Theta) \approx 1 + 3g\cos\Theta. \tag{2.31}$$

In the δ-Eddington approximation (Fig. 2.15), the δ-scaling of the scattering phase function thus yields its approximation expressed as:

$$P(\cos\Theta) \approx P_{\delta-Eddington}(\cos\Theta) = 2f\delta(1-\cos\Theta) + (1-f)(1+3g'\cos\Theta), \tag{2.32}$$

where f represents the fraction of radiation scattered in the forward direction, δ is the Dirac delta function and g' is the asymmetry parameter of the truncated phase function. The speciality of the δ-Eddington approximation is the assumption $f = g^2$, which proved to work well over a vast range of cloud conditions. Whereas the introduced methodology leaves the RTE formally invariant, the original set of optical properties (k_{ext}, ω_0, g) is replaced by its scaled counterpart (k'_{ext}, ω'_0, g') obeying the following relationships:

$$k'_{ext} = (1-\omega_0 f)k_{ext}, \qquad \omega'_0 = \frac{(1-f)\omega_0}{1-\omega_0 f}, \qquad g' = \frac{g-f}{1-f}. \tag{2.33}$$

It should be noted that in the δ-scaling approximation the extinction of the direct radiation (S) governed by the Beer-Bouguer-Lambert's law is given by:

$$S(\tau') = S_0 \exp(-\tau'/\mu_0), \tag{2.34}$$

with μ_0 representing the cosine of the solar zenith angle and consistently utilizing the scaled optical thickness τ':

$$\tau' = (1-\omega_0 f)\tau. \tag{2.35}$$

Since $\tau' \leq \tau$, the δ-scaled direct radiative flux is larger than the unscaled value. This implies that the sum of the scaled direct and the scaled diffuse radiation has to be compared with the measured global radiation (i.e., total downward radiation). It should finally be reminded that the δ-scaling does not affect the absorption coefficient and thus the emission of thermal radiation.

2.4 Cloud-radiation interaction

The principal characteristics of cloud-radiation interaction are outlined next. Whereas the cloud-radiative effects are caused by clouds themselves and thus pronouncedly manifested within the cloud layer, they are strongly imprinted also at the surface. We observe the realistic 3-D radiation computation and subsequently highlight the chief drawbacks of the ICA calculation, when both are performed on the same highly resolved cloud field as illustrated in Fig. 2.16. Although weather and climate models do not resolve the classic 3-D cloud-radiative features perceived locally on high-resolution research model grid, these transform into systematic biases when averaged over larger scale, comparable to a weather or climate model grid box size. As a substantial aim of this thesis is to quantify the extent of the latter in order to pave the way towards improved radiation parameterizations in coarse-resolution models, the physical understanding of the 3-D cloud-radiation interplay is the prerequisite provided in this section. Some crucial parameters governing the interchange between clouds and radiation are as well exposed.

2.4.1 Three-dimensional cloud-radiation interaction

We examine first the benchmark interaction of radiation with a cloud in standard atmospheric conditions. Figure 2.17 shows three-dimensional heating rate distribution within the atmosphere as well as the net surface flux distribution for a realistic shallow cumulus cloud field (LES cumulus case from the Intercomparison of 3-Dimensional Radiation Codes, I3RC; Cahalan et al., 2005) calculated with the accurate 3-D Monte Carlo radiative model MYSTIC (Mayer, 2009).

In the solar spectral range (Fig. 2.17, left panel) at an oblique Sun illuminating the cloud scene from the side, the largest heating is at the illuminated cloud side and the heating rate generally decreases towards the interior of the cloud. This is the well-acknowledged "cloud side illumination effect" (Várnai and Davies, 1999; Hogan and Shonk, 2013; Jakub and Mayer, 2015, 2016). Solar photons that were not absorbed within the illuminated cloud portion have a high chance to be scattered in the forward direction out of the cloud, which leads to decreased heating rate at the opposite side of the cloud. This well-established 3-D radiative effect is referred to as "cloud side escape" or "cloud side leakage" (O'Hirok and Gautier, 1998a, 2005; Várnai and Davies, 1999; Hogan and Shonk, 2013). Along the direction of direct radiation beam, furthermore, substantial shadowing is observed in the atmosphere underneath the cloud as well as at the ground. This shadow is displaced and elongated according to solar zenith angle, consequently the net surface flux is highly inhomogeneous with noticeable local maxima and minima (Wapler and Mayer, 2008; Wissmeier et al., 2013; Jakub and Mayer, 2015, 2016).

In the thermal spectral range (Fig. 2.17, right panel) there is strong cooling at cloud top and cloud sides and modest warming at cloud bottom (Kablick et al., 2011; Klinger and Mayer, 2014, 2016). The strongest cooling is observed at cloud top, which is a result of efficient cloud top emission and simultaneously weak emission of radiation stemming

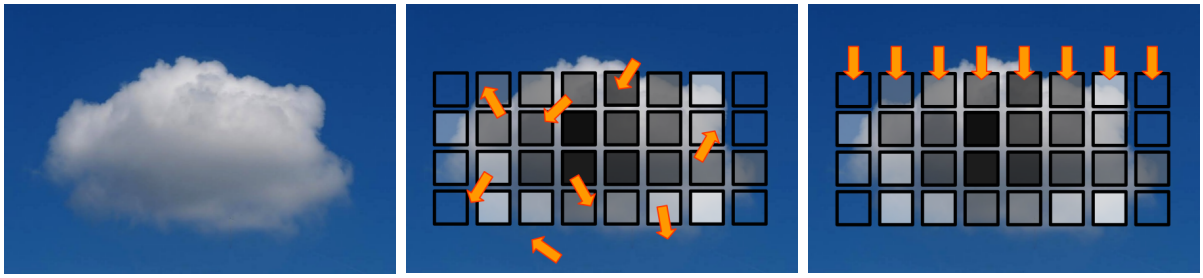

Figure 2.16: *An illustration of the 3-D (middle panel) and the ICA (right panel) radiation calculation on a highly resolved cloud field, which is considered to be the best proximity for a cloud in the real world (left panel). The darker/lighter grey shading represents larger/smaller optical thickness. The arrows denote radiative fluxes, abling to propagate throughout the entire domain in the 3-D configuration, whereas being confined to individual vertical model columns in the ICA.*

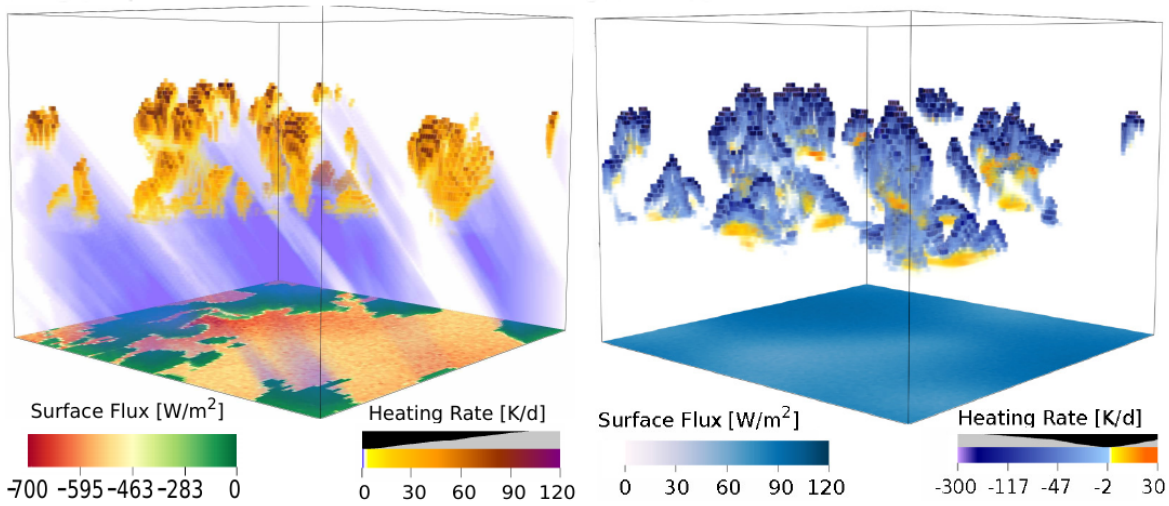

Figure 2.17: *Three-dimensional atmospheric heating rate distribution for realistic cumulus cloud field (I3RC; Cahalan et al., 2005) in the solar (left panel) and thermal (right panel) spectral range. Shown is also the net surface flux distribution underneath the cloud field. The radiation calculations were performed with the Monte Carlo radiative transfer model MYSTIC. Source: Dr. Fabian Jakub (personal correspondence).*

from the cooler atmosphere above, being absorbed at cloud top. Similarly, notable "cloud side cooling" (Kablick et al., 2011; Klinger and Mayer, 2014, 2016; Schäfer et al., 2016) is due to efficient sideward emission of radiation from cloud lateral areas into the surrounding cloud-free regions. The modest warming observed at cloud bottom is predominantly due to absorption of radiation emitted from warmer atmospheric layers underneath. In contrast to solar radiation, which can propagate deeper into the cloud interior, thermal heating and cooling rates are strongly confined to cloud edges (Klinger and Mayer, 2014, 2016). The thermal net surface flux distribution underneath the cloud field is fairly uniform.

2.4.2 Independent Column Approximation

In the one-dimensional ICA approach the solution to radiative transfer problem is confined to each individual domain grid column. Although various techniques exist for solving the RT problem within the independent column (e.g., two-stream approach), they all prevent horizontal energy exchange across the model domain. The consequent ICA shortcomings are elucidated herein, firstly for solar and subsequently for thermal radiation.

Whereas in the 3-D configuration the largest solar heating rate is observed at the sunlit cloud side, the peak heating is always located at cloud top in the ICA (Fig. 2.18), which is fundamentally wrong unless the Sun is at zenith (O'Hirok and Gautier, 2005; Jakub and Mayer, 2015). Similarly, whereas in the 3-D calculation a reduced heating rate is observed at the shadowed cloud side, the photons are prohibited to leak out through cloud side in the ICA, which leads to unrealistically increased heating rate at this side (O'Hirok and Gautier, 1998a, 2005; Várnai and Davies, 1999). When examining the horizontally averaged effect in the cloud layer, which would be a relevant quantity for the parameterization in weather and climate models, the increased heating at the illuminated cloud side partly compensates the decreased heating at the opposite side of the cloud in the 3-D configuration. The extent of the remaining ICA bias as a function of various parameters (e.g., Sun elevation as well as several cloud characteristics) is uncertain and will be partially unfolded in the present work.

The two opposing solar 3-D effects partly compensate also when observing the averaged net surface flux. The surface shadow in the ICA is always located directly underneath the cloud and remains of constant size, regardless of Sun elevation (O'Hirok and Gautier, 2005; Wapler and Mayer, 2008; Wissmeier et al., 2013; Jakub and Mayer, 2015). The realistic cloud side illumination implies an elongated surface shadow when the Sun is not at zenith, which results in overall reduced direct solar surface flux in the 3-D calculation compared to that in the ICA (Wapler and Mayer, 2008; Wissmeier et al., 2013; Jakub and Mayer, 2015). Similarly, surface diffuse radiation distribution is misrepresented in the ICA (Wapler and Mayer, 2008; Wissmeier et al., 2013). The cloud side escape commonly leads to overall increased diffuse radiation at the ground in the 3-D configuration compared to that in the ICA (O'Hirok and Gautier, 1998a, 2005). It remains unclear and poorly quantified, how much of the ultimate impact remains at the scale of global mesoscale and regional models for varying parameters governing the radiative transfer.

In the thermal spectral range, the ICA approximately captures cloud top cooling and cloud base warming, whereas it completely neglects cooling at cloud sides (Kablick et al., 2011; Klinger and Mayer, 2014, 2016), since sideward emission is suppressed. Contrarily to partially compensating solar cloud side phenomena, the thermal cloud side cooling effect is additive and thus systematic when inspecting larger-scale averages. Finally, the ICA commonly underestimates the proper thermal net surface flux, since realistic cloud side emission, which acts to increase downward surface radiation, is suppressed (Schäfer et al., 2016).

The described classic 3-D cloud-radiative effects are explicitly marked in Fig. 2.19, where radiative transfer experiments were performed for idealized clouds with constant

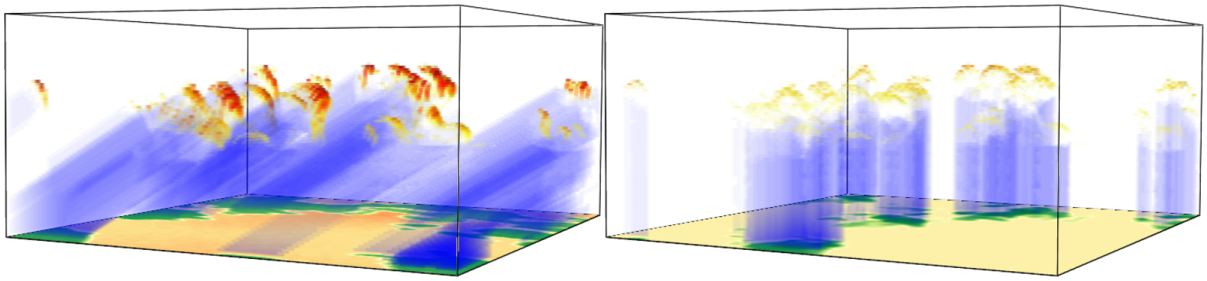

Figure 2.18: *Solar heating rate and net surface flux distribution for realistic cumulus cloud field (I3RC; Cahalan et al., 2005) when the Sun is shining from the side in the 3-D MYSTIC (left panel) and ICA two-stream (right panel) radiation calculation. The color shading is the same as in Fig. 2.17. Source: Jakub (2016).*

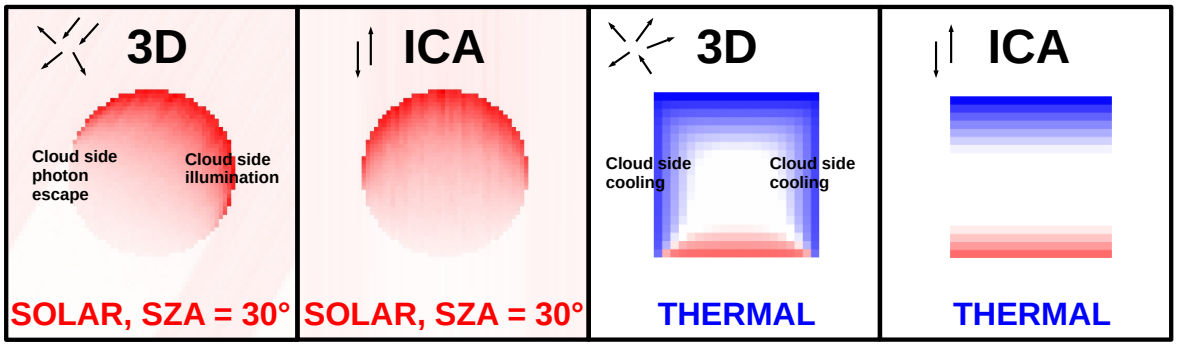

Figure 2.19: *Illustration of the main differences between the 3-D and ICA radiation calculation for idealized clouds characterized by constant optical properties. The two panels on the left show solar heating rate distribution for a solar zenith angle of 30° for an idealized spherical cloud. The two panels on the right show thermal heating rate distribution for an idealized cuboid cloud. Shown is vertical cross-section through the cloud center. Red color denotes heating, whereas blue color denotes cooling, with darker red/blue shading denoting stronger heating/cooling. Marked are classic 3-D cloud-radiative effects, which are misrepresented in the ICA.*

optical properties. In realistic atmospheric configurations these effects are most pronounced in regions with largest horizontal gradients of optical properties, which are indeed the cloud side (lateral) areas. Similar phenomena, nevertheless, are naturally observed also in the interior of individual clouds predominantly in regions characterized by profound horizontal cloud variations. Further mechanisms underpinning the radiative effects related to horizontal photon flow in a heterogeneous medium are described by Várnai and Davies (1999).

2.4.3 Controlling parameters

The exact nature of cloud-radiation interaction depends on various parameters. An important circumstance is the already mentioned solar zenith angle, which controls the direction and the strength of incident solar beam (an illustration of how cloud side illumination varies with SZA is shown in Fig. 2.20). Another environmental property, which exerts a major influence on atmospheric radiative transfer is the ground albedo. Whereas the Earth's surface is frequently assumed to be black for the interaction with thermal radiation, the ground reflectivity in the solar spectral range generally spans a wide range of values. As an illustration, oceanic albedo is profoundly lower than global land albedo (Li et al., 2006; Zhang et al., 2010; He et al., 2014; Hogan and Bozzo, 2015). Since ground surfaces with larger albedo reflect greater amount of the incoming solar radiation back towards the space, this does not only exert a direct control on the surface energy budget, but also increases the chance for radiation to reinteract with the cloud layer. The essentials of cloud-radiation interaction, moreover, primarily depend on multiple characteristics of cloud fields themselves – e.g., cloud cover, cloud optical thickness, cloud geometry and cloud heterogeneity (e.g., Di Giuseppe and Tompkins, 2003a,b, 2005; Cairns et al., 2000; Carlin et al., 2002). The cloud geometry, as an illustration, is commonly described by cloud aspect ratio (Di Giuseppe and Tompkins, 2003b). The latter is maximized for vertically developed deep convective regimes and minimized for horizontally extensive sheets of stratiform cloudiness. It is hence straightforward to imagine that cloud side area and thereby the significance of 3-D radiative transfer is markedly larger for deep regimes than for stratiform scenarios. Similarly, vast fields of broken shallow cumulus exhibit large cumulative cloud side area and are thereby a critical subject to one-dimensional radiative transfer approximations (e.g., Klinger et al., 2017; Jakub and Mayer, 2017). The nature of the realistic cloud-radiation interaction and henceforth the extent of the radiative biases as a function of various parameters outlined above will be additionally investigated within the scope of this thesis.

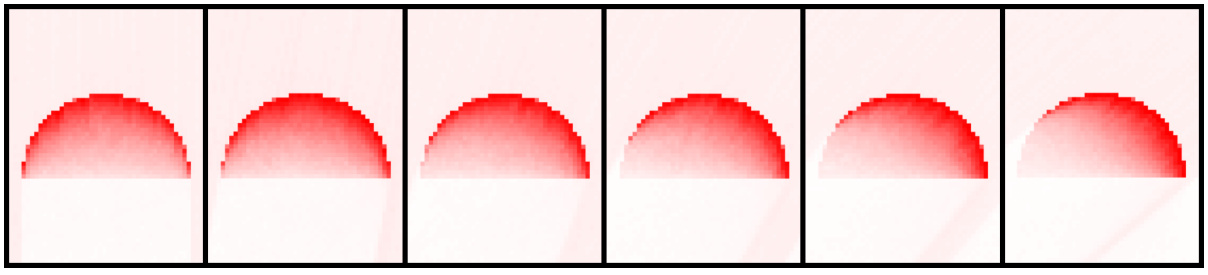

Figure 2.20: *Solar heating rate as a function of SZA for an idealized half-spherical cloud with constant optical properties in the 3-D radiation calculation. SZA is varied from 0° (leftmost panel) to 50° (rightmost panel) with a step of 10°. Shown is vertical cross-section through the center of the cloud. The darker/lighter red shading denotes larger/smaller heating rate. Source: Prof. Dr. Bernhard Mayer (personal correspondence).*

2.5 Radiation schemes: treatment of cloud horizontal inhomogeneity

Radiation schemes in coarse-resolution global numerical weather prediction and climate models, commonly referred to as GCMs, have traditionally been claimed to be impaired by the poor representation of clouds (Randall et al., 1984, 2003, 2007). This section aims at more thoroughly reviewing the past and current treatment of unresolved cloudiness in GCM radiation parameterizations, focusing on the issues related to cloud horizontal inhomogeneity representation. It commences with summarizing the conventional GCM cloud representation. Subsequently it introduces the methodologies to reduce the biases arising from horizontally homogeneous cloud assumption, such as the state-of-the-art McICA algorithm (Barker et al., 2002; Pincus et al., 2003) and finally exposes its alternative − the Tripleclouds concept.

2.5.1 Conventional cloud representation

Undoubtedly, one of the most rigorous assumptions that persisted in GCMs for multiple decades, was the complete removal of cloud horizontal heterogeneity − the conventional *horizontally homogeneous cloud representation* (Fig. 2.21, left panel). Since the nature of cloud-radiation interactions is intrinsically nonlinear, the homogeneous representation of clouds leads to substantial biases of GCM radiative quantities (Cahalan et al., 1994a,b; Cairns et al., 2000). Further, as previously pointed out, an assumption of how partial cloudiness vertically overlaps within each GCM grid column is required. The conventional assumption is the maximum-random overlap, advocated by many studies (e.g., Geleyn and Hollingsworth, 1979) and recently criticized by others, since it breaks down in the case of vertically developed cloud systems in strongly sheared environments (e.g., Di Giuseppe and Tompkins, 2015). Last but not least, the 3-D radiative effects related to the subgrid horizontal photon transport, which in reality manifests itself most pronouncedly in regions characterized by strong horizontal gradients of optical properties such as cloud side boundaries, were traditionally neglected and are currently still disregarded in the majority of GCMs. This broad palette of problems is challenging to tackle and solve.

2.5.2 Methodologies to reduce cloud inhomogeneity biases

In order to reduce the most striking biases stemming from cloud horizontal inhomogeneity, several methods were developed in the past. The scaling factor method, proposed by Cahalan et al. (1994a) and implemented in the European Centre for Medium-Range Weather Forecasts (ECMWF) model by Tiedtke (1996), was a conventional approach, where the cloud optical depth was multiplied by a constant scaling factor and the resulting effective optical depth was passed to the radiation scheme. Oreopoulos and Barker (1999) introduced a more sophisticated gamma-weighted radiative transfer scheme, later applied also by Carlin et al. (2002) and Rossow et al. (2002), where the optical depth across a grid box

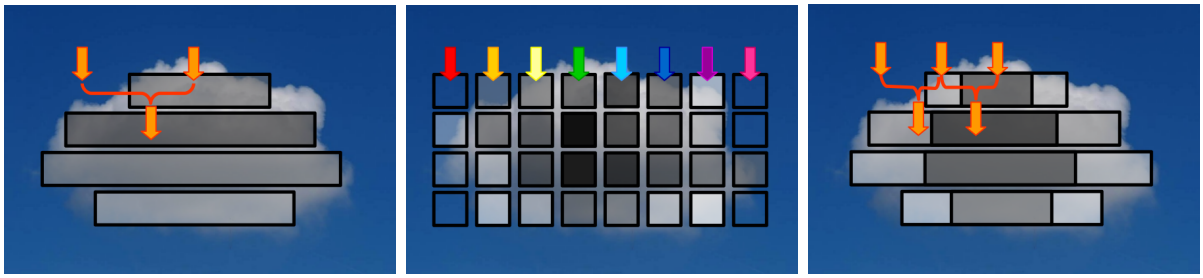

Figure 2.21: *Divergent modeling of cloud-radiation interaction in weather and climate models (arrows denote radiative fluxes, grey shading mirrors cloud optical thickness): the conventional approach (left panel), the McICA algorithm (middle panel; rainbow-colored radiative fluxes indicate calculations in various spectral bands) and the Tripleclouds methodology (right panel).*

is weighted using a gamma distribution. Moreover, Barker et al. (2002) and subsequently Pincus et al. (2003) presented an alternative technique, known as the McICA (Monte Carlo integration of Independent Column Approximation; Fig. 2.21, middle panel), which is currently operationally employed in most large-scale atmospheric models. The fundamental assumption of the McICA is that the ICA approximation is adequate and therefore allows for the independent generation of subgrid cloudy columns, which is managed by means of stochastic cloud generator (Räisänen, 2004; Räisänen and Barker, 2004). As the full ICA is not affordable within the computational constraints of simulating complex weather and climate scenarios, the computational speed gain in the McICA approach is based on the simultaneous sampling of subgrid cloud state and spectral interval.

Whereas all aforementioned methodologies certainly brought improvements compared to the conventional GCM cloud representation, they all have their disadvantages. The usage of the McICA algorithm, for example, introduces conditional random errors (the McICA noise) to radiative quantities, and it is unclear how significantly this affects the forecast skill. Räisänen et al. (2007), as an illustration, investigated the impact of the McICA noise in an atmospheric GCM (ECHAM5; Roeckner et al., 2003) and found statistically discernible impacts on simulated climate for a fairly reasonable McICA implementation. The largest effect was observed in the boundary layer, where clouds are essentially maintained by local cloud top radiative cooling. As the McICA noise disrupted this cooling, a positive feedback loop was induced, where a reduction of cloud fraction led to weaker radiative cooling, which in turn further diminished the cloud fraction. Similar findings were already previously reported by Räisänen et al. (2005) for global climate simulated with another GCM.

2.5.3 The advent of the Tripleclouds concept

A few years after the introduction of the McICA, SH08 proposed a unique method, which utilizes two regions in each vertical model layer to represent the cloud, as opposed to one. One region is used to represent the optically thicker part of the cloud and the other

represents the remaining optically thinner part − the method therefore captures cloud horizontal inhomogeneity. Together with the cloud-free region, the radiation scheme thus has three regions at each height and is referred to as the Tripleclouds (TC) scheme. In the primary work of SH08 the layer cloudiness was split into two equally sized regions and the corresponding pair of cloud condensates (e.g., LWC) was generated on the basis of known LWC distribution. The method was initially tested on high-resolution radar data, where the exact position of the three regions was passed to the radiative solver, capable of representing an arbitrary vertical overlap. In practice, a host GCM model usually provides only mean LWC and no information about vertical cloud arrangement. In order to make the method applicable to GCMs, Shonk et al. (2010) derived a global estimate of cloud horizontal variability in terms of fractional standard deviation (FSD), which can be used to split the mean LWC into two components along with the LWC distribution assumption. Further, they incorporated a generalized vertical overlap parameterization, namely the exponential-random overlap, accounting for the aforementioned problematics in strongly sheared conditions. In the second part of this study (Shonk and Hogan, 2010) the effect of improved horizontal and vertical cloud structure on global radiation budget was quantified. As anticipated, the greatest effect of cloud horizontal inhomogeneity was identified in areas of marine stratocumulus, whereas the largest impact of revised vertical overlap was observed in regions of deep tropical convection. Recently, the method was implemented in the *ecRad* package (Hogan and Bozzo, 2018), the current radiation scheme of ECMWF Integrated Forecast System (IFS). In contrast to the McICA, which is still operational also at ECMWF due to its higher computational efficiency, the TC scheme does not produce any radiative noise (Fig. 2.22). As suggested by Hogan and Bozzo (2016), this superiority could become even more valuable in the future if an alternative gas-optics model with fewer spectral intervals than the current Rapid Radiative Transfer Model for GCMs (RRTMG; Mlawer et al., 1997) will be developed, since this would increase the level of the McICA noise, but it would not affect Tripleclouds. In other words, in order to limit the McICA noise in this case, oversampling of each interval would be required, which could increase the computational cost of the McICA to a similar degree as that of the Tripleclouds scheme.

Before the TC radiative solver can be operationally employed, however, it has to be further validated. Whereas all previous studies employing the TC scheme examined primarily the top-of-the-atmosphere (TOA) radiation budget, the present work is aimed at evaluating the atmospheric heating rate and net surface flux. To that end, building upon the Tripleclouds idea of SH08, the δ-Eddington two-stream method for one cloud-free and two cloudy regions at each height (Fig. 2.21, right panel) was constructed within the scope of this thesis. The present TC implementation is presented in the methodology chapter.

2.5.4 Existing Tripleclouds condensate pair generation methods

In order to apply the Tripleclouds radiative solver, a pair of cloud condensates characterizing optically thick and thin cloudy regions, referred to as the LWC^{ck} (Cloud thicK) and LWC^{cn} (Cloud thiN), needs to be created in each vertical layer. To that end, we first re-

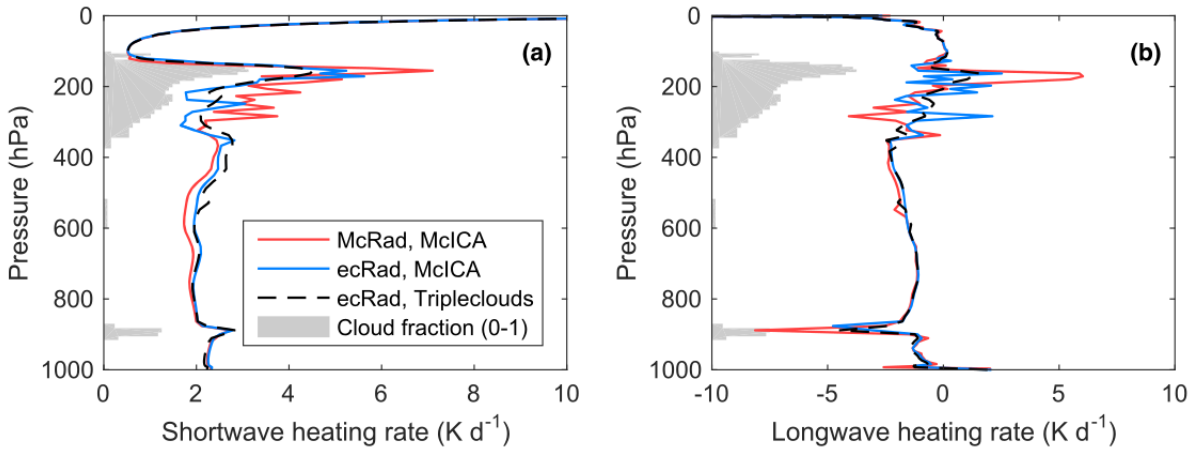

Figure 2.22: *Solar (left panel) and thermal (right panel) heating rate profile comparing the McICA and the Tripleclouds radiation scheme (SH08) as implemented in the ecRad radiation package. Shown is also the result of the previous McICA implementation within an older version of the radiation package at ECMWF (McRad, Morcrette et al., 2008). Although the amount of Monte Carlo noise in the McICA profiles reduced during the course of the solver optimization process, it remains substantial compared to noise-free Tripleclouds solution. Source: Hogan and Bozzo (2018).*

vise the original Tripleclouds approach introduced in SH08, later referred to as the "lower percentile method" (Shonk et al., 2010), which can only be applied if the LWC distribution is known. We then summarize the more practical "fractional standard deviation method" (Shonk et al., 2010).

Lower percentile method

In this method, it is assumed that the LWC distribution in each vertical layer can be approximated with the normal distribution:

$$p(LWC) = \frac{1}{\sqrt{2\pi}\sigma_{LWC}} \exp\left[-\frac{(LWC - \overline{LWC})^2}{2\sigma_{LWC}^2} \right], \tag{2.36}$$

where $\overline{LWC}$ is layer mean LWC and σ_{LWC} is its standard deviation. The distribution of LWC is divided into two regions through a given percentile of the distribution, denoted as "split percentile (SP)". The latter is chosen to be the 50th percentile or the median, which splits the cloud volume into two equal parts (cloud fraction in each vertical layer is halved). The LWC of the optically thin cloud (LWC^{cn}) is determined as the value corresponding to the so-called "lower percentile (LP)" of the distribution. This is chosen to be the 16th percentile based on the following considerations. We adjust the two LWC values in a way that the mean LWC in the layer is conserved:

$$\overline{LWC} = \frac{LWC^{ck} + LWC^{cn}}{2}, \tag{2.37}$$

and that they are separated by two standard deviations:

$$LWC^{ck} - LWC^{cn} = 2\sigma_{LWC}. \tag{2.38}$$

For a Gaussian distribution, the latter constraint has a desired property that the variability within each of the two cloudy regions (measured by σ_{LWC}) is the same as that within the entire cloud in the layer. Equations (2.37) and (2.38) give the following relationship for LWC^{cn}:

$$LWC^{cn} = \overline{LWC} - \sigma_{LWC}. \tag{2.39}$$

The fraction of the distribution with LWC lower than LWC^{cn} is therefore:

$$f_{cn} = \int_{-\infty}^{LWC^{cn}} p(LWC)dLWC = 0.159, \tag{2.40}$$

which corresponds to the LP of 16. Finally, the LWC^{ck} is determined using Eq. (2.37) to conserve the mean.

It should be noted that the choice of the 16th percentile as the lower percentile and the 50th percentile as the split percentile is based solely on theoretical considerations. In practice, the LP and SP are the two tunable parameters, that can be adjusted according to their performance on real cloud data. Even though the optimal setting varies, SH08 exposed that the combination of LP of 16 and SP of 50 generally serves well in both solar and thermal spectral range for vast ranges of cloud data.

Fractional standard deviation method

This method in its initial formulation by Shonk et al. (2010) implicitly assumes that LWC is normally distributed as well: the cloudiness in each vertical layer is partitioned into two regions of equal size and the pair of LWC (LWC^{ck}, LWC^{cn}) is obtained by:

$$LWC^{ck,cn} = \overline{LWC} \pm \sigma_{LWC} = \overline{LWC}(1 \pm FSD), \tag{2.41}$$

where FSD represents the fractional standard deviation of LWC:

$$FSD = \frac{\sigma_{LWC}}{\overline{LWC}}. \tag{2.42}$$

Since in practice only $\overline{LWC}$ is known within a GCM grid box, the FSD has to be parameterized. A review of numerous studies carried out by Shonk et al. (2010) gave a globally representative FSD of 0.75 ± 0.18.

If the subgrid cloud condensate is normally distributed, subtracting σ_{LWC} from the $\overline{LWC}$ to obtain the LWC^{cn} in Eq. (2.41) corresponds approximately with the 16th percentile of the distribution. For more realistic lognormal and gamma distributions, the 16th percentile (advocated by SH08) is given by relationships presented in Hogan et al. (2016, 2019). The splitting principles for various distributional assumptions as applied in the present work shall be further addressed in the following methodology chapter.

Chapter 3

Data and methodology

3.1 Cloud data

We first present a set of shallow cumulus clouds used to quantify the radiative bias in numerical models at regional scale. In the subsequent section cloud field case studies used to explore the Tripleclouds potential at global scale are introduced.

3.1.1 Evolving shallow cumulus cloud field

Input for offline regional-scale radiation calculations is a set of shallow cumulus cloud fields, simulated with the University of California, Los Angeles large-eddy simulation (UCLA-LES) model (Stevens et al., 2005; Stevens, 2007). The simulation relates to the Rain in Cumulus over the Ocean (RICO, Rauber et al., 2007) campaign. The horizontal domain size is 6.4 x 6.4 km^2, with the vertical extent of the domain being 4 km. A constant model grid spacing of 25 m is used in all three (x-, y-, z-) directions. A 3-D distribution of cloud liquid water content was extracted from the simulation run and the corresponding effective radius was parameterized according to Bugliaro et al. (2011). For our analysis we choose a set of ten cloud scenes (depicted in Fig. 3.1) from the initial 8 hours of simulation in a way that total cloud cover of the scene is varied between ∼10 % and ∼100 % approximately with a step of 10 %. Thus the evolving cloud field comprises examples of broken cumulus as well as more uniform stratocumulus clouds. These cloud scenes have highly variable optical thickness, with a maximum vertically integrated optical thickness of ∼20, ∼80 and ∼230 corresponding to scenes with total cloud cover of ∼10 %, ∼50 % and ∼100 %, respectively.

3.1.2 Cloud field case studies

Data for global-scale radiative transfer experiments is a set of 3-D highly resolved inhomogeneous cloud fields, defined in terms of LWC and IWC distributions as well as the assigned effective radii (Bugliaro et al., 2011). Compared to the evolving shallow cumulus cloud field introduced above, the cloud field case studies are prescribed on somewhat larger domains, allowing to investigate the radiative effects at the scale of global models.

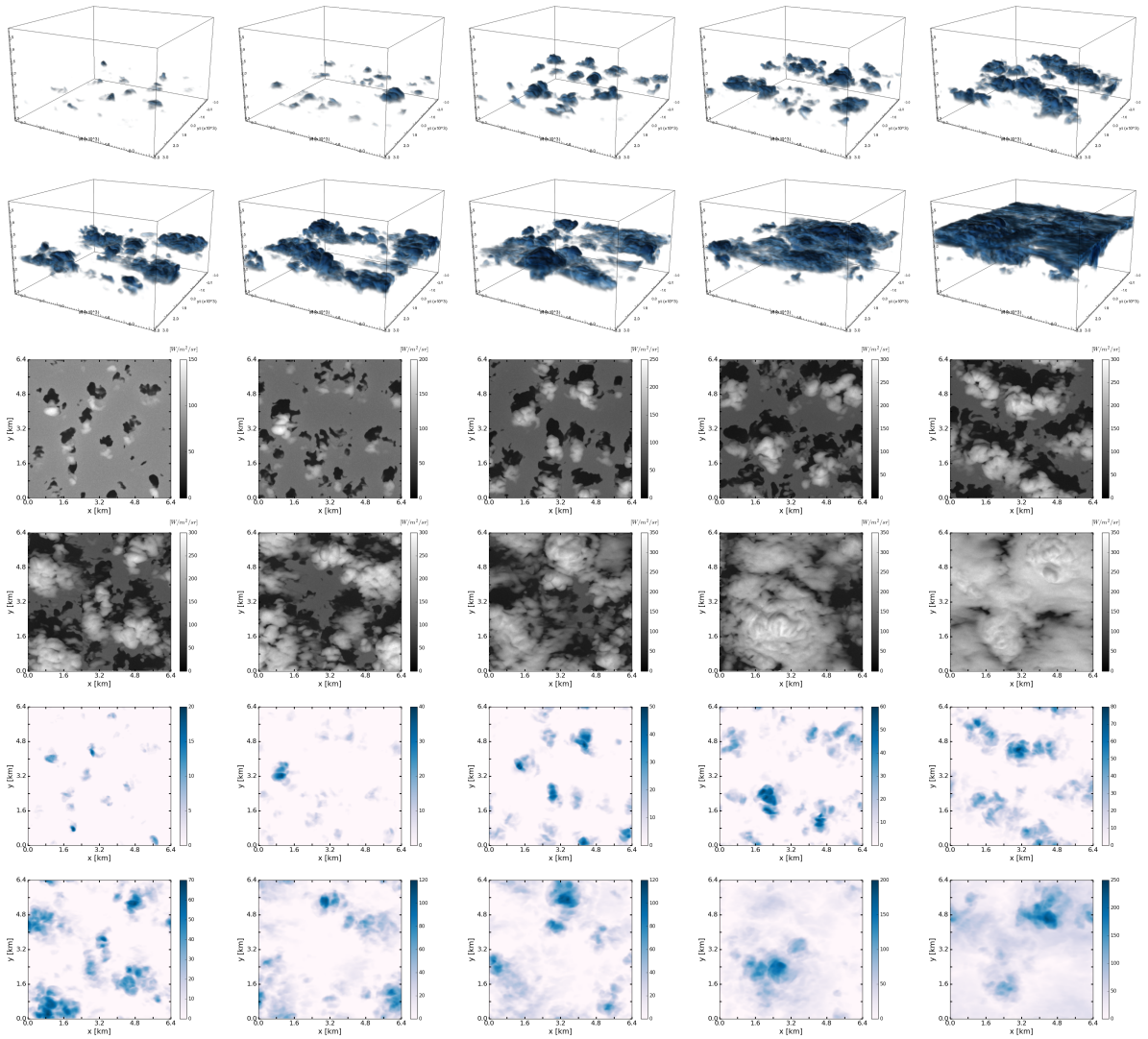

Figure 3.1: *A set of shallow cumulus cloud scenes used as input for radiative transfer calculations. Top – visualization with VisIt (Childs et al., 2012). Middle – visualization with MYSTIC, shown is nadir radiance distribution at a height of 5 km with the Sun under a zenith angle of 30° illuminating the scenes from the south. Bottom – vertically integrated cloud optical thickness.*

Diverse models employed to generate these cloud fields, together with different resolutions, result in inherently distinctive cloud structures and hence ensure that the four selected cases comprise a wide range of inhomogeneity. It should be noted that these case studies were intentionally chosen as scenarios arising from minimal vertical wind shear conditions, enabling to focus on cloud horizontal heterogeneity effects. In the following, each cloud type is characterized briefly.

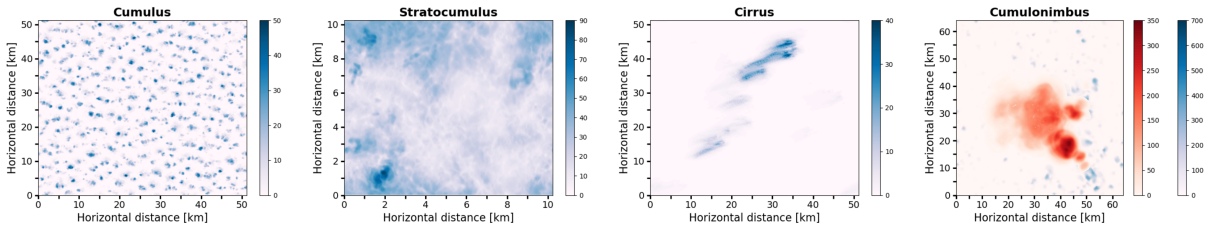

Figure 3.2: *Vertically integrated optical thickness of selected cloud field case studies. Note that for cumulonimbus, the blue/red shading denotes optical thickness of liquid/ice phase.*

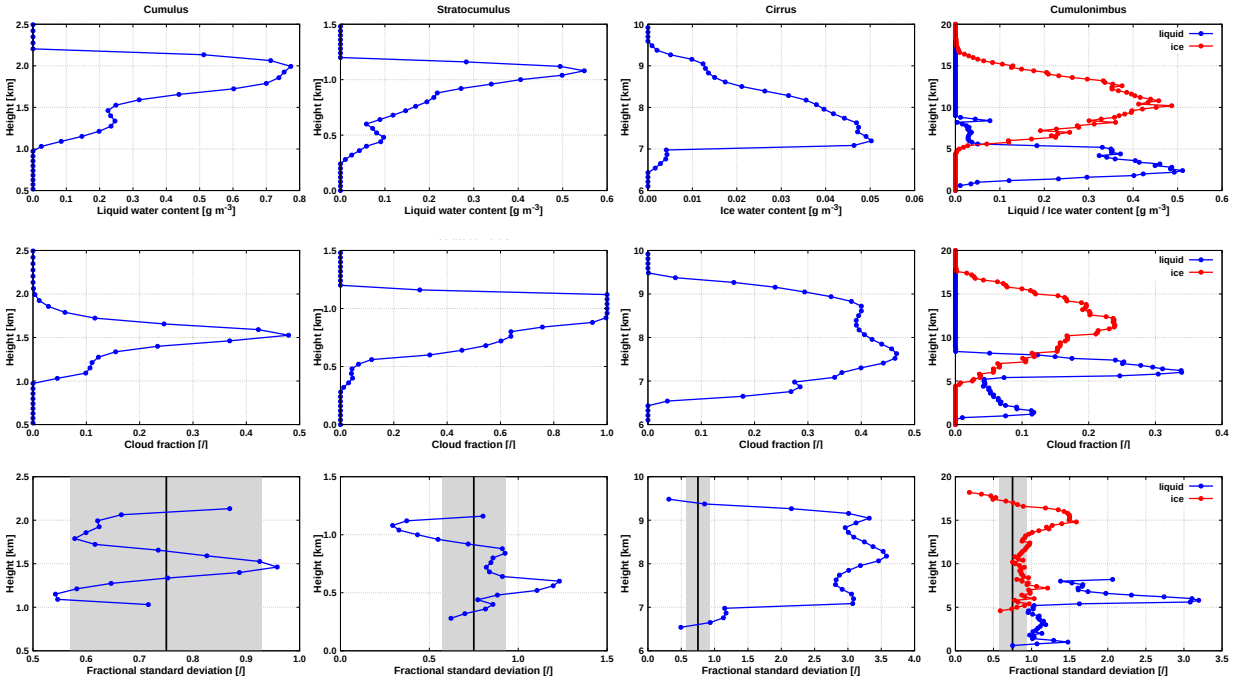

Figure 3.3: *Characterization of selected cloud field case studies in terms of averaged LWC/IWC (top row), cloud fraction (middle row) and fractional standard deviation of LWC/IWC (bottom row), whereby the vertical black line shows the mean global FSD estimate and the grey shaded area denotes its uncertainty.*

Cumulus

The shallow cumulus cloud case study was also simulated with the UCLA-LES model. The horizontal domain size is 51.2 x 51.2 km^2, with the vertical extent of the domain being 3.5 km. A constant horizontal grid spacing of 100 m is applied, whereas the vertical grid spacing is variable ranging from 50 m at the ground to 84 m at domain top. Further details about the UCLA-LES setup can be found in Jakub and Mayer (2017). Figure 3.2 (first panel) shows vertically integrated cloud optical thickness, demonstrating that optically thicker regions are located in the interior of individual clouds, which conforms to the core-shell model (see also Fig. 3.4). Vertical profiles of averaged LWC, cloud fraction (defined

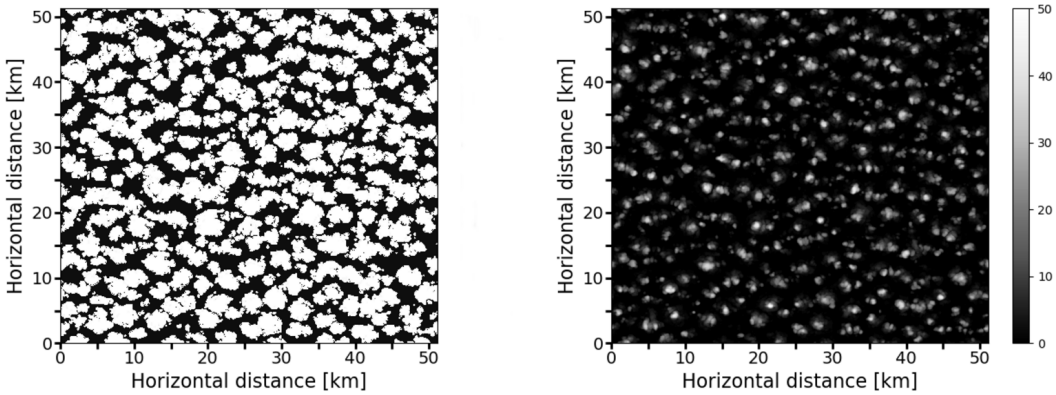

Figure 3.4: *Horizontal heterogeneity for cumulus case study. Left – cloud mask (clouds in white, clear sky in black). Right – vertically integrated cloud optical thickness, highlighting solely optically thicker convective cores.*

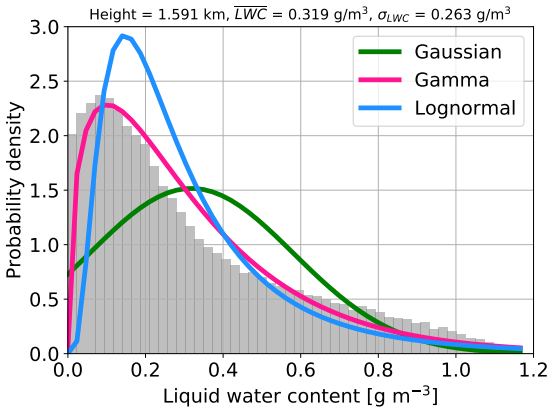

Figure 3.5: *Actual LWC probability density in the central part of the cumulus cloud layer and distributional fits.*

by LWC $> 10^{-3}$ g m^{-3}) and FSD are shown in Fig. 3.3 (first column). Although the FSD is strongly dependent on the position within the cloud layer, it predominantly lies within the range of global estimate, with its height-averaged value of 0.71 being close to the mean global estimate.

To gain further insight about the subgrid cloud variability, the theoretical distributions (Gaussian, gamma, lognormal; see also Appendix A) were fitted to the actual LWC distribution in each vertical layer (as illustrated in Fig. 3.5). The Kolmogorov-Smirnov test (Conover, 1971; Wilks, 1995) was used to assess the goodness of fit. It was found that the actual LWC distribution is best approximated with the gamma distribution (best fit in 55 % of the cloudy layers), followed by the lognormal distribution, whereas the Gaussian distribution always ranked worst. Precisely, the gamma distributional fit performed best throughout the central part of the cumulus layer, where cloud-radiative effect is maximized.

Stratocumulus

The stratocumulus cloud was simulated with the UCLA-LES model as well, whereby the simulation relates to the Atlantic Stratocumulus Transition Experiment (ASTEX; Albrecht et al., 1995a), conducted over the northeast Atlantic Ocean in June 1992 (Wood, 2012). The case study thereby exemplifies a marine boundary layer stratocumulus, exhibiting sporadic convective cells embedded in the stratus layer (Agee et al., 1973; Atkinson and Zhang, 1996; Wood and Hartmann, 2006; Wood, 2012). Observational studies show, inter alia, that directional and magnitude vertical shear is small in mesoscale cellular convection (Agee et al., 1973). The horizontal domain size is 10.24 x 10.24 km^2, with the vertical extent of the domain being 4 km. A constant model grid spacing of 40 m is applied in all three (x-, y-, z-) directions. Figure 3.2 (second panel) visualizes the cloud field in terms of vertically integrated optical thickness. Vertical profiles of averaged LWC, cloud fraction (defined by LWC $> 10^{-3}$ g m^{-3}) and FSD are shown in Fig. 3.3 (second column). The overcast stratocumulus scene is topped slightly above 1 km height. The FSD, although roughly centered around the global estimate, is strongly dependent on the vertical position within the cloud layer: it exhibits a maximum (1.2) in the lowest portion of the cloud layer and a minimum (0.3) in the uppermost radiatively important region. Furthermore, it is found that the actual LWC distribution throughout the vast majority of the uppermost part of the stratocumulus layer, where radiative effect is maximized, is best approximated with lognormal distribution (best fit in 5/8 of top layers).

Cirrus

The cirrus cloud was generated with the stochastic cloud model Cloudgen of Hogan and Kew (2005), described also in Zhong et al. (2008). The speciality of this 3-D cirrus fractal model is its capability to generate structural features unique to cirrus clouds: realistic fallstreak geometry and shear-induced mixing. The model input parameters are based on the statistics derived from radar observations in southern England (Hogan et al., 2003; Hogan and Illingworth, 2003). We chose the cirrus uncinus case study of June, 24th, 1999, which is the first of the three cases discussed by Hogan and Kew (2005) and subsequently also by Zhong et al. (2008)[1] [2], and was adopted herein as it is the case with smallest vertical wind shear. The horizontal domain size is 51.2 x 51.2 km^2 with a grid spacing of 100 m. The vertical extent of the domain is 7 km using constant vertical grid spacing of 109 m. Figure 3.2 (third panel) visualizes the cloud field in terms of vertically integrated optical thickness. Vertical profiles of averaged IWC, cloud fraction (defined by IWC $> 10^{-3}$ g m^{-3}) and FSD are shown in Fig. 3.3 (third column). The degree of cloud horizontal heterogeneity is largest in the central part of the cloud layer, with FSD exceeding 3.5. The cirrus layer is thus by far not uniform, rather it exhibits cellular structures ("generating

[1] The studies of Hogan and Kew (2005) and Zhong et al. (2008) used coarser horizontal grid resolution (1.56 km).

[2] Hogan and Kew (2005) showed that for this particular cirrus case study, the maximum-random overlap assumption performs reasonably well in both the solar and thermal spectral range.

cells"), which would in reality be associated with convective motions. The latter produce higher supersaturations (Heymsfield, 1977) and increase cirrus ice crystal residence time (Mitchell, 1994), which leads to an increased IWC within the cells. The layer IWC of the present cirrus is lognormally distributed, since this is the intrinsic Cloudgen property.

Cumulonimbus

The cumulonimbus cloud was simulated with the Goddard Cumulus Ensemble cloud resolving model (GCE-CRM), described in detail by Tao and Simpson (1993) and more recently by Tao et al. (2003). The simulation relates to the convective event observed on 23 February 1999 during the Tropical Rainfall Measuring Mission (Simpson et al., 1988, 1996) Large-Scale Biosphere-Atmosphere Experiment in Amazonia (TRMM-LBA). The horizontal domain size is 64.0 x 64.0 km^2, with the vertical extent of the domain being 23 km, which is sufficient to allow the growth of tropical cirrus anvil. The grid spacing of 250 m is applied in each horizontal direction and 200 m in the vertical direction. The simulation is described by Lang et al. (2007) and briefly by Zinner et al. (2008). Due to light environmental winds (Fig. 2b of Lang et al., 2007), the convection was rather weakly organized[3]. Figure 3.2 (fourth panel) visualizes the cloud field in terms of vertically integrated optical thickness. Vertical profiles of averaged LWC and IWC, the corresponding cloud fraction as well as FSD are shown in Fig. 3.3 (fourth column). The case study is characterized by three distinct cloud layers: a liquid phase region extending from 0.8 km to 4.4 km consisting of shallow cumuli, a mixed-phase stratiform region located between 4.4 km and 8.2 km, and an ice phase region extending from 8.2 km to 17.4 km height, encompassing the cumulonimbus deep convective core and the anvil. Remarkably, the stratiform layer is highly heterogeneous, with the maximum FSD of the liquid phase exceeding 3.2. The maximum FSD in the bottommost cumuliform region as well as in the uppermost anvil region reaches approximately half of this value.

The comparison of theoretical distributions with actual LWC/IWC distributions reveals the following findings: the assumption of Gaussianity is void for the present cumulonimbus scenario and in each vertical layer either gamma or lognormal distribution was classified as the best fit. Thus, throughout the majority of the liquid region the actual LWC distribution is best approximated with the gamma distribution (best fit in 58 % of layers). In the mixed-phase region the LWC distribution is best approximated with the lognormal distribution (best fit in 85 % of layers), whereas the IWC distribution is best approximated with the gamma distribution (best fit in 85 % of layers). In the ice region the IWC distribution is best approximated with the gamma distribution within the bottommost 30 % and uppermost 13 % of the region (best fit in all cases), while within the remaining central part the lognormal distribution appears to be the optimal approximation (best fit in 58 % of layers).

[3]The fact that the deep convective cloud is practically not sheared, makes it a perfect target to study the performance of our current Tripleclouds implementation, which is not yet capable of representing an arbitrary vertical overlap.

3.2 Radiative transfer models

The radiative transfer experiments were performed using the *libRadtran* radiative software package (www.libradtran.org; Mayer and Kylling, 2005; Emde et al., 2016), which contains several radiative transfer solvers. In this section we first introduce the Monte Carlo radiation model, which is the key feature of the package and was used for 3-D benchmark and associated ICA calculations. Further, we explain the δ-Eddington two-stream method (also previously contained in *libRadtran*) and its extension to support maximum-random overlap assumption for partial cloudiness, which was accomplished in the frame of this dissertation. Finally, we present the Tripleclouds radiative solver, which was as well developed within the scope of this thesis. Further technical instructions regarding the usage of both newly implemented solvers in the *libRadtran* framework are provided in Appendix B.

3.2.1 Three-dimensional Monte Carlo radiative model

The benchmark experiments were performed with the 3-D radiative transfer model MYSTIC, the Monte Carlo code for the physically correct tracing of photons in cloudy atmospheres (Mayer, 1999, 2000, 2009). MYSTIC participated in both phases of the international Intercomparison of 3-Dimensional Radiation Codes (Cahalan et al., 2005), where it proved its ability to accurately compute radiative transfer in versatile cloud scenarios.

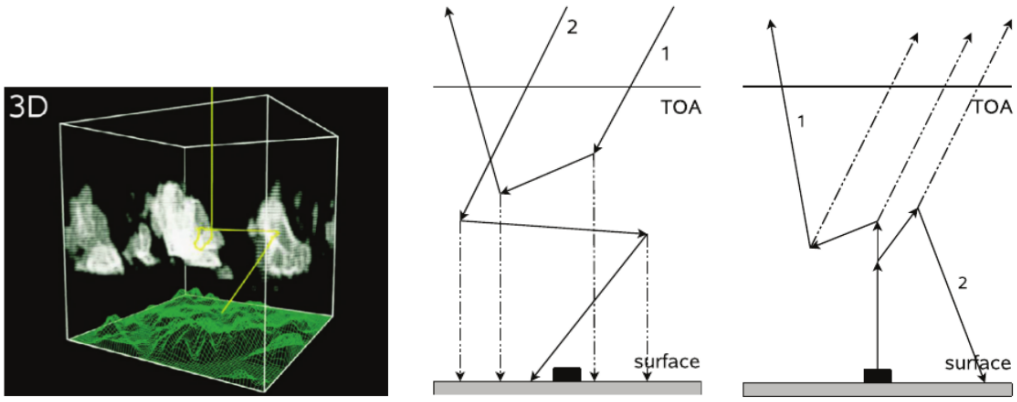

Figure 3.6: *Online visualization of a MYSTIC simulation (left panel). Forward (middle panel) and backward (right panel) Monte Carlo technique. Source: Mayer (2009).*

The elementary principles of Monte Carlo radiative transfer modeling and it's MYSTIC implementation will be described in the following. For a comprehensive explanation, the reader is referred to further literature (Mayer, 2009; Marshak and Davis, 2005). The Monte Carlo approach to radiative modeling has several advantages, starting from the basic fact that the radiative transfer equation can be solved even without knowing it, but strictly focusing on individual physical processes (emission, scattering, absorption), which enables a fairly uncomplicated covering of arbitrary complex 3-D inhomogeneous cloud and orography scenarios. The model domain is defined on a 3-D rectangular grid, whereby

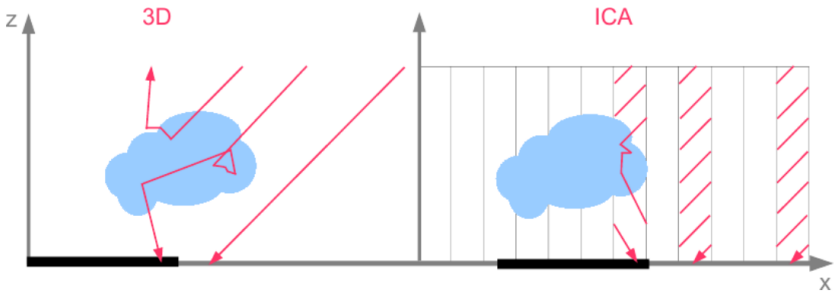

Figure 3.7: *Three-dimensional (left) and ICA (right) Monte Carlo radiative modeling.*

each grid box contains information about molecule, cloud droplet, ice crystal and aerosol particle radiative properties. The Monte Carlo method relies on tracing photons from their source to destination, using a random number generator for simulating heuristic decisions at several stages of the photon journey. The solar photons enter the model domain at its top at a random (x-, y-) location and at a given entry direction, specified by the solar zenith and azimuth angles. The thermal photons are emitted from a random location in the atmosphere or the Earth's surface, depending on the temperature and emission coefficient. The initial photon direction is random, since thermal emission is isotropic. The photon life during its travel path consists of a set of repeatable events – whether scattering or absorption occurs. The decision which interaction takes place is simulated by another random number being compared with the single scattering albedo of the particular grid box. The absorption process is in principle fairly simple, since the photon "dies". Instead of computationally inefficient killing of absorbed photons, however, the photon lifetime is rather simulated by applying a fictional photon weight, being reduced during the photon path regarding the traversed optical thickness. The scattering event, on the other hand, solely changes the photon flight direction, but it conserves energy. To determine the new photon direction, the scattering angle is sampled utilizing the phase function information, while the azimuth angle is randomly drawn. The periodic boundary conditions at domain lateral margins ensure that a photon exiting the domain at one side is mirrored to reenter the domain on the opposite side. If the photon hits the ground, it can be either reflected or absorbed. The photon tracing otherwise terminates if the photon exists the model atmosphere at TOA.

The accuracy of the Monte Carlo radiative quantities is heavily correlated with the number of injected photons traced. Increasing the total number of photons reduces the resulting error – the Monte Carlo noise. Since implementing the Monte Carlo technique requires significant computational resources, several optimizing solutions were introduced in the past. As such, opposed to the standard forward photon tracing summarized above, the backward photon tracing (Emde and Mayer, 2007; Klinger and Mayer, 2014) is appealing, which is physically justified by the Helmholtz reciprocity principle (von Helmholtz and König, 1896). In this case, the photons are fictively traced from the destination back to source, which is especially beneficial for short thermal photon trajectories due to large atmospheric optical thickness in thermal part of the spectrum. The backward tracing is

thus a powerful methodology if one is interested in knowing the result only at a specific location (e.g., the cloud volume). Both fundamental photon tracing principles are illustrated in Fig. 3.6. It should be reminded that despite introduced optimizations, the Monte Carlo modeling is computationally not affordable for operational usage in numerical weather and climate prediction, but it is a highly valuable tool for offline research benchmark radiation calculations.

Alternatively, MYSTIC can be run in ICA mode as well, whereby periodic boundary conditions are imposed on each individual domain grid column (Fig. 3.7), preventing horizontal photon exchange between the columns. The 3-D and ICA configurations enable to conveniently investigate radiative effects of horizontal photon transport, which is customarily neglected in atmospheric dynamical models.

3.2.2 δ-Eddington two-stream method with maximum-random overlap

We begin by introducing the classic δ-Eddington two-stream method (Joseph et al., 1976; Zdunkowski et al., 2007) suitable for a horizontally homogeneous model atmosphere and then explain the extension of this method which accounts for partial cloudiness.

δ-Eddington two-stream method

In summary, the common feature of two-stream methods is the division of the radiation field into direct solar beam (S) and two streams of diffuse radiation − the downward ($E_{\downarrow}$) and upward ($E_{\uparrow}$) component. For most applications, δ-TSMs, in which a part of the scattered radiation is retained in the direct beam to approximate the strong forward-scattering peak of cloud droplets and aerosol particles, have been found to be more accurate than two-stream methods without δ-scaling (Räisänen, 2002). The fractional scattering into the forward peak taken to be the square of the phase function asymmetry parameter is what distinguishes the widespread δ-Eddington approximation from others of similar nature.

For the calculations in a vertically inhomogeneous atmosphere, the atmosphere is discretized into a number of homogeneous layers, each characterized by its optical properties (optical thickness, single scattering albedo, asymmetry parameter). Consider first a single layer (j) located between levels $(i-1)$ and (i), as depicted in Fig. 3.8[4]. A system of linear equations determining the fluxes that emanate from this layer as a function of fluxes that enter the layer can be written in matrix form as:

$$\begin{pmatrix} E_{\uparrow}(i-1) \\ E_{\downarrow}(i) \\ S(i) \end{pmatrix} = \begin{pmatrix} a_{11} & a_{12} & a_{13} \\ a_{12} & a_{11} & a_{23} \\ 0 & 0 & a_{33} \end{pmatrix} \cdot \begin{pmatrix} E_{\uparrow}(i) \\ E_{\downarrow}(i-1) \\ S(i-1) \end{pmatrix}. \tag{3.1}$$

[4]We follow the convention of i, j increasing downward from the top of the atmosphere, where $i = 0$, $j = 1$. Index i is used for level variables, whereas index j is used for layer variables. The N vertical layers, which are enumerated from 1 to N, are enclosed by $(N + 1)$ vertical levels, enumerated from 0 to N.

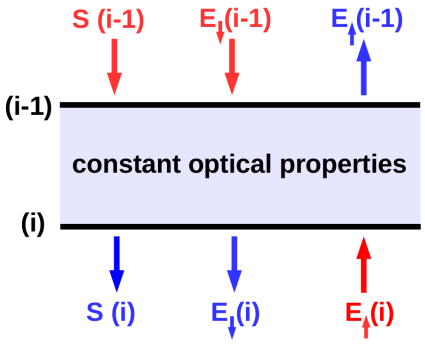

Figure 3.8: *A homogeneous model layer between levels* $(i-1)$ *and* (i)*. Incoming radiative fluxes are colored red, outgoing fluxes are colored blue.*

The linear coefficients a_{kl} in Eq. (3.1), referred to as Eddington coefficients, depend on optical properties of layer (j). They have the following physical meaning: a_{11} and a_{12} represent the transmission and reflection coefficient for diffuse radiation, respectively. Further, a_{13} and a_{23} represent the reflection and transmission coefficient for the primary scattered solar radiation, respectively, while a_{33} denotes the transmission coefficient for the direct solar radiation. For the details of their definition the reader is referred to Zdunkowski et al. (2007).

The preceding formulation considered solar radiative transfer in the absence of thermal emission. As solar and thermal spectra are separated and can be therefore conveniently treated independently, the solar source is merely replaced with the terrestrial emission term when addressing thermal radiation. The vertical temperature variation is thereby taken into account by allowing the Planck function to vary in accordance with the Eddington-type linearization:

$$B_{Planck}(\tau) = B_0 + B_1\tau, \tag{3.2}$$

where B_0 and B_1 are constants. The equation system for a single layer is constructed in a similar manner, accounting for both upward and downward thermal emission contributions. For a more comprehensive explanation the reader is further referred to Zdunkowski et al. (2007), as in the rest of this chapter we will focus on solar radiation.

In a consecutive step individual layers are concatenated by imposing flux continuity at each level. Taking appropriate boundary conditions at TOA (Eq. 3.3) and at the ground (Eq. 3.4, with A_g representing ground albedo) into account,

$$E_{\downarrow}(0) = 0, \tag{3.3}$$

$$E_{\uparrow}(N) = A_g[S(N) + E_{\downarrow}(N)], \tag{3.4}$$

the equation system is solved analytically by means of standard numerical procedures (e.g., Zdunkowski et al., 2007; Stephens and Webster, 1981; Ritter and Geleyn, 1992; Stephens et al., 2001). After radiative fluxes thrughout the atmosphere have been computed, the

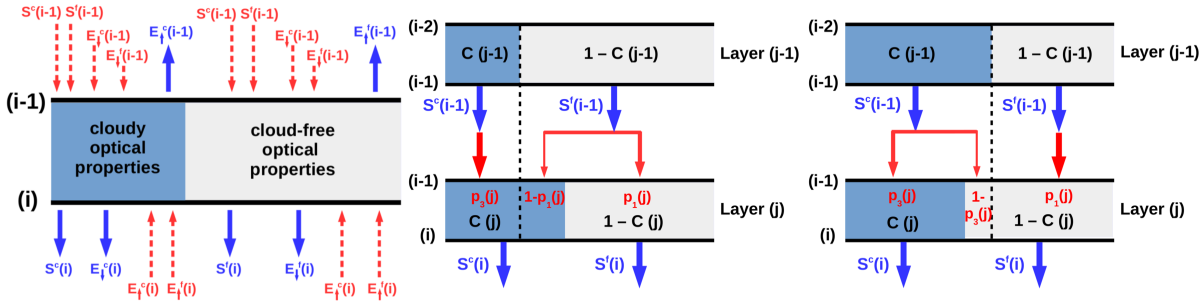

Figure 3.9: *Left panel depicts a partially cloudy model layer located between levels* $(i-1)$ *and* (i)*, which has the information about the cloudy and cloud-free optical properties. The blue arrows represent radiative fluxes emanating from cloudy and cloud-free regions. The red arrows indicate a complex situation of possible incoming fluxes, which can though be determined taking the overlap rules and knowledge about the cloud fraction in the adjacent layers into account. Middle and right panels illustrate the transmission of direct solar radiation through two adjacent layers with different cloud fraction for maximum overlap concept. Middle schematic shows the situation where the upper layer has smaller cloud fraction than the lower layer, while the right schematic shows the opposite situation.*

calculation of heating rates is straightforward. The heating rate of an individual layer is given by:

$$\frac{\Delta T}{\Delta t} = \frac{1}{\rho c_p} \frac{\Delta E_{net}}{\Delta z}, \tag{3.5}$$

where ρ represents air density, c_p represents the specific heat capacity of air at constant pressure, Δz represents the vertical thickness of the layer and ΔE_{net} represents the radiative flux absorbed in the layer, defined as the difference between the fluxes entering the layer and those leaving the layer.

Inclusion of partial cloudiness

Consider now a partially cloudy layer (Fig. 3.9, left panel), which is characterized by two sets of optical properties and corresponding Eddington coefficients – one for the cloudy region (superscript "c") and the other for the cloud-free region (superscript "f"). In order to apply the maximum-random overlap assumption (Geleyn and Hollingsworth, 1979) the cloudy and cloud-free fluxes need to be treated separately. Total radiative flux at a given level is thus the sum of the cloudy and cloud-free component, e.g.,

$$S(i) = S^c(i) + S^f(i), \tag{3.6}$$

and analogously for both diffuse components:

$$E_{\downarrow}(i) = E^c_{\downarrow}(i) + E^f_{\downarrow}(i), \tag{3.7}$$

$$E_{\uparrow}(i) = E^c_{\uparrow}(i) + E^f_{\uparrow}(i). \tag{3.8}$$

The equation system (3.1) is replaced by:

$$\begin{pmatrix} E^c_\uparrow(i-1) \\ E^c_\downarrow(i) \\ S^c(i) \end{pmatrix} = \begin{pmatrix} a^c_{11} & a^c_{12} & a^c_{13} \\ a^c_{12} & a^c_{11} & a^c_{23} \\ 0 & 0 & a^c_{33} \end{pmatrix} \cdot \begin{pmatrix} p_4 E^c_\uparrow(i) + (1-p_2) E^f_\uparrow(i) \\ p_3 E^c_\downarrow(i-1) + (1-p_1) E^f_\downarrow(i-1) \\ p_3 S^c(i-1) + (1-p_1) S^f(i-1) \end{pmatrix}, \tag{3.9}$$

$$\begin{pmatrix} E^f_\uparrow(i-1) \\ E^f_\downarrow(i) \\ S^f(i) \end{pmatrix} = \begin{pmatrix} a^f_{11} & a^f_{12} & a^f_{13} \\ a^f_{12} & a^f_{11} & a^f_{23} \\ 0 & 0 & a^f_{33} \end{pmatrix} \cdot \begin{pmatrix} (1-p_4) E^c_\uparrow(i) + p_2 E^f_\uparrow(i) \\ (1-p_3) E^c_\downarrow(i-1) + p_1 E^f_\downarrow(i-1) \\ (1-p_3) S^c(i-1) + p_1 S^f(i-1) \end{pmatrix}, \tag{3.10}$$

so that the fluxes emanating from the cloudy and cloud-free region depend on a linear combination of both cloudy and cloud-free incoming fluxes. Overlap coefficients p_1, p_2, p_3 and p_4 refer to layer (j) and describe the division of incoming fluxes between the cloudy and cloud-free region in accordance with the maximum-random overlap assumption, where adjacent cloudy layers are overlapped maximally, and cloudy layers separated by at least one cloud-free layer are overlapped randomly. For layer (j) they have the following form:

$$p_1(j) = \frac{1 - \max\big\{C(j), C(j-1)\big\}}{1 - C(j-1)}, \tag{3.11}$$

$$p_2(j) = \frac{1 - \max\big\{C(j), C(j+1)\big\}}{1 - C(j+1)}, \tag{3.12}$$

$$p_3(j) = \frac{\min\big\{C(j), C(j-1)\big\}}{C(j-1)}, \tag{3.13}$$

$$p_4(j) = \frac{\min\big\{C(j), C(j+1)\big\}}{C(j+1)}, \tag{3.14}$$

with C representing layer cloud fraction. Figure 3.9 (middle and right panels) illustrates both possible geometries that need to be considered in order to determine the coefficients p_1 and p_3 related to the division of downward fluxes (the division of upward fluxes is managed via p_2 and p_4 in a similar fashion). For a two-region layer, the boundary condition at TOA (Eq. 3.3) is formulated as:

$$E^c_\downarrow(0) = 0, \tag{3.15}$$

$$E^f_\downarrow(0) = 0. \tag{3.16}$$

Similarly, the boundary condition at the ground (Eq. 3.4) is extended to:

$$E^c_\uparrow(N) = A_g[S^c(N) + E^c_\downarrow(N)], \tag{3.17}$$

$$E^f_\uparrow(N) = A_g[S^f(N) + E^f_\downarrow(N)], \tag{3.18}$$

which assumes that the downward fluxes after they have been reflected from the ground enter the same sections of cloudy and cloud-free air (isotropic ground reflection). The method has been successfully implemented in the radiative transfer package *libRadtran* for the purpose of this study.

3.2.3 The Tripleclouds radiative solver

The underlying two-stream framework employed in the present Tripleclouds implementation differs from that applied by SH08 and subsequent studies (e.g., Shonk et al., 2010; Hogan et al., 2019), whereby the latter is based on the adding method (Lacis and Hansen, 1974) as originally included in the Edwards and Slingo (1996) radiation scheme. We thus commence by extending the previously introduced δ-Eddington two-stream methodology (Joseph et al., 1976; Zdunkowski et al., 2007) to three regions at each height, whereas subsequently the novel overlap formulation based on the core-shell model is established.

δ-Eddington two-stream method for three regions at each height

Consider now a model layer located between levels $(i-1)$ and (i) divided into three regions (Fig. 3.10). Such layer is characterized by three sets of optical properties and corresponding Eddington coefficients: one for the region of optically thick cloud (superscript "*ck*"), the other for the region of optically thin cloud (superscript "*cn*") and the third for the cloud-free region (superscript "*f*"). In order to apply vertical overlap rules the radiative fluxes corresponding to each of the three regions need to be defined separately at each level (e.g., S^{ck}, S^{cn} and S^{f}; and analogously for both diffuse components). Total radiative flux at level (i) is thus the sum of both cloudy and the cloud-free components:

$$S(i) = S^{ck}(i) + S^{cn}(i) + S^{f}(i), \tag{3.19}$$

$$E_{\downarrow}(i) = E^{ck}_{\downarrow}(i) + E^{cn}_{\downarrow}(i) + E^{f}_{\downarrow}(i), \tag{3.20}$$

$$E_{\uparrow}(i) = E^{ck}_{\uparrow}(i) + E^{cn}_{\uparrow}(i) + E^{f}_{\uparrow}(i). \tag{3.21}$$

The equation system (3.1) is replaced by:

$$\begin{pmatrix} E^{ck}_{\uparrow}(i-1) \\ E^{ck}_{\downarrow}(i) \\ S^{ck}(i) \end{pmatrix} = \begin{pmatrix} a^{ck}_{11} & a^{ck}_{12} & a^{ck}_{13} \\ a^{ck}_{12} & a^{ck}_{11} & a^{ck}_{23} \\ 0 & 0 & a^{ck}_{33} \end{pmatrix} \cdot \begin{pmatrix} T^{ck,ck}_{\uparrow} E^{ck}_{\uparrow}(i) + T^{cn,ck}_{\uparrow} E^{cn}_{\uparrow}(i) + T^{f,ck}_{\uparrow} E^{f}_{\uparrow}(i) \\ T^{ck,ck}_{\downarrow} E^{ck}_{\downarrow}(i-1) + T^{cn,ck}_{\downarrow} E^{cn}_{\downarrow}(i-1) + T^{f,ck}_{\downarrow} E^{f}_{\downarrow}(i-1) \\ T^{ck,ck}_{\downarrow} S^{ck}(i-1) + T^{cn,ck}_{\downarrow} S^{cn}(i-1) + T^{f,ck}_{\downarrow} S^{f}(i-1) \end{pmatrix}, \tag{3.22}$$

$$\begin{pmatrix} E^{cn}_{\uparrow}(i-1) \\ E^{cn}_{\downarrow}(i) \\ S^{cn}(i) \end{pmatrix} = \begin{pmatrix} a^{cn}_{11} & a^{cn}_{12} & a^{cn}_{13} \\ a^{cn}_{12} & a^{cn}_{11} & a^{cn}_{23} \\ 0 & 0 & a^{cn}_{33} \end{pmatrix} \cdot \begin{pmatrix} T^{ck,cn}_{\uparrow} E^{ck}_{\uparrow}(i) + T^{cn,cn}_{\uparrow} E^{cn}_{\uparrow}(i) + T^{f,cn}_{\uparrow} E^{f}_{\uparrow}(i) \\ T^{ck,cn}_{\downarrow} E^{ck}_{\downarrow}(i-1) + T^{cn,cn}_{\downarrow} E^{cn}_{\downarrow}(i-1) + T^{f,cn}_{\downarrow} E^{f}_{\downarrow}(i-1) \\ T^{ck,cn}_{\downarrow} S^{ck}(i-1) + T^{cn,cn}_{\downarrow} S^{cn}(i-1) + T^{f,cn}_{\downarrow} S^{f}(i-1) \end{pmatrix}, \tag{3.23}$$

$$\begin{pmatrix} E^{f}_{\uparrow}(i-1) \\ E^{f}_{\downarrow}(i) \\ S^{f}(i) \end{pmatrix} = \begin{pmatrix} a^{f}_{11} & a^{f}_{12} & a^{f}_{13} \\ a^{f}_{12} & a^{f}_{11} & a^{f}_{23} \\ 0 & 0 & a^{f}_{33} \end{pmatrix} \cdot \begin{pmatrix} T^{ck,f}_{\uparrow} E^{ck}_{\uparrow}(i) + T^{cn,f}_{\uparrow} E^{cn}_{\uparrow}(i) + T^{f,f}_{\uparrow} E^{f}_{\uparrow}(i) \\ T^{ck,f}_{\downarrow} E^{ck}_{\downarrow}(i-1) + T^{cn,f}_{\downarrow} E^{cn}_{\downarrow}(i-1) + T^{f,f}_{\downarrow} E^{f}_{\downarrow}(i-1) \\ T^{ck,f}_{\downarrow} S^{ck}(i-1) + T^{cn,f}_{\downarrow} S^{cn}(i-1) + T^{f,f}_{\downarrow} S^{f}(i-1) \end{pmatrix}, \tag{3.24}$$

Figure 3.10: *A model layer between levels* $(i-1)$ *and* (i) *divided into three regions.*

so that the fluxes emanating from a certain region of the layer under consideration (e.g., region of optically thick cloud) generally depend on a linear combination of the incoming fluxes stemming from each of the three regions in adjacent layers. The coefficients starting with T appearing in Eqs. (3.22), (3.23), (3.24) are referred to as the overlap (transfer) coefficients and correspond to the layer under consideration (j). The coefficient $T_{\downarrow}^{ck,cn}(j)$, for example, represents the fraction of downward radiation that leaves the base of optically thick cloud of layer $(j-1)$ and enters the optically thin cloud of layer under consideration (j). The overlap coefficients quantitatively depend on the choice of the overlap rule, which will be discussed in the next paragraph. For a three-region layer, the boundary condition at TOA (Eq. 3.3) implies:

$$E_{\downarrow}^{ck}(0) = 0, \tag{3.25}$$

$$E_{\downarrow}^{cn}(0) = 0, \tag{3.26}$$

$$E_{\downarrow}^{f}(0) = 0. \tag{3.27}$$

The boundary condition at the ground (Eq. 3.4) is extended to:

$$E_{\uparrow}^{ck}(N) = A_g[S^{ck}(N) + E_{\downarrow}^{ck}(N)], \tag{3.28}$$

$$E_{\uparrow}^{cn}(N) = A_g[S^{cn}(N) + E_{\downarrow}^{cn}(N)], \tag{3.29}$$

$$E_{\uparrow}^{f}(N) = A_g[S^{f}(N) + E_{\downarrow}^{f}(N)], \tag{3.30}$$

which assumes that the downward fluxes leaving the lowest model layer, after reflection enter the same sections of individual cloudy and cloud-free air.

Overlap considerations

The layer cloud fraction C is given by:

$$C(j) = C^{ck}(j) + C^{cn}(j). \tag{3.31}$$

In our implementation, we demand the following relationship between the individual cloud fraction components:

$$C^{ck}(j) = \alpha \cdot C(j), \tag{3.32}$$

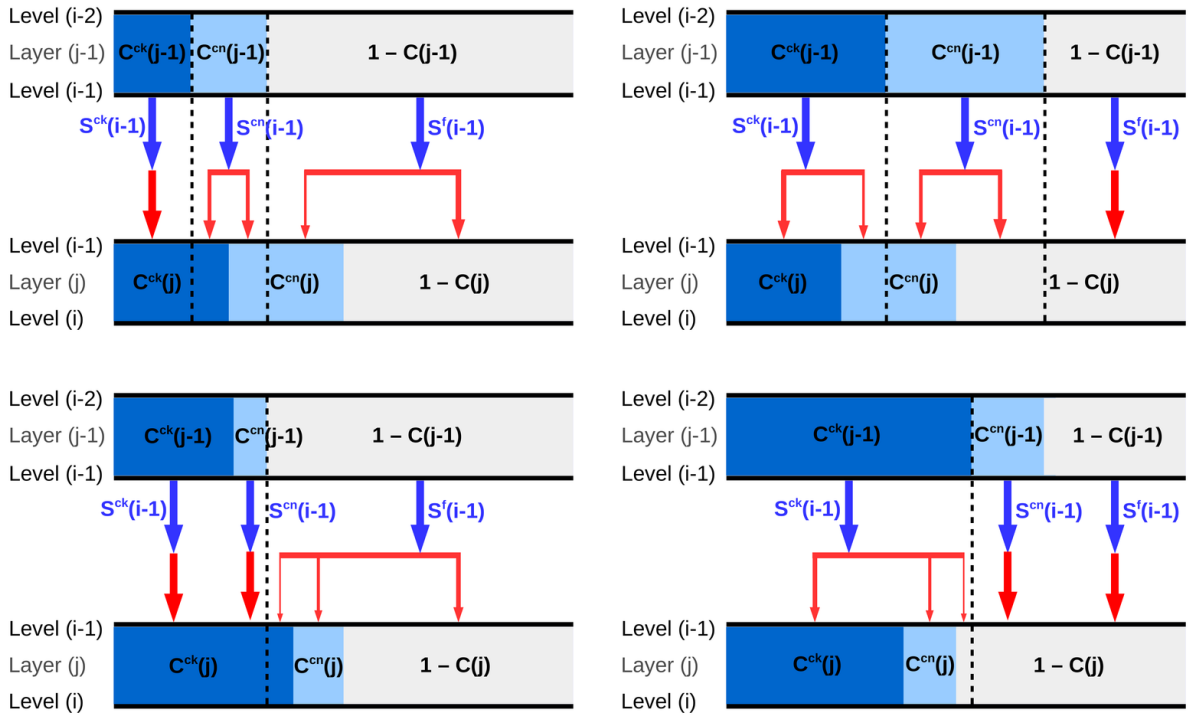

Figure 3.11: *Transmission of direct solar radiation through two adjacent layers with partial cloudiness for the maximum^2-random overlap concept.*

$$C^{cn}(j) = (1 - \alpha) \cdot C(j), \tag{3.33}$$

where α is a constant between 0 and 1. We apply the maximum-random overlap assumption (Geleyn and Hollingsworth, 1979) for the entire layer cloudiness (sum of optically thick and thin cloudy regions), where adjacent cloudy layers exhibit maximal overlap and cloudy layers separated by at least one cloud-free layer exhibit random overlap. If the cloudy layers are split into two parts, however, this overlap rule is not sufficient and needs to be extended. Therefore, we additionally assume the maximum overlap of optically thicker cloudy regions in pairs of adjacent layers and abbreviate this extended overlap rule to the "maximum^2-random overlap". This assumption implicitly places the optically thicker cloudy region towards the interior of the cloud in the horizontal plane, which is in line with the core-shell model.

Now one can quantitatively determine the overlap coefficients in Eqs. (3.22), (3.23) and (3.24) for the maximum^2-random overlap. We consider the transmission of downward radiation through two adjacent layers with partial cloudiness. Four possible geometries, illustrated in Fig. 3.11, need to be treated. For the situation depicted on the top left panel of Fig. 3.11, the transmission of direct radiation can be formulated as follows. The optically thick cloud of layer $(j-1)$ transmits $S^{ck}(i-1)$, the optically thin cloud transmits $S^{cn}(i-1)$

and the cloud-free region transmits $S^f(i-1)$. These three components of the transmitted radiation must then be distributed between the three regions of the lower layer (j). The maximum overlap of optically thick cloudy regions implies that the entire radiation S^{ck} leaving the base of layer $(j-1)$ enters the optically thick cloud below:

$$T_{\downarrow}^{ck,ck}(j) = 1, \tag{3.34}$$

and none of it enters the other two regions:

$$T_{\downarrow}^{ck,cn}(j) = 0, \tag{3.35}$$

$$T_{\downarrow}^{ck,f}(j) = 0. \tag{3.36}$$

To ensure the maximum overlap of cloudy layers as a whole, the remaining cloudy flux at the base of layer $(j-1)$, namely the $S^{cn}(i-1)$, needs to be led into the two cloudy regions of the lower layer, with the priority to enter the optically thick cloud. This yields:

$$T_{\downarrow}^{cn,ck}(j) = \frac{C^{ck}(j) - C^{ck}(j-1)}{C^{cn}(j-1)}, \tag{3.37}$$

$$T_{\downarrow}^{cn,cn}(j) = \frac{[C^{ck}(j-1) - C^{cn}(j-1)] - C^{ck}(j)}{C^{cn}(j-1)}, \tag{3.38}$$

$$T_{\downarrow}^{cn,f}(j) = 0. \tag{3.39}$$

The cloud-free flux S^f at the base of layer $(j-1)$ is distributed according to:

$$T_{\downarrow}^{f,ck}(j) = 0, \tag{3.40}$$

$$T_{\downarrow}^{f,cn}(j) = \frac{C(j) - C(j-1)}{1 - C(j-1)}, \tag{3.41}$$

$$T_{\downarrow}^{f,f}(j) = \frac{1 - C(j)}{1 - C(j-1)}. \tag{3.42}$$

The derivation of overlap coefficients for other three geometric arrangements involves analogous considerations, whereby the resulting formulas are given in Table 3.1. In order to simplify the handling of various overlap geometries it is convenient to implement the operator G:

$$G(x) = \begin{cases} 1, & \text{if } x > 0 \\ 0, & \text{if } x \leq 0 \end{cases}$$

Hence the generalized overlap coefficients can be formulated as exposed in the rightmost column of Table 3.1, taking into account that:

$$\sum_{b=\{ck,cn,f\}} T_{\downarrow}^{ck,b}(j) = 1, \tag{3.43}$$

Table 3.1: *The transfer coefficients $T_{\downarrow}^{a,b}(j)$ for the four cloud geometries depicted in Fig. 3.11, denoted as case "1-A" (top left panel), "1-B" (bottom left panel), "2-A" (top right panel) and "2-B" (bottom right panel), as well as their general form (layer index written as a subscript).*

	Case 1 $C_j > C_{j-1}$		Case 2 $C_j \leq C_{j-1}$		General formulation
	A $C_j^{ck} < C_{j-1}$	B $C_j^{ck} \geq C_{j-1}$	A $C_j > C_{j-1}^{ck}$	B $C_j \leq C_{j-1}^{ck}$	
$T_{\downarrow,j}^{ck,ck}$	1	1	$\frac{C_j^{ck}}{C_{j-1}^{ck}}$	$\frac{C_j^{ck}}{C_{j-1}^{ck}}$	$\frac{\min\{C_j^{ck}, C_{j-1}^{ck}\}}{C_{j-1}^{ck}}$
$T_{\downarrow,j}^{ck,cn}$	0	0	$1 - \frac{C_j^{ck}}{C_{j-1}^{ck}}$	$\frac{C_j^{cn}}{C_{j-1}^{ck}}$	$1 - T_{\downarrow,j}^{ck,ck} - T_{\downarrow,j}^{ck,f}$
$T_{\downarrow,j}^{ck,f}$	0	0	0	$1 - \frac{C_j}{C_{j-1}^{ck}}$	$G(C_{j-1} - C_j) G(C_{j-1}^{ck} - C_j)(1 - \frac{C_j}{C_{j-1}^{ck}})$
$T_{\downarrow,j}^{cn,ck}$	$\frac{C_j^{ck} - C_{j-1}^{ck}}{C_{j-1}^{cn}}$	1	0	0	$G(C_j - C_{j-1})(1 - \frac{\max\{C_j^{ck}, C_{j-1}\} - C_j^{ck}}{C_{j-1}^{cn}})$
$T_{\downarrow,j}^{cn,cn}$	$\frac{C_{j-1} - C_j^{ck}}{C_{j-1}^{cn}}$	0	$\frac{C_j - C_{j-1}^{ck}}{C_{j-1}^{cn}}$	0	$1 - T_{\downarrow,j}^{cn,ck} - T_{\downarrow,j}^{cn,f}$
$T_{\downarrow,j}^{cn,f}$	0	0	$\frac{C_{j-1} - C_j}{C_{j-1}^{cn}}$	1	$G(C_{j-1} - C_j)(1 - \frac{C_j - \min\{C_j, C_{j-1}^{ck}\}}{C_{j-1}^{cn}})$
$T_{\downarrow,j}^{f,ck}$	0	$\frac{C_j^{ck} - C_{j-1}}{1 - C_{j-1}}$	0	0	$G(C_j - C_{j-1}) G(C_j^{ck} - C_{j-1})(\frac{C_j^{ck} - C_{j-1}}{1 - C_{j-1}})$
$T_{\downarrow,j}^{f,cn}$	$\frac{C_j - C_{j-1}}{1 - C_{j-1}}$	$\frac{C_j^{cn}}{1 - C_{j-1}}$	0	0	$1 - T_{\downarrow,j}^{f,ck} - T_{\downarrow,j}^{f,f}$
$T_{\downarrow,j}^{f,f}$	$\frac{1 - C_j}{1 - C_{j-1}}$	$\frac{1 - C_j}{1 - C_{j-1}}$	1	1	$\frac{1 - \max\{C_j, C_{j-1}\}}{1 - C_{j-1}}$

$$\sum_{b=\{ck,cn,f\}} T_{\downarrow}^{cn,b}(j) = 1, \tag{3.44}$$

$$\sum_{b=\{ck,cn,f\}} T_{\downarrow}^{f,b}(j) = 1. \tag{3.45}$$

The transmission of upward radiation is managed via overlap coefficients $T_{\uparrow}^{a,b}(j)$ in an equivalent manner, except that these are dependent on the cloud fraction in the layer under consideration and that in the layer underneath $[C(j), C(j+1)]$. It should be noted that the same coefficients govern the reflection, whereby the upward reflection of downward radiation is treated with $T_{\downarrow}^{a,b}$ and the reverse situation is treated with $T_{\uparrow}^{a,b}$. Pairwise overlap as employed here ensures that the matrix problem is fast to solve. Whereas a drawback of the core-shell model and thereby the outlined overlap is that it underperforms in the case of vertically developed cloud systems in strongly sheared conditions, the present Tripleclouds implementation is an excellent tool to study shallow convective cloudiness as well as vertically upright storm clouds. In this way the effects of cloud horizontal inhomogeneity are tackled in isolation, while the issues related to vertical shear are eliminated. The Tripleclouds radiative solver has been successfully implemented in *libRadtran*. Technically, the calculation of the overlap coefficients is performed in an autonomous function enabling flexible modifications of overlap rules in the future.

3.3 Configuring baseline Tripleclouds experiments

In order to utilize the Tripleclouds radiative solver, a pair of LWC/IWC characterizing the two cloudy regions has to be generated in each vertical layer. In the following we describe the configuration of the baseline Tripleclouds experiments carried out in this work. For the sake of brevity we refer solely to the liquid phase in the remainder of this section, since analogous considerations are applied to the ice phase.

As introduced in the previous chapter, SH08 showed that TC performs well for TOA radiative fluxes when the LWC^{cn} is chosen to be the value corresponding to the 16th percentile of the observed LWC distribution, whereas the LWC^{ck} is determined under conservation constraints of layer mean. This method, evaluated based on the analysis of high-resolution cloud radar data, was referred to as the "lower percentile (LP) method" and utilizes a split percentile of 50, implying that cloudiness in each vertical layer is divided through a median of distribution into two equal parts.

When the TC radiative solver resides in a host GCM model, however, the details about the underlying LWC variability are not known, therefore several assumptions have to be introduced. In order to obtain the pair (LWC^{cn}, LWC^{ck}) from $\overline{LWC}$, which is indeed available in a GCM, we introduce the so-called $\overline{LWC}$-scaling factors for the optically thin and thick cloudy region, termed s^{cn} and s^{ck} respectively, fulfilling the following relationships:

$$LWC^{cn} = \overline{LWC}s^{cn}, \tag{3.46}$$

$$LWC^{ck} = \overline{LWC}s^{ck}. \tag{3.47}$$

Different parameters to define the degree of cloud horizontal inhomogeneity are employed in the existing literature and numerical models (e.g., Cahalan et al., 1994a; Smith and Del Genio, 2001; Carlin et al., 2002; Rossow et al., 2002; Oreopoulos and Cahalan, 2005). A frequently used parameter is the previously mentioned fractional standard deviation (FSD) of LWC, which is simply the standard deviation (σ_{LWC}) divided by the mean ($\overline{LWC}$). The FSD is a convenient measure, since it accounts for a strong correlation between $\overline{LWC}$ and σ_{LWC} (Smith and Del Genio, 2001; Carlin et al., 2002; Hill et al., 2012). Based on a comprehensive review of numerous observational studies encompassing diverse cloud data sets, Shonk et al., 2010 converted various variability measures into a single globally applicable FSD parameter, whose mean value and uncertainty are as follows:

$$FSD = 0.75 \pm 0.18. \tag{3.48}$$

When TC is employed in a host GCM, moreover, an assumption about the shape of LWC distribution has to be made. To this end, we test three different assumptions for subgrid cloud condensate distribution: Gaussian distribution, which traditionally prevailed in many models due to its simplicity, as well as more realistic gamma (supported by Barker et al., 1996; Pincus et al., 1999; Carlin et al., 2002; Rossow et al., 2002) and

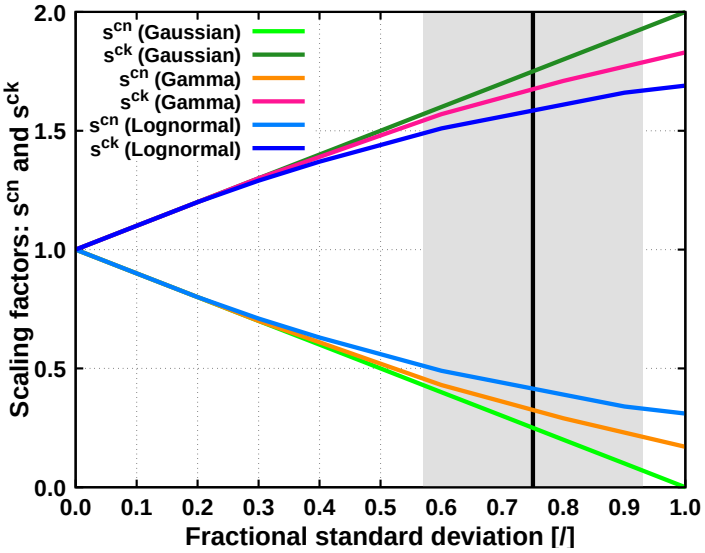

Figure 3.12: *Scaling factors (s^{cn}, s^{ck}) of $\overline{LWC}$ for Gaussian, gamma and lognormal distributions. The black line and the grey area represent mean global FSD and its uncertainty.*

lognormal distribution (supported by Pincus et al., 1999; Hogan and Illingworth, 2003). For a Gaussian distribution, the 16th percentile (advocated by SH08) is given by:

$$s^{cn} = 1 - FSD, \tag{3.49}$$

although caution needs to be taken as this expression becomes unphysical for FSD > 1. Similarly, according to Hogan et al. (2019), for a gamma distribution the 16th percentile is approximated by:

$$s^{cn} = \exp\left[- FSD - \frac{FSD^2}{2} - \frac{FSD^3}{4} \right]. \tag{3.50}$$

Finally, according to Hogan et al. (2016), for a lognormal distribution:

$$s^{cn} = \frac{1}{\sqrt{FSD^2 + 1}} \exp\left[- \sqrt{\ln(FSD^2 + 1)} \right]. \tag{3.51}$$

For any FSD value, the s^{cn} defined with Eq. (3.50) or (3.51) lies in the range between 0 and 1. The desired conservation of $\overline{LWC}$ implies $s^{ck} = 2 - s^{cn}$, where the layer cloudiness is geometrically halved. The approach outlined above, utilizing any of the selected distributional assumptions to generate the LWC pair, is referred to as the "FSD method" in the remainder of this work. The resulting $\overline{LWC}$-scaling factors for Gaussian, gamma and lognormal distribution as a function of FSD are shown in Fig. 3.12. It is immediately apparent that in the region of the global FSD estimate, the pair (LWC^{cn}, LWC^{ck}) generally exhibits large sensitivity to the assumed form of LWC distribution. This signifies the meaningfulness to pose a question, whether different assumptions for the subgrid cloud condensate distribution significantly affect radiative quantities when global FSD is applied as a proxy for cloud internal variability.

3.4 Experimental design

The experimental strategy to quantify radiative biases in regional models for shallow cumulus clouds is presented first. In the subsequent section the design of radiation experiments at global scale targeted primarily at exploring the potential of the Tripleclouds method for diverse cloud types is outlined. Radiative diagnostics and bias measures are introduced thereafter. In the final section the radiative transfer simulation setup is summarized.

3.4.1 Regional-scale modeling strategy

Table 3.2 lists the experiments performed to quantify radiative biases for evolving shallow cumulus cloud field at the scale of regional models. On the whole, these experiments aim at assessing the overall bias of radiative quantities in current regional NWP and climate models, which typically employ two-stream radiation schemes operating on horizontally homogeneous fractional cloudiness. The another objective is to additionally examine the bias portion stemming from neglected grid-scale and subgrid-scale horizontal photon transport.

Thus, to quantify the bias of radiative quantities in regional models, a regional model-type experiment together with a benchmark is required. The benchmark calculation using the 3-D model MYSTIC was performed on a high-resolution LES cloud field grid, whereby the result was horizontally averaged over the domain (abbreviated as the "3-D" experiment). In order to imitate poor representation of shallow cumulus in regional models, the information content of the cloud field has to be reduced. Therefore the domain was horizontally splitted into four boxes (Fig. 3.13) with dimensions comparable to regional-scale model grid spacing (3.2 km) and cloud radiative properties (LWC, R_e) were horizontally averaged within these boxes in each vertical layer. In this way, four columns which generally contain homogeneous partial cloudiness were created and the δ-Eddington two-stream method with maximum-random overlap assumption was called four times per cloud scene, whereby the resulting radiative quantities were again horizontally averaged over the domain (abbreviated as the "1-D" experiment). Moreover, it should be noted that the cloud field resolution in the 1-D experiment was only degraded in the horizontal plane, whereas the vertical resolution was retained as inherited from the LES grid[5]. In summary, the 1-D experiment has multiple error sources, namely, the poor cloud structure as well as the neglected grid-scale and subgrid-scale horizontal photon transport. Furthermore, we created a third, intermediate experiment by running MYSTIC in independent column mode on cloud field preserving its LES resolution and averaging the result horizontally (abbreviated as the "ICA" experiment). The ICA is thus the same as the 3-D experiment except that it neglects horizontal photon transport between the LES-grid columns. In this way one is able to isolate and quantify the contribution of neglected horizontal photon transport to the overall error of 1-D experiments (in the hypothetical case when the subgrid cloud structure

[5]This can be partially justified by the fact that weather models have relatively fine vertical grid spacing in the planetary boundary layer, although we agree that proper handling of variable vertical resolution would deserve further attention.

Table 3.2: *List of regional-scale radiative transfer experiments.*

Experiment description	Abbreviation
Benchmark 3-D Monte Carlo radiative model	3-D
ICA Monte Carlo radiative model	ICA
Regional model radiation scheme	1-D

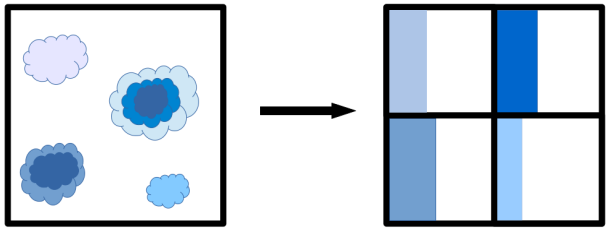

Figure 3.13: *Left panel: horizontal cross-section of LES shallow cumulus cloud field. Right panel: division of this layer into four boxes with dimensions comparable to regional model grid spacing, each containing a horizontally homogeneous fractional cloud. The latter is constructed by averaging LES distributions of cloud radiative properties over the cloudy fraction of each box.*

would be perfectly guessed). The outcome of the regional-scale radiation experiments will be thoroughly discussed in the first part of the results chapter (Section 4.1).

3.4.2 Global-scale modeling strategy

Table 3.3 summarizes the baseline experiments carried out at the scale of global models for four selected cloud field case studies. These experiments aim to explore the potential of the state-of-the-art Tripleclouds method for use in coarse-resolution weather and climate models in the first place, compare its performance with the conventional GCM cloud modeling approach and additionally quantify the bias related to neglected horizontal photon transport at the scale of GCMs.

The benchmark 3-D MYSTIC and associated ICA experiment were configured in the same manner as outlined above. Thus they were both performed on the high-resolution cloud field grid (Fig. 3.14, left), whereby the result was horizontally averaged across the domain. The difference between the ICA and 3-D was used to assess the impact of horizontal photon transport on domain-averaged (GCM-scale) radiative quantities. Moreover, we performed a conventional GCM-type calculation on a layer-averaged fractional cloud (Fig. 3.14, middle). The δ-Eddington two-stream method with maximum-random overlap was used hereby in place of conventional GCM scheme. The Tripleclouds radiative solver was employed in conjunction with both the LP and FSD method (Fig. 3.14, right). In order to verify (or discard) the validity of the global FSD estimate for atmospheric heating

Table 3.3: *List of global-scale radiative transfer experiments.*

Experiment description	Abbreviation
Benchmark 3-D Monte Carlo radiative model	3-D
ICA Monte Carlo radiative model	ICA
Conventional GCM radiation scheme	GCM
Tripleclouds radiative solver with LP method	TC(LP)
Tripleclouds radiative solver with FSD method	TC(FSD)

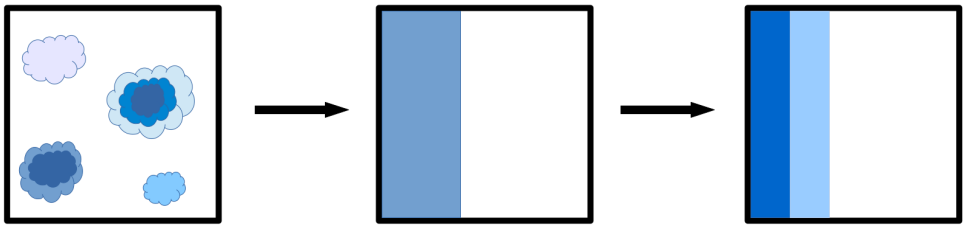

Figure 3.14: *Left panel: high-resolution cloud field prescribed on a domain with dimensions comparable to global weather or climate model grid box (shown is a horizontal cross-section). Middle panel: conditions in a grid box of a conventional GCM (homogeneous fractional cloudiness). Right panel: two-region cloudy layer used as input for the Tripleclouds radiative solver.*

rates and surface fluxes, we applied its mean value (0.75) in the initial TC experiments together with all three assumptions for subgrid cloud condensate distribution (Gaussian, gamma and lognormal) as outlined in Section 3.3. The resulting LWC profiles for the cumulus cloud field case study are shown in Fig. 3.15, demonstrating that the LWC pair characterizing the two cloudy regions is clearly sensitive to the distribution assumption, when the mean global FSD estimate is used as a proxy for cloud horizontal inhomogeneity degree. It should be noted that the effective radii characterizing the two cloudy regions were kept the same (averaged R_e). The outcome of the global-scale radiation experiments will be comprehensively discussed in the second part of the results chapter (Section 4.2).

3.4.3 Diagnostics and bias measures

For each radiative experiment we diagnosed atmospheric heating rate and net surface flux. Each diagnostic was examined in the solar, thermal (nighttime effect) and total (daytime effect) spectral range. The error is measured by the absolute bias (Eq. 3.52), relative bias (Eq. 3.53) and for the heating rate profile additionally by the root mean square error evaluated throughout the vertical extent of the cloud layer (Eq. 3.54):

$$\text{absolute bias} = y - x, \tag{3.52}$$

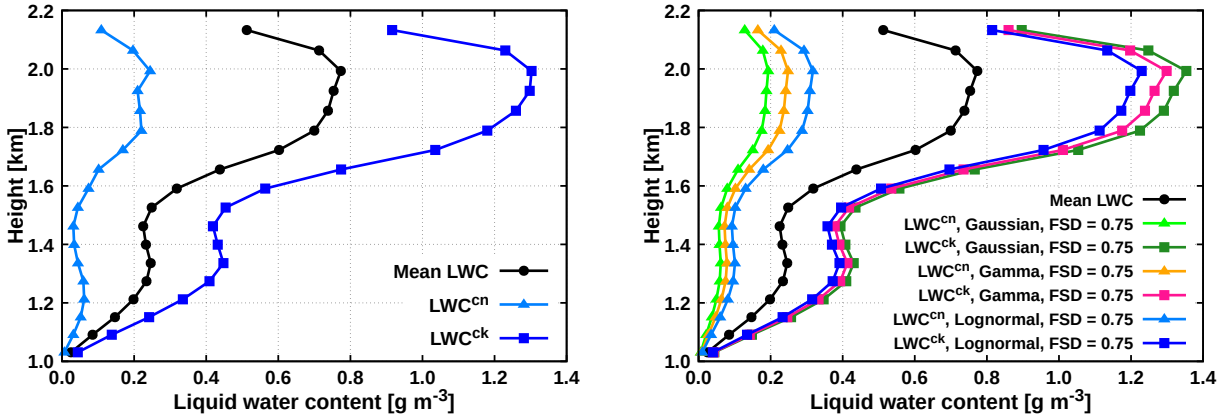

Figure 3.15: *LWC profiles obtained with the LP method (left panel) and the FSD method using mean global estimate and altering LWC distribution (right panel) for the cumulus case study.*

$$\text{relative bias} = \left(\frac{y}{x} - 1\right) \cdot 100\%, \tag{3.53}$$

$$\text{cloud-layer RMSE} = \sqrt{\overline{(y-x)^2}}, \tag{3.54}$$

where x represents the 3-D benchmark and y represents the biased quantity (i.e, the outcome of either the ICA, 1-D, GCM or any Tripleclouds experiment).

3.4.4 Radiative transfer simulation setup

In the following the basic radiative transfer simulation setup is outlined. Each radiation experiment was repeated for each cloud scene in both the solar and thermal spectral range. The background state of atmospheric pressure, temperature, density and trace gases (water vapour, O_3, CO_2) was assumed to be horizontally homogeneous, taken from the US standard atmosphere (Anderson et al., 1986). The simulation domain extended vertically up to a height of 120 km, which is considered to be the TOA. In the lowest portion of the domain where clouds are located we preserved the original high-resolution vertical grid as inherited from the parent cloud model and interpolated the background standard atmospheric conditions onto this grid. It should be reminded that solely LWC and IWC as well as the corresponding effective radii were used as input for radiation calculations to define the cloud fields, while other hydrometeor categories (i.e., precipitation-sized particles, such as rain, snow and graupel) were excluded from the analysis. Optical properties of water droplets (assumed to be spherical) were prescribed following the parameterization of Hu and Stamnes (1993), which uses the Henyey-Greenstein phase function as an approximation of the real Mie phase function. Similarly, optical properties of ice crystals were specified based on the parameterization of Yang et al. (2000), assuming habit of hexagonal columns. Parameterization of atmospheric absorption and scattering properties in the solar spectral

range follows the correlated-k distribution of Kato et al. (1999) with 32 bands. Parameterization of molecular thermal absorption was adopted from Fu and Liou (1992) utilizing 12 bands. In the Monte Carlo experiments, the forward model was used in the solar part of the spectrum and the backward technique (Klinger and Mayer, 2014) in the thermal part. The horizontal extent of the domain matched the horizontal domain size of each individual cloud field. Periodic lateral boundary conditions were applied in the 3-D configuration. Whereas the exact number of traced photons depends on the particular cloud scene, it was held sufficiently high, so that the Monte Carlo noise of domain-averaged quantities was kept below 0.1 %.

Solar downward flux at TOA corresponds to 1365, 1182 and 683 W m^{-2} at SZAs of 0° (overhead Sun), 30° and 60°, which are the principal Sun elevations examined in the present work. At the surface, a constant temperature of 288.2 K implies thermal upward flux of 389.5 W m^{-2} according to the Stefan-Boltzmann law. In order to carry out a detailed sensitivity study for regional-scale radiation calculations, SZA was varied from 0° to 80° with a step of 10°, while solar azimuth angle was held fixed at 0° (Sun illuminating the cloud scenes from the south). Further, we varied surface shortwave albedo by applying constant values of 0.25 and 0.05 as typical high and low values representing land and ocean. In the thermal part of the spectrum the surface was assumed to be nonreflective. The simulation setup of the experiments at global scale is the same as that at regional scale, except that we focused on SZA variation between 0°, 30° and 60° and the surface was assumed to have a constant solar albedo of 0.25.

Chapter 4

Results and discussion

4.1 Quantifying the radiative bias in regional models for shallow cumulus clouds

The radiative biases at the scale of regional models for the evolving shallow cumulus cloud field are assessed in the following. First, in Sections 4.1.1 and 4.1.2, we present the results for atmospheric heating rates and surface fluxes as a function of SZA for a single shallow cumulus scene with intermediate cloud cover of 52.3 % placed over land. In the subsequent Sections 4.1.3, 4.1.4 and 4.1.5 additionally the dependence on surface albedo, cloud cover and liquid water path is discussed.

4.1.1 Heating rate in the cloud layer

The vertical profile of radiative heating rate influences atmospheric stratification and directly impacts flow dynamics. Figure 4.1 shows the vertical profile of radiative heating rate in the trio (3-D, 1-D, ICA) of experiments in the solar spectral range for SZAs of 0°, 30° and 60° as well as in the thermal spectral range. In order to highlight the effects of clouds on radiative biases we examine only the profiles within the cumulus cloud layer, which is located between 1.025 and 1.875 km height (the cloud-free atmosphere below and above these heights is not shown). In the solar 3-D experiment for overhead Sun (top left panel of Fig. 4.1) there is strong absorption of solar radiation in the cloud layer, resulting in a peak heating rate of about 9 K day^{-1} reached at approximately 1.5 km height. This is slightly above the height of maximum cloud fraction (1.4 km) due to the fact that cloud liquid water, which is the dominant absorber of solar radiation in this layer, generally increases with height from cloud base towards cloud top (except in the uppermost region of the cloud, where it decreases with height due to entrainment). The maximum heating rate is thus located between the height of maximum cloud fraction and the height of maximum LWC. As the Sun descends, the incoming radiation at TOA decreases with the cosine of SZA and so does the solar heating rate in the cloud layer, reaching a maximum value of about 8 K day^{-1} at SZA of 30° and about 5 K day^{-1} at SZA of 60° in the 3-D experiments.

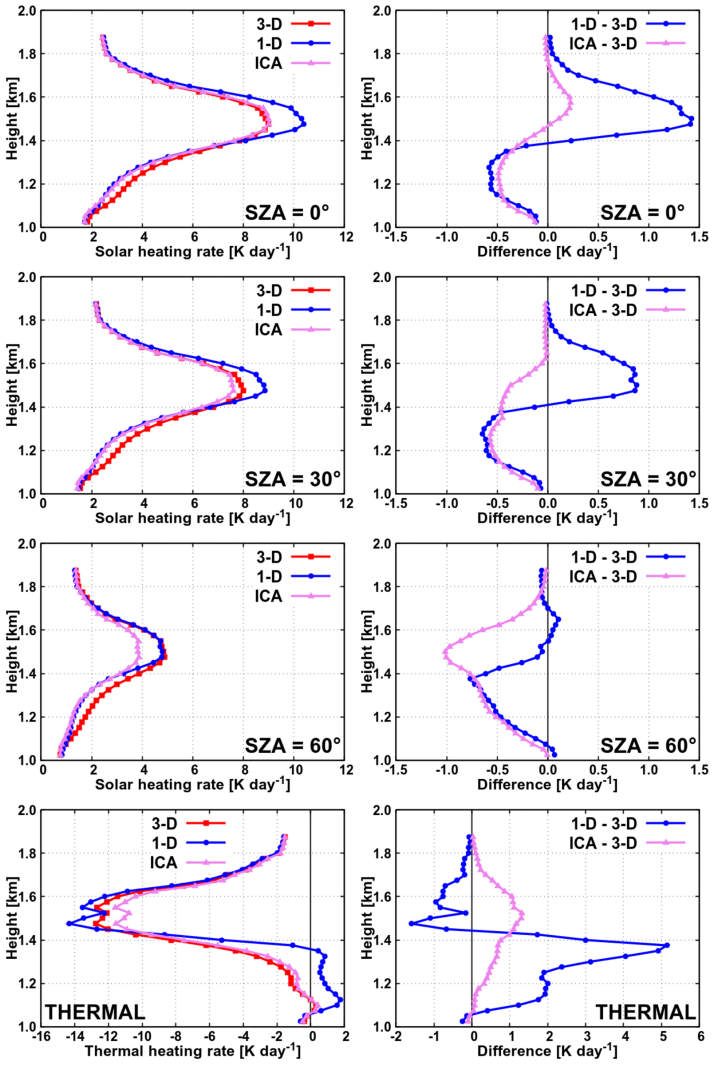

Figure 4.1: *Heating rate in the cloud layer of cumulus cloud scene with total cloud cover of 52.3 % in the experiments with land albedo.*

The height where the maximum heating is reached stays approximately the same for all SZAs. In the thermal spectral range the cloud layer is subjected to strong cooling attaining a peak value of about 13 K day^{-1} again at a height of ∼1.5 km. Below this height, the magnitude of cooling decreases towards the cloud base, where a slight cloud base warming effect is observed.

The difference between the 1-D experiment and the 3-D benchmark (Fig. 4.1, right panels) is as described in the following: in the solar experiments at high Sun (SZA between 0° and 50°) the bias of the 1-D profile shows pronounced vertical gradient within the cloud layer and changes its sign approximately at a height of maximum cloud fraction. In the top part of the cloud layer (i.e., above maximum cloud fraction) the 1-D solar heating rate is too high, while in the bottom part of the cloud layer it is too low, compared to the 3-D

heating rate. In the case of low Sun (SZA of 60° and larger) the 1-D solar heating rate is systematically too low compared to its 3-D counterpart throughout the entire cloud layer. The main reason for that is cloud side illumination (Hogan and Shonk, 2013; Jakub and Mayer, 2015, 2016), which is taken into account in 3-D experiments and completely absent in 1-D calculations.

The ICA calculations help to explain these findings: in the case of overhead Sun the amount of radiative energy hitting cloud tops is practically the same in both ICA and 3-D experiment, yet in the 3-D experiment some of the photons escape through cloud sides (an effect introduced as cloud side escape or loss of photons; O'Hirok and Gautier, 1998a; Hogan and Shonk, 2013), whereas in the ICA approximation the photons remain trapped within individual atmospheric columns. As a consequence, the ICA heating rate is larger than the 3-D heating rate within the top part of the cloud layer (top row of Fig. 4.1). This leakage of photons through cloud sides in the 3-D configuration simultaneously leads to an increased radiation component reaching the ground and being reflected back towards the cloud, which increases the absorption in the bottom part of the cloud layer. For this reason, within the bottom part of the cloud layer, the 3-D heating rate is larger than the ICA one. With increasing SZA the 3-D cloud side illumination effect becomes increasingly more important (overcoming the loss of photons through cloud sides in the upper layers) and the ICA heating rate is found to be systematically too low throughout the entire vertical extent of the cloud layer (at SZA of 30° and larger).

A thorough inspection of the solar experiments in Fig. 4.1 reveals that the 1-D profiles almost completely match the ICA ones in the bottom part of the cloud layer, while in the top part of the cloud layer there is a large discrepancy between the two (at all SZAs). This suggests that "classic 3-D radiative effects" related to horizontal photon transport (discussed above in terms of the difference between ICA and 3-D) can explain the bias of 1-D profiles in the bottom part of the cloud layer (and are thus presumably by far the largest contributor to the overall bias of 1-D profiles in this region). In the top part of the cloud layer, however, the additional error sources accompanying the 1-D experiment, stemming from the misrepresentation of subgrid cloud variability, have to be considered when developing a correction of 1-D solar heating rates based on physical considerations.

In the thermal spectral range, the 1-D experiment overestimates the amount of 3-D cooling in the top part of the cloud layer, whereas in the bottom part of the cloud layer the situation is reversed (a difference of more than 5 K day^{-1} between 1-D and 3-D is observed locally). The ICA experiment, however, underestimates the magnitude of 3-D thermal cooling throughout the entire vertical extent of the cloud layer (with a maximum difference of less than 1.5 K day^{-1}). The latter is as expected, a manifestation of cooling due to horizontal emission of radiation through cloud side areas, which is suppressed in the ICA approximation, but present in the 3-D benchmark (Klinger and Mayer, 2014, 2016). Altogether, this implies that the error arising from the poor representation of subgrid cloud structure additionally affecting the 1-D experiment acts to reduce the positive difference between ICA and 3-D (and even turning it into a negative one) within the top part of the cloud layer and magnifies the positive difference between ICA and 3-D by a factor 3 to 5 within the bottom part of the cloud layer. Once more, the turning point where the 1-D

thermal (absolute) bias changes its sign corresponds well with the height of maximum cloud fraction, where a large vertical gradient of bias is detected as well (bottom right panel of Fig. 4.1). Recall that this is qualitatively similar to that observed in the solar experiments at high Sun, except that the sign of the 1-D solar bias is reversed, meaning that the solar and thermal biases partially compensate each other. The difference between the 1-D and 3-D experiment in the thermal spectral range, however, is quantitatively larger than in the solar spectral range and dominates the total effect of solar and thermal spectral range (for all SZAs). This means that during both daytime and nighttime the bias of the 1-D heating rate profile artificially enhances destabilization of the cloud layer by overestimating both cooling at cloud-layer top and warming at cloud-layer bottom. During daytime, this enhanced destabilization is maximized at low Sun (a difference of up to 5 K day^{-1} between 1-D and 3-D is observed locally at SZA of 80°).

4.1.2 Net surface flux

Net surface radiative flux is directly related to surface heating and thereby affects the development of convection. Furthermore, it enters the surface layer parameterization scheme (e.g., soil and vegetation scheme) of a host weather or climate model and influences various physical processes therein (e.g., hydrological processes, such as melting of snow). Operational 2-m temperature predictions, moreover, are among forecast products of most interest for users, yet they are still subjected to substantial and consistent regional biases in NWP worldwide, partially arising directly from biases of surface radiative fluxes.

Motivated by the desire to understand the causes of the latter, we explore here the net surface flux in the trio (3-D, 1-D, ICA) of experiments on a single cumulus cloud scene with total cloud cover of 52.3 % over land. In the solar spectral range (Fig. 4.2), the net surface flux exhibits profound diurnal variation, decreasing from ∼710 W m^{-2} at overhead Sun to ∼60 W m^{-2} at SZA of 80° in the 3-D experiment (left panel of Fig. 4.2). Similarly, the bias of the 1-D (as well as of the ICA) experiment is strongly dependent on the position of the Sun (middle and right panels of Fig. 4.2). At high Sun (SZA between 0° and 40°) the 1-D experiment underestimates the 3-D benchmark, whereas at low Sun (SZA of 50° and larger) the opposite is the case. While the maximum absolute bias of the 1-D experiment is approximately the same for high and low Sun (about 25 W m^{-2}), the maximum relative bias of 43 % is clearly reached at SZA of 80° due to strongly reduced fluxes at low Sun positions.

Again, we aim to untangle this bias dependence of 1-D experiments on SZA, by first explaining purely the effects of neglected horizontal photon transport. Due to the aforementioned loss of photons through cloud sides, the diffuse downward radiation at the surface in 3-D is larger than in ICA (Wapler and Mayer, 2008). This is the main reason why solar net surface flux in the ICA experiment is underestimated relative to 3-D at Sun angles between 0° and 60°. At SZAs larger than 60°, however, the so-called "elongated shadow effect" (Wissmeier et al., 2013), which is generally present for all Sun positions except for overhead Sun, becomes dominant and solar net surface flux in the ICA experiment is overestimated relative to 3-D. This is essentially the cloud side illumination effect, where the

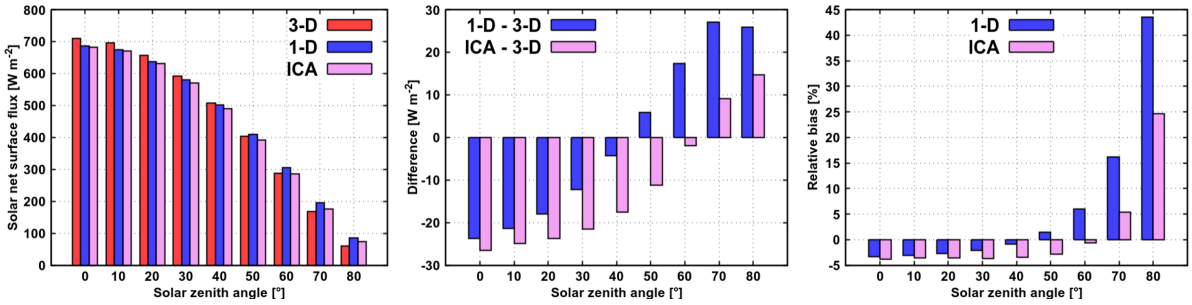

Figure 4.2: *Solar net surface flux for a cumulus cloud scene with total cloud cover of 52.3 % in the experiments with land albedo.*

effective total cloud cover (Di Giuseppe and Tompkins, 2003a; Tompkins and Di Giuseppe, 2007; Hinkelman et al., 2007) increases with descending Sun and hence also the size of the shadow increases with decreasing solar elevation, which is not taken into account in the ICA. This leads to a considerably reduced direct radiation reaching the ground and thus solar net flux in the 3-D experiment when the Sun is lower in the sky.

Both aforementioned shortcomings of ICA manifest themselves in the 1-D experiment as well. For overhead Sun, the apparent reduction of total cloud cover in the 1-D experiment due to the overlap assumption (maximal layer cloud fraction of 37.2 %, which is effectively the total cloud cover in the 1-D experiment, is appreciably lower than the total cloud cover of the 3-D cloud field, that is 52.3 %) acts to increase the amount of direct radiation reaching the surface (compared to 3-D or ICA case), which in turn reduces the net surface flux bias in the 1-D experiment (compared to that in the ICA experiment). When the Sun is from the side, the effective total cloud cover in the 1-D experiment remains 37.2 %, while in the 3-D experiment it is increased well beyond 52.3 %, which further increases the discrepancy in cloud shadow area at the surface in the 1-D and 3-D experiment. In particular, at SZAs larger than 60°, both the absolute and relative bias of the 1-D experiment are by at least a factor of 2 larger than the corresponding biases of the ICA experiment.

In the thermal spectral range the surface cools by emitting more radiation than it receives with a net flux of -62.1 W m^{-2} in the 3-D experiment. The emitted upward flux is given by the Stefan-Boltzmann law and is by definition unbiased in the ICA and 1-D calculations. The ICA downward flux (322.6 W m^{-2}), on the other hand, is somewhat lower than its 3-D counterpart (327.3 W m^{-2}), because the emission of thermal radiation (at a downward angle) through cloud sides, which increases radiation at the surface, is neglected in the ICA approximation (Fig. 1 of Schäfer et al., 2016). Due to the apparent reduction of total cloud cover by the overlap assumption the 1-D downward flux (316.3 W m^{-2}) is even lower than the ICA one. This leads to the thermal net surface flux of -73.1 W m^{-2} in the 1-D experiment. Hence, a difference of -11.0 W m^{-2} between the 1-D and 3-D thermal net surface flux implies an excessive cooling of the surface during nighttime. Finally, observing the total effect during daytime, the 1-D net surface flux is found to underestimate the benchmark 3-D value at SZAs between 0° and 50°, while at larger SZAs the situation is reversed.

4.1.3 Dependence on surface albedo

It is well known that NWP models can have large temperature errors at coastlines (Hogan and Bozzo, 2015). Due to their high computational cost, the radiation schemes are often applied on a coarser spatial grid (compared to the grid of model dynamical core). In regions along coastlines this implies that radiative quantities computed over the ocean are being used at nearby land grid points (where surface temperature and albedo are very different), or vice versa. The alternative practice is averaging input to the radiation scheme onto the coarser grid, which has similar disadvantages.

In the preceding Sections 4.1.1 and 4.1.2 experiments for a solar surface albedo of 0.25 were presented. Here we discuss how the results of these experiments change when the albedo is reduced to a typical oceanic value of 0.05, focusing on the comparison between 1-D and 3-D quantities. As albedo is thus reduced, the solar heating rate within the cloud layer in the benchmark 3-D experiments is reduced, since less radiation is reflected from the surface back towards the cloud. This reduction is largest in the lower part of the cloud layer, whereas at the height where maximum heating is reached (and above), the albedo effect is only marginal. Further, the reduction of solar heating rate with a decreased albedo is largest when the Sun is overhead, where a maximum difference of about 0.8 K day^{-1} is observed between 3-D heating rate profiles in the experiments with A of 0.25 and 0.05, and reduces in significance with descending Sun (at SZA of 80° this difference is imperceptible, essentially less than 0.05 K day^{-1} throughout the entire vertical extent of the cloud layer). This implies that the variation of surface albedo has a comparatively large effect on the benchmark heating rate profile at small SZAs and becomes less important with decreasing elevation of the Sun.

More relevant for this study, the difference between the 1-D and 3-D heating rate profile in the calculations with A of 0.05 stays practically the same as in those with A of 0.25 (with a deviation being mostly less than 0.1 K day^{-1} at all SZAs). This means that the relative bias of the 1-D heating rate profile is generally increased as albedo is decreased. This increase of relative bias is smallest when the Sun is overhead and gains in significance with descending Sun.

Further, at the surface (Fig. 4.3), solar net flux in the 3-D experiment is generally increased as albedo is decreased from 0.25 to 0.05 (lower surface reflectivity implies more radiation is absorbed in the surface). This increase is largest for overhead Sun, where the 3-D net surface flux is increased from ∼710 W m^{-2} to ∼850 W m^{-2} and reduces in significance with descending Sun. The difference between the 1-D and 3-D net surface flux in the experiments with A of 0.05 stays approximately the same as in those with A of 0.25, at least at relatively high Sun (with a deviation of less than 2 W m^{-2} at SZA between 0° and 20°). When the Sun is lower in the sky (SZA of 50° and larger), however, the overestimation of net surface flux in the 1-D experiment with A of 0.05 is enlarged (compared to the overestimation in the 1-D experiment with A of 0.25), although not more than by an additional 6 W m^{-2}. On the whole, the relative bias of the 1-D net surface flux over the ocean stays approximately the same as over land (with a deviation of less than 2 % at all SZAs).

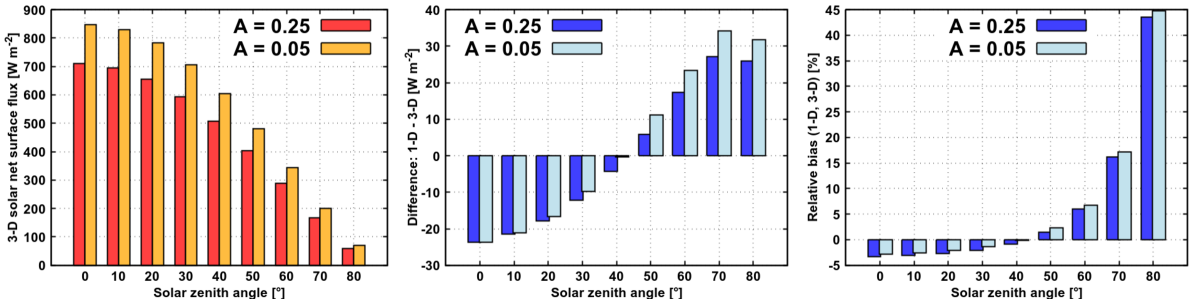

Figure 4.3: *Solar net surface flux for a cumulus cloud scene with total cloud cover of 52.3 % in the experiments with land and oceanic albedo.*

Referring back to the findings of Hogan and Bozzo (2015), our results regarding the sensitivity of the 3-D benchmarks on the variation of surface albedo confirm that along coastlines the radiative quantities should be computed on the regular grid (at least at higher Sun elevations). The fact that the absolute bias of cloud-layer heating rate is approximately the same over land and ocean and that the relative bias of net surface flux over land and ocean is approximately the same as well, indicate the possibility of eliminating one parameter (namely the surface albedo) when developing a correction for NWP radiative quantities (after the robustness of the results is proved for diverse cloud scenarios).

4.1.4 Dependence on cloud cover

We examine now the dependence of heating rates and surface fluxes on cloud cover (in addition to their dependence on SZA and albedo) by analysing the entire data set of ten cumulus cloud scenes. We present the benchmark 3-D experiments first and then discuss the bias of 1-D experiments (noting that the ICA experiments are investigated in the next section, where additionally the dependence on LWP is examined). Thus in the 3-D solar experiments over land, the heating rate within the cloud layer generally becomes larger with increasing CC of the cloud scene. At overhead Sun, for example, a peak heating rate of ∼3 K day^{-1}, ∼9 K day^{-1} and ∼43 K day^{-1} in the experiments on cloud scenes with CC of 12.0 %, 52.3 % and 98.9 %, respectively (Fig. 4.4, top left panel). The height where the peak heating is reached does not vary with SZA and is slightly above the height of maximum cloud fraction of a given cloud scene (the latter differs from scene to scene, since both the vertical extent of the cumulus cloud layer as well as the height of the maximum cloud fraction generally increase during the course of UCLA-LES simulation). Similarly, in the 3-D thermal experiments, the main cloud-radiative effects described in Section 4.1.1 (cloud top cooling, cloud side cooling, cloud base warming) in general become more pronounced as CC is increased. The peak magnitude of cooling, for example, equals to ∼4 K day^{-1}, ∼13 K day^{-1} and ∼76 K day^{-1} in the experiments on cloud scenes with CC of 12.0 %, 52.3 % and 98.9 %, respectively (Fig. 4.4, bottom left panel). The height where this peak thermal cooling is attained at a given cloud scene corresponds well with the height of peak

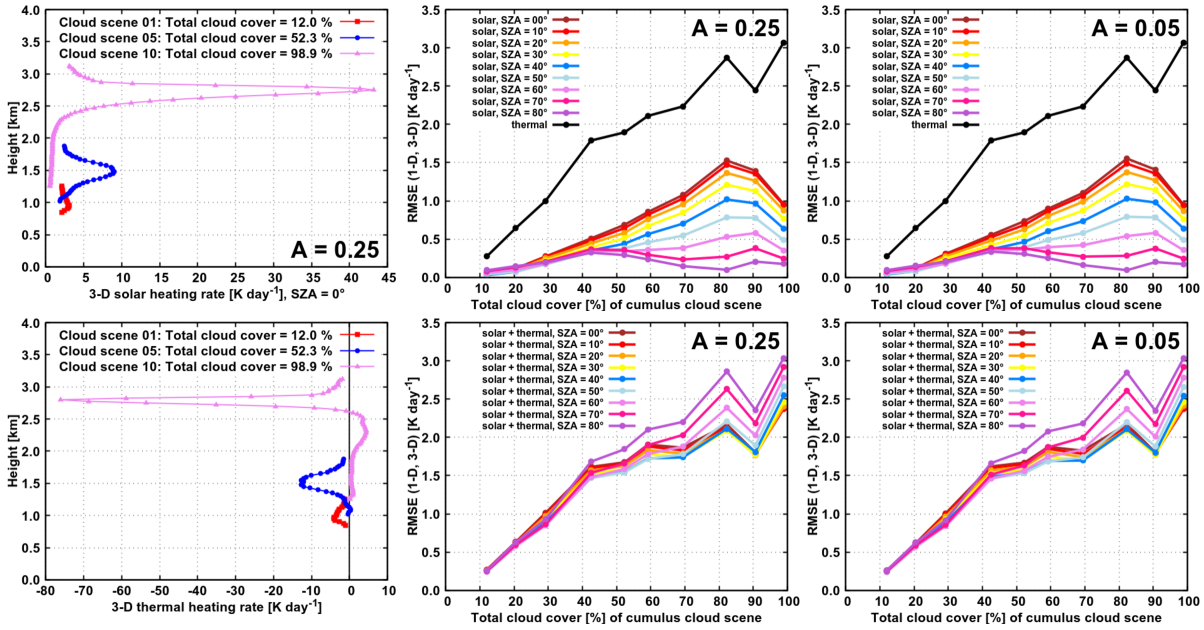

Figure 4.4: *The benchmark 3-D solar heating rate in the experiments with overhead Sun and land albedo (top left panel) and thermal heating rate (bottom left panel) in the cloud layer for the three selected cloud scenes with total cloud cover of 12.0 %, 52.3 % and 98.9 %. The cloud-layer RMSE between the pair (1-D, 3-D) of heating rate profiles for the entire set of ten cumulus cloud scenes, characterized by their total cloud cover, in the experiments with land (middle panels) and oceanic (right panels) albedo. Top panels show the RMSE in the solar and thermal spectral range separately, whereas the bottom panels show the RMSE between the pair of total profiles.*

solar heating.

The cloud-layer RMSE between the pair (1-D, 3-D) of heating rate profiles generally increases with CC and reaches a maximum value of 1.5 K day^{-1} for overhead Sun in the solar spectral range and a maximum value of 3.0 K day^{-1} in the thermal spectral range (Fig. 4.4, top middle panel). Although the RMSE is a good measure of an averaged difference between the 1-D and 3-D heating rate profiles, locally the difference between 1-D and 3-D can be much larger. For the stratocumulus scene with CC of 98.9 %, for example, the cloud top cooling is overestimated by about 15 K day^{-1} and the cloud base warming is overestimated by about 10 K day^{-1} in the 1-D thermal experiment. The discrepancy between the 1-D and 3-D profile in the thermal spectral range is quantitatively larger than in the solar spectral range and dominates the daytime RMSE at all CC. Nevertheless, during daytime, the difference between the 1-D and 3-D solar heating rate partially compensates the corresponding thermal heating rate difference. The degree of compensation is smallest at SZA of 80° and increases with increasing solar elevation (Fig. 4.4, bottom middle panel). The dependence of daytime RMSE on SZA is generally stronger at larger CC.

In the solar experiments over the ocean, the 3-D benchmark heating rate within the cloud layer is in general somewhat lower than that in the experiments over land, although this effect is prevailing at small CC and becomes less apparent at larger CC. At overhead

Sun, for example, a peak heating rate is reduced by 0.5 K day^{-1}, 0.6 K day^{-1} and 0.1 K day^{-1} in the experiments over the ocean (compared to the experiments over land) on cloud scenes with CC of 12.0 %, 52.3 % and 98.9 %, respectively. This implies the relative changes of about 16.7 %, 6.7 % and 0.2 %, respectively. The RMSE between the pair (1-D, 3-D) of solar heating rate profiles in the experiments over the ocean (Fig. 4.4, top right panel) shows a remarkably similar dependence on SZA and CC as the RMSE in the experiments over land. The discrepancy between the RMSE values over land and ocean (at a given SZA and CC) is less than 0.1 K day^{-1}. This suggests that the conclusions regarding the absolute bias of cloud-layer heating rate drawn in Section 4.1.3 could be generalized to the entire set of cumulus scenes.

Figure 4.5 shows the net surface flux as a function of SZA and CC in the experiments over land. In the solar spectral range, at a given CC, the 3-D net surface flux decreases with increasing SZA, yet this decrease is stronger at smaller values of CC and reduces in significance as CC is increased. At a given SZA, on the other hand, the 3-D net surface flux gently decreases with increasing CC, up to a CC of ∼90 %, followed by a sharper drop towards considerably lower flux in the case of the fully-covered scene. In the thermal spectral range the surface cools by emitting more radiation than it receives at all CC. While the upward emission of the surface (389.5 W m^{-2}) is independent of CC, the downward flux at the surface increases with increasing CC. Consequently, thermal net surface flux increases with increasing CC as well. Quantitatively, the net surface flux in the solar spectral range is larger than that in the thermal spectral range, except at SZA of 80°, where the total net surface flux is close to zero (for all values of CC). In the solar spectral range, the 1-D experiment generally overestimates the corresponding 3-D experiment at low Sun (bias up to 30 W m^{-2} or 45 %), while at high Sun the opposite is the case (bias up to −60 W m^{-2} or −10 %). This positive bias at low Sun is largest at intermediate range of CC, while negative bias at high Sun is peaked at larger CC (80 % and beyond). In the thermal spectral range, the 1-D experiment overestimates the amount of 3-D cooling, with the maximal effect (−10 W m^{-2} or 20 %) peaked at intermediate range of CC. The daytime bias at the surface (Fig. 4.5, bottom middle and right panels) is clearly governed by the solar fluxes. Nevertheless, especially at low Sun, when solar fluxes are considerably reduced, thermal fluxes play a role in modulating the surface bias as well.

In the solar experiments over the ocean (not shown), the 3-D net surface flux is generally larger than that in the experiments over land (e.g., for the cloud scene with CC of 12.0 %, a benchmark value of ∼1040 W m^{-2} is found at SZA of 0° and ∼470 W m^{-2} at SZA of 60°). Interestingly, the absolute bias of the 1-D experiment over the ocean at a given SZA and CC is increased (compared to its counterpart over land) by such an amount that the relative bias of the 1-D experiment stays approximately the same as over land (with a deviation of less than 2 %), hinting that the conclusions regarding the surface bias drawn in Section 4.1.3 can be generalized to the entire set of diverse cumulus scenarios.

Finally, the reader should keep in mind, that the results presented in this section should not be interpreted solely as a function of CC. With increasing CC of the scenes from the set, the cloud optical thickness increases as well. This is because both the geometrical thickness and cloud liquid water increase during the evolution of the cloud field (prior

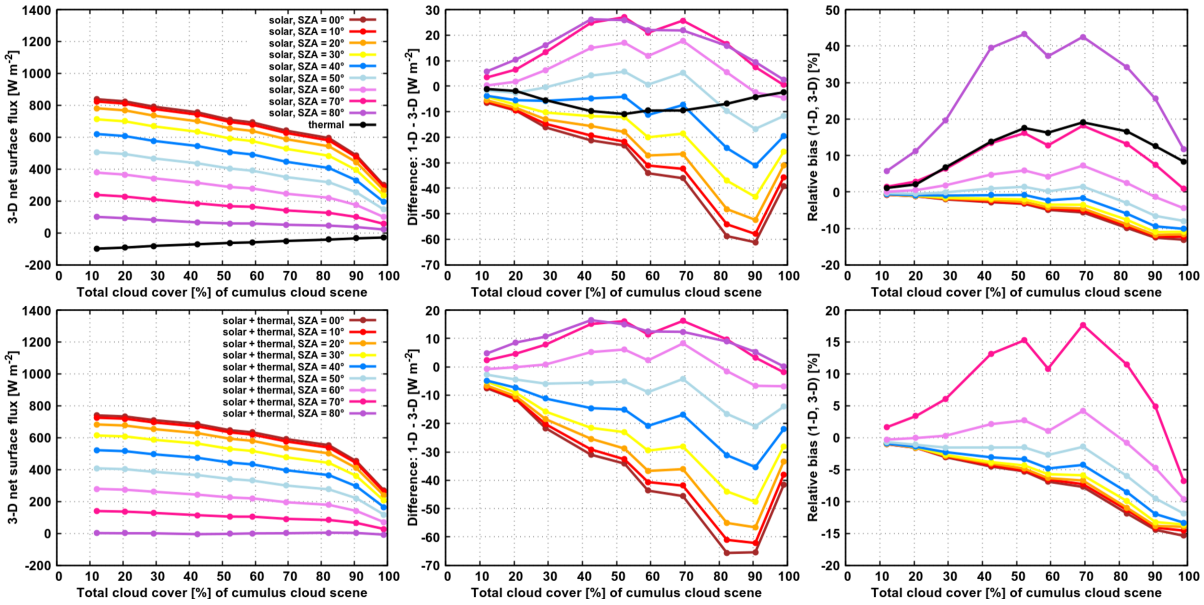

Figure 4.5: *Net surface flux for the ten cumulus cloud scenes, characterized by their total cloud cover, in the experiments with land albedo. Top row shows the results in the solar and thermal spectral range separately, whereas the bottom row shows the total effect of solar and thermal spectral range (large relative bias of total flux at SZA of 80° is off the scale and not shown on plot).*

to the rain formation), which would also be expected in the real world. Further, apart from CC and LWP, there are plenty of other factors that change from scene to scene and affect the outcome of 3-D experiments and thus the bias of the 1-D calculation. These factors include 3-D cloud geometry, the number of individual clouds in the domain and their spatial distribution.

4.1.5 Statistical synthesis and dependence on liquid water path

In order to obtain a larger data set and thus at least partially overcome the issues discussed in the last paragraph of the previous section, we slightly change the methodology that has been used so far. Namely, for each of the ten cloud scenes, we sample a number of sub-scenes ("windows"), with a horizontal size of 2.8 x 2.8 km^2 at various (x, y)-coordinates within the domain. In order to create the 1-D experiment, the cloud optical properties within each window are averaged in the same manner as described in the methodology chapter and the two-stream method with maximum-random overlap assumption is called once per window. The 3-D and ICA experiments are then created by averaging the heating rates and surface fluxes, precalculated on highly resolved cloud fields (i.e., retaining the resolution from LES), over the same window region. Further, within each window, a total cloud cover of 3-D cloud field as well as averaged cloud liquid water path are calculated (allowing us to examine the dependence on both CC *and* LWP). In this way a total of 1000

windows are analyzed for each of the three selected SZAs (0°, 30° and 60°) at each of the two surface albedos in the solar spectral range and also 1000 windows in the thermal spectral range. Figures 4.6 and 4.7 show the resulting scatter plots, where each dot represents the result of one window (note that on subfigures, where the results for the three SZAs in the solar experiments are shown simultaneously, only one quarter of analyzed windows is displayed). It is immediately apparent that there is a strong correlation between CC and LWP. As previously suggested, this means that the findings regarding the dependencies on total cloud cover of selected cloud scenarios might be obtained similarly if the cloud scenarios were represented in terms of their optical thickness (but for the sake of brevity we refer to this dependence solely as "CC dependence").

On the whole, the analysis of multiple windows confirms the conclusions that have been drawn in Section 4.1.4 qualitatively (regarding the bias dependence on SZA, A, CC), but extends the range of bias quantitatively. Thus the RMSE between the pair (1-D, 3-D) of solar heating rate profiles in the experiments over land increases with CC and reaches a maximum value of ∼3.0 K day^{-1} for overhead Sun (Fig. 4.6, top left panel), which is about twice as large as the corresponding maximum based on the individual examination of the ten cloud scenes. This suggests that the results of the case studies should be taken with caution and demonstrates the general need for statistics. The RMSE between the pair (ICA, 3-D) of solar profiles in the experiments over land (Fig. 4.6, top right panel) exhibits a different dependence on SZA and CC than the RMSE between the pair (1-D, 3-D). The RMSE (ICA, 3-D) peaks at intermediate CC, besides it is smallest for overhead Sun and increases with descending Sun (cloud side illumination effect), which is the opposite to the RMSE (1-D, 3-D).

In the solar experiments over the ocean (not shown), the RMSE (1-D, 3-D) as well as the RMSE (ICA, 3-D) exhibit a qualitatively similar dependence on SZA and CC as their counterparts over land. The discrepancy between the RMSE (1-D, 3-D) over land and ocean at SZA of 0°, for example, is less than 0.04 K day^{-1} in 75 percent of the windows and less than 0.07 K day^{-1} in 95 percent of the windows. Overall, this discrepancy is less than 0.1 K day^{-1} in *all* windows examined.

The RMSE between the pair (1-D, 3-D) of thermal heating rate profiles (Fig. 4.6, bottom left panel) approximately linearly increases with CC and reaches a maximum value of ∼5.5 K day^{-1}. The RMSE between the pair (ICA, 3-D) of thermal profiles (Fig. 4.6, bottom right panel) exhibits a significantly different dependence on CC than the RMSE between the pair (1-D, 3-D). As anticipated, the maximum RMSE (ICA, 3-D) of ∼1.0 K day^{-1} is reached at intermediate range of CC, where cloud side (lateral) area is maximized. This lateral surface area of clouds, namely, is the primary region subjected to strong 3-D cooling, which is neglected by the ICA. As intermediate CC is decreased (increased) towards smaller (larger) values, the cloud side area generally reduces and so does the RMSE (ICA, 3-D). At CC of 100 %, however, the RMSE (ICA, 3-D) does not fall to zero. This RMSE of about 0.5 K day^{-1} on average is a reminder of an important component of in-cloud horizontal photon transport between optically thicker and optically thinner regions of the cloud, leading to a discrepancy between the ICA and 3-D experiment even at overcast scenarios, where cloud side area is negligible. Furthermore, since overcast cloud scenarios

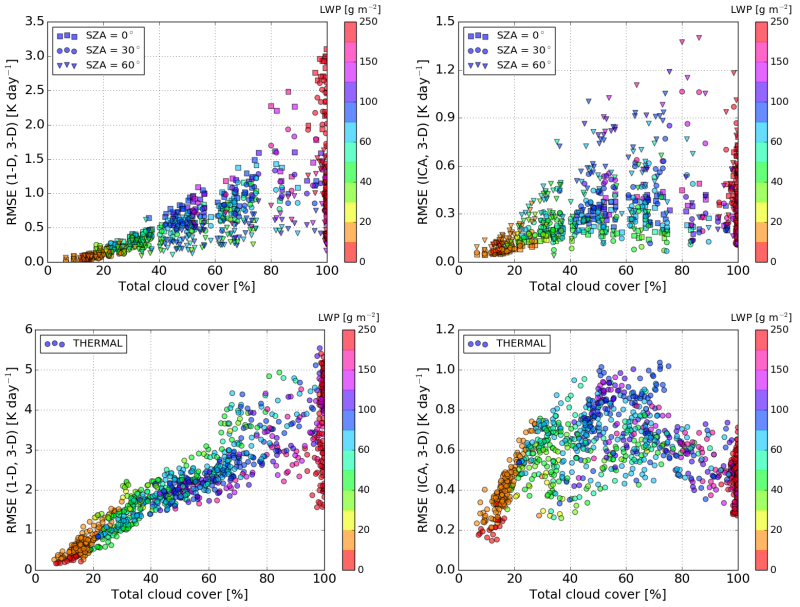

Figure 4.6: *The cloud-layer RMSE between the pair (1-D, 3-D) and the pair (ICA, 3-D) of solar (top row) and thermal (bottom row) heating rate profiles in the experiments with land albedo.*

are more or less maximally overlapped, the major error source responsible for the much larger RMSE between (1-D, 3-D) compared to the RMSE between (ICA, 3-D) of thermal profiles is attributed to the neglection of cloud horizontal heterogeneity.

To synthesize, the ICA is overall more accurate than the 1-D experiment. This suggests that the poor representation of cloud structure in the 1-D experiment has a profound impact on the cloud-layer heating rate. This is especially true in the thermal spectral range and in the solar spectral range at high Sun, at intermediate and large CC, where the RMSE (1-D, 3-D) greatly surpasses the RMSE (ICA, 3-D).

Examining the dependence on LWP (at a given SZA, A, CC) we find that in the solar spectral range the RMSE (1-D, 3-D) and the RMSE (ICA, 3-D) both increase with increasing LWP. In the thermal spectral range, on the other hand, the dependence of RMSE on LWP is less straightforward, because thermal emission quickly saturates (Fig. 1 of Petters et al., 2012).

Observing the net surface flux (Fig. 4.7) it is found that the 1-D solar experiment overestimates the corresponding 3-D experiment at low Sun (e.g., at SZA of 60°, bias up to 150 W m^{-2} or 80 % over land and 200 W m^{-2} or 80 % over the ocean), while at high Sun the opposite is the case (e.g., at SZA of 30°, bias up to −200 W m^{-2} or −40 % over land and −250 W m^{-2} or −40 % over the ocean). This positive bias at low Sun is largest at intermediate CC, while negative bias at high Sun is peaked at larger CC. In the thermal spectral range, the 1-D experiment overestimates the amount of 3-D surface cooling with the maximal effect (−25 W m^{-2} or 50 %) peaked at intermediate CC. The bias of the ICA experiment exhibits a qualitatively similar dependence on SZA, A and CC as the bias of the 1-D experiment (in both the solar and thermal spectral range). Although not

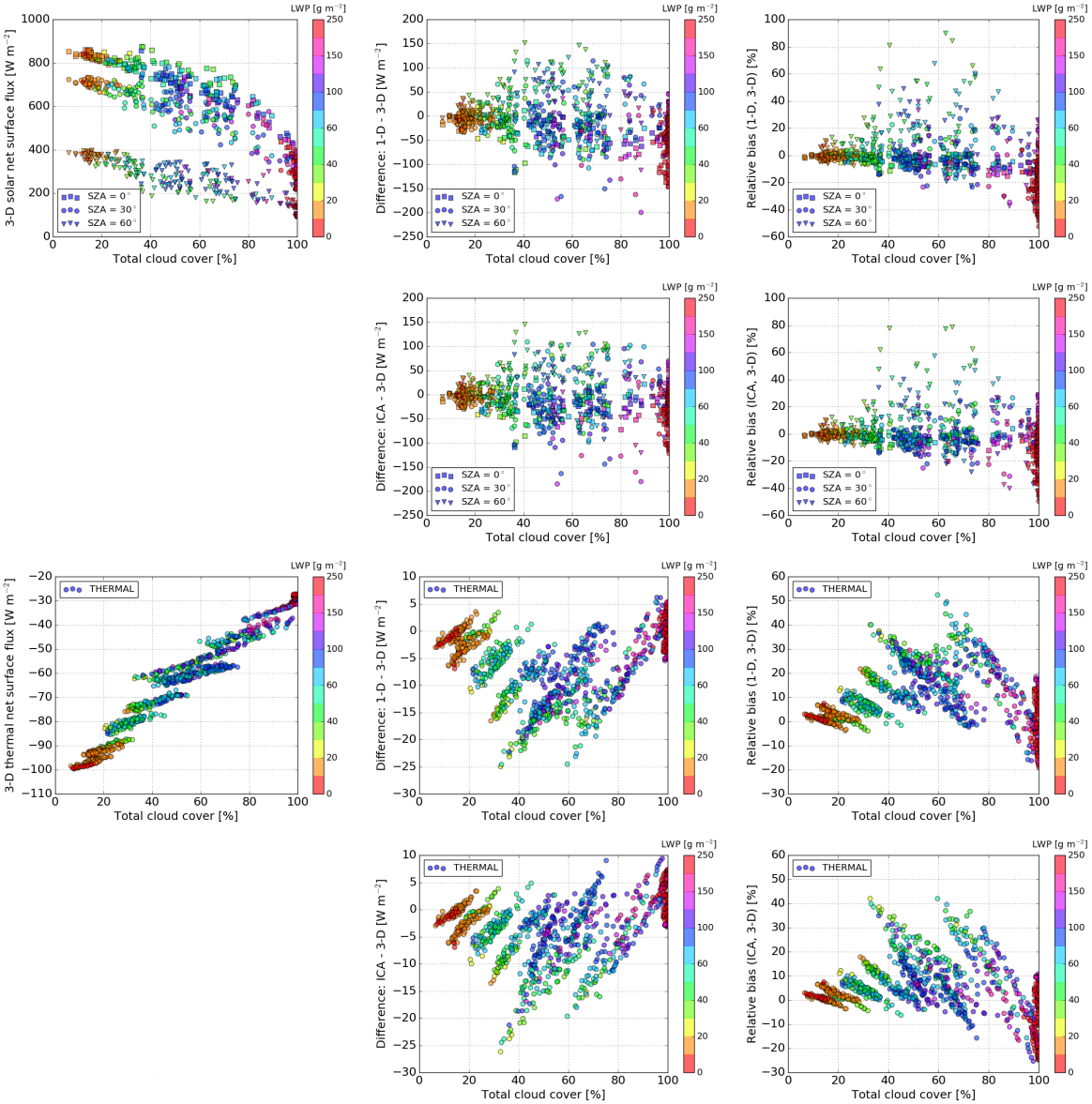

Figure 4.7: *Solar (the first and the second row) and thermal (the third and the fourth row) net surface flux in the experiments with land albedo.*

immediately apparent from the scatter plots, the mean ICA bias is quantitatively lower than the mean 1-D bias, which suggests that the poor representation of clouds affects the 1-D surface bias as well.

Examining the dependence on LWP (at fixed values of other parameters) we find that the 3-D solar net surface flux decreases with increasing LWP (at least for overhead Sun). The 3-D thermal net surface flux (at a fixed CC) shows little dependence on LWP. Similarly, the dependence of surface biases on LWP is difficult to elucidate. Further investigation is needed to better quantify these effects.

4.2 Exploring the potential of the Tripleclouds method for various cloud types

The radiative biases at the scale of global models are examined hereafter, primarily aiming to explore the potential of the Tripleclouds method for various cloud types. In Section 4.2.1 the atmospheric heating rate for each cloud type is exposed, whereas in Section 4.2.2 the net surface flux is presented. We examine first the 3-D benchmarks, then discuss the ICA shortcomings, investigate the conventional GCM and finally focus on the baseline Tripleclouds experiments. Based upon the results of the latter, some optimized Tripleclouds configurations are further explored in Section 4.2.3.

4.2.1 Atmospheric heating rate

Cumulus

Figure 4.8 (left) shows the radiative heating rate in the benchmark 3-D experiment for the cumulus cloud. In the solar spectral range for overhead Sun there is a large absorption of radiation in the cloud layer, resulting in a peak heating rate of 10.8 K day^{-1}. The latter is reached in the central part of the cloud layer, slightly above the height of maximal cloud fraction. With decreasing Sun elevation the solar heating rate diminishes, exhibiting the maximum of 9.4 and 5.5 K day^{-1} at SZAs of 30° and 60°, respectively. The height where the peak heating is reached stays the same at all SZAs. In the thermal spectral range the cloud layer is subjected to strong cooling, reaching a peak value of 17.7 K day^{-1} attained at the same height as the maximum solar heating. Below this height, the magnitude of cooling decreases towards the cloud base, where a slight cloud base warming effect is observed. The total heating rate, a physically relevant quantity during daytime, is dominated by stronger thermal radiative effect. These findings are overall similar to those documented in Section 4.1.1, where a shallow cumulus with intermediate cloud cover was also investigated, albeit simulated on a smaller domain.

The investigation of radiative biases (Fig. 4.8, middle and right) reveals that these are maximized in the central part of the cumulus layer as well. The disparity between ICA and 3-D increases with descending Sun (cloud side illumination), reaching a maximum of -0.7 K day^{-1} at SZA of 60°. The strength of thermal cooling is underestimated up to 1.0 K day^{-1} in the ICA, since realistic cloud side cooling is neglected.

The main shortcomings of the GCM experiment are as follows. In the solar spectral range the peak heating rate is overestimated by about 2.7, 2.1 and 0.8 K day^{-1} at SZAs of 0°, 30° and 60°, respectively. In the bottom part of the cloud layer, on the contrary, the heating rate is underestimated, although not more than by 0.4 K day^{-1} at all SZAs. In the thermal spectral range the GCM bias artificially enhances radiatively driven destabilization of the cloud layer by an overestimation of cloud top cooling by 6.0 K day^{-1} and an overestimation of cloud base warming by 3.4 K day^{-1}. The solar and thermal GCM biases therefore partially compensate during daytime. Nevertheless, the stronger thermal

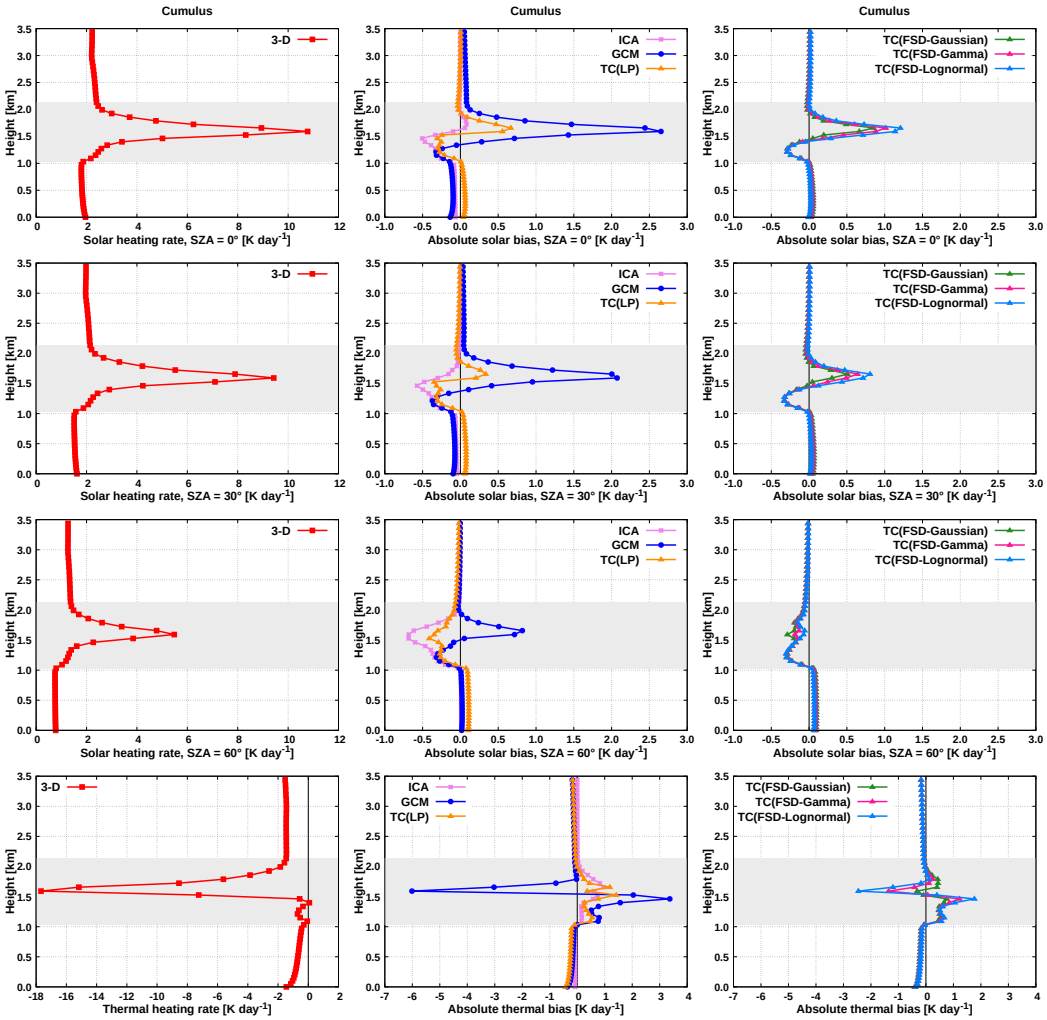

Figure 4.8: *Radiative heating rate for the cumulus cloud. The grey-shaded area denotes the cloud layer.*

radiative effect implies persistent cloud layer destabilization during nighttime and daytime.

The present findings regarding cumulus cloud-radiative biases are again to some extent in concordance with those presented in the previous section for a snapshot of evolving shallow cumulus cloud field with intermediate cloud cover at the scale of regional models. It was however shown that at global scale the effect of neglected horizontal photon transport plays a comparatively minor role in relation to the effect stemming from the poor cloud structure representation. This indicates the large potential for the Tripleclouds method to be used in coarse-resolution global models, since it depletes the bias arising from the misrepresentation of subgrid cloud variability, but not the horizontal photon transport. In this first case study involving the cumulus cloud, Tripleclouds will be evaluated in more detail within the following two paragraphs to expose and elucidate cloud heterogeneity issues.

Tripleclouds with LP method

We assess first the TC radiative solver when the LP method is used to obtain the pair of LWC. The results of this experiment, denoted as "TC(LP)", are shown in Fig. 4.8 (middle) and Fig. 4.9. It is apparent that the TC(LP) is overall significantly more accurate than the GCM. In the solar spectral range for overhead Sun (Fig. 4.8, top middle), the maximal bias within the cloud layer is reduced from 2.7 K day^{-1} to only 0.7 K day^{-1}. Whereas the largest bias reduction is observed within the cloud layer, the heating rate above and below the cloud layer is considerably improved as well, explained as follows. The non-homogeneous clouds have lower mean shortwave albedo and absorptivity than the corresponding homogeneous cloudiness with the same mean optical depth (Fig. 2 of Cairns et al., 2000). This implies that the non-homogeneous cloud in the TC configuration reflects less of the incoming solar radiation upward (leading to a reduction of the positive GCM bias above the cloud layer) and simultaneously absorbs less radiation (leading to a reduction of the positive GCM bias in the cloud layer), compared to the homogeneous cloud in the GCM. Consequently, more radiation is transmitted through the cloud layer and absorbed in the region below the cloud layer in the TC experiment compared to that in the GCM, which reduces the negative GCM bias in this region. At SZA of 30° the behavior is qualitatively similar, with the maximal bias of 2.1 K day^{-1} within the cloud layer reduced by a factor of 5. At SZA of 60°, the maximal bias of 0.8 K day^{-1} within the cloud layer becomes of the opposite sign, but is still smaller in magnitude (-0.4 K day^{-1}), when the TC(LP) is applied in place of the conventional GCM. In the layer above and especially below the cloud layer, however, the bias is slightly increased. Finally, it should be noted that at low Sun (SZAs of 30° and 60°) the TC is generally even more accurate than the ICA, which could be partially due to effective treatment of solar 3-D effects in the TC scheme. It is noteworthy that, at all three SZAs, the 3-D radiation feature at cloud base (increased heating due to surface reflection of radiation) cannot be properly accounted for using the TC solver.

In the thermal spectral range (Fig. 4.8, bottom middle), the degree of artificially enhanced destabilization of the cloud layer, arising from the overestimation of cloud top cooling and cloud base warming in the GCM, is drastically reduced when the TC(LP) is applied, interpreted as follows. The non-homogeneous clouds have lower mean longwave emissivity and absorptivity than the corresponding homogeneous clouds with the same mean optical depth. Thus the non-homogeneous cloud top in the TC experiment emits less radiation compared to the homogeneous cloud top in the GCM configuration, which reduces the negative GCM bias at cloud top. Similarly, the non-homogeneous cloud base in the TC experiment absorbs less of the radiation stemming from the warmer atmospheric layers underneath the cloud, compared to the homogeneous cloud base in the conventional GCM, which reduces the positive GCM bias at cloud base. As anticipated, in the region above and below the cloud layer, the difference between the TC and the GCM is only marginal. It is noteworthy that the TC performs similarly well to the ICA also in the thermal spectral range, implying that the realistic subgrid cloud variability can be adequately represented by a two-point probability density function (PDF).

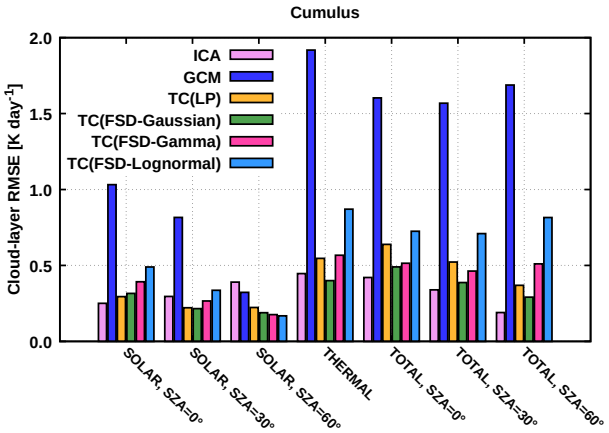

Figure 4.9: *Cloud-layer RMSE in the experiments for the cumulus cloud.*

Tripleclouds with FSD method

We investigate now the TC experiments applying the FSD method together with global FSD estimate, shown in Fig. 4.8 (right) and Fig. 4.9. The TC(FSD) experiment assuming the Gaussianity of cloud condensate is examined first − this experiment is considerably more accurate than the conventional GCM as well. As an illustration, the daytime cloud-layer RMSE of 1.7 K day^{-1} is reduced to 0.3 K day^{-1} at SZA of 60° (Fig. 4.9). Furthermore, the TC(FSD) experiment is even slightly more accurate than the TC(LP) especially in the thermal spectral range and in the solar spectral range at SZAs of 30° and 60°, whereas at SZA of 0° the situation is reversed (Fig. 4.8). The largest discrepancy between the two TC experiments is observed in the central part of the cloud layer and is attributed to the fact that the actual layer LWC distribution of the present shallow cumulus deviates from the assumed Gaussian distribution as well as that the actual FSD deviates from the assumed global estimate.

When examining the entire set of TC(FSD) experiments with global FSD it is apparent that the radiative heating rate is considerably more accurate compared to the conventional GCM regardless of the exact assumption for the LWC distribution. Although the Gaussian distribution was ranked worst when fitted to the actual PDF, the Gaussianity assumption with global FSD performed best in practice, contemplated as follows. In the central part of the cloud layer around maximum cloud fraction the actual FSD of the present shallow cumulus (0.95) is larger than the assumed global estimate. The latter is primarily due to great amount of cloud side area in this region, an essential characteristic of broken cloud field, which generally contributes to increased variability (Boutle et al., 2014; Hill et al., 2012, 2015). Since the assumption of Gaussianity implies the largest difference between the LWC pair characterizing the two cloudy regions (Figs. 3.12 and 3.15), it partially accounts for the missing variability provided by the global estimate. More sophisticated parameterizations are desired to be developed in the future.

Stratocumulus

Figure 4.10 (top row) shows the radiative heating rate in the benchmark 3-D experiment for the stratocumulus cloud. There is large absorption of solar radiation in the cloud layer, resulting in the maximum heating rate of about 53, 47 and 27 K day^{-1} at SZAs of 0°, 30° and 60°, respectively. The peak heating rates are concentrated in the uppermost part of the cloud layer, since both cloud fraction and LWC generally increase from cloud base towards cloud top. In the thermal spectral range the cloud layer is subjected to strong cooling, reaching a peak of almost -140 K day^{-1} at the same height where maximum solar heating is attained. These large heating and cooling rates are partially a manifestation of high vertical resolution (Di Giuseppe and Tompkins, 2003a). The daytime heating rate is dominated by thermal cooling. Thus persistent cloud-top radiative cooling, a typical feature of marine stratocumulus-topped boundary layers (STBLs; Wood, 2012), drives convective instability and controls turbulence within the underlying mixed layer (Randall, 1980; Deardorff, 1981; Stevens et al., 1999), when adequately coupled to a dynamical model. The radiative biases could therefore importantly affect the evolution of the stratocumulus layer itself.

The examination of radiative biases (Fig. 4.10, bottom row) reveals that these are maximized in the uppermost part of the stratocumulus layer as well. The disparity between the ICA and 3-D is minor: a maximum difference of -0.2 K day^{-1} is observed in the solar spectral range for SZA of 60° (cloud side illumination effect). In the thermal spectral range, the ICA underestimates the amount of 3-D cooling by about 2.5 K day^{-1} in the uppermost grid point of the cloud layer (cloud side cooling effect). These comparatively small ICA biases are attributed to the minor cloud top topography (difference between the nearby local height maximum and minimum; Zuidema and Evans, 1998) of the present stratocumulus. The radiative transfer, namely, acts to smooth out structures at spatial scales smaller than the photon mean free path, with the latter corresponding to several hundred meters in STBLs (Marshak et al., 1985).

The GCM bias exhibits a pronounced vertical gradient within the cloud layer: in the uppermost part of the cloud layer the GCM solar heating rate is too high, while in the region underneath it is too low (at all SZAs). In the thermal spectral range the opposite is the case, but the bias is quantitatively larger and dominates the daytime bias. Thus the GCM boosts radiatively driven destabilization of the stratocumulus layer during daytime and nighttime, by overestimating cooling at the uppermost region of the layer (bias of -14 K day^{-1}) and overestimating warming in the region underneath (bias up to 9 K day^{-1}).

In the Tripleclouds experiments the solar bias is increased compared to that of the GCM. This is most notable when using the FSD method, since the global FSD introduces excessive heterogeneity in the radiatively important upper part of the cloud layer. In the thermal spectral range the TC in most configurations outperforms the conventional GCM. Further, the TC appears to be strongly sensitive to the assumed condensate distribution, highlighting its importance, with the lognormality assumption performing best. Noteworthy, although the TC with global FSD degrades the solar bias, it is still more accurate than the GCM during all nighttime and daytime conditions, when LWC lognormality is assumed (Fig. 4.13, left). In particular, nocturnal cloud-layer RMSE is reduced from about

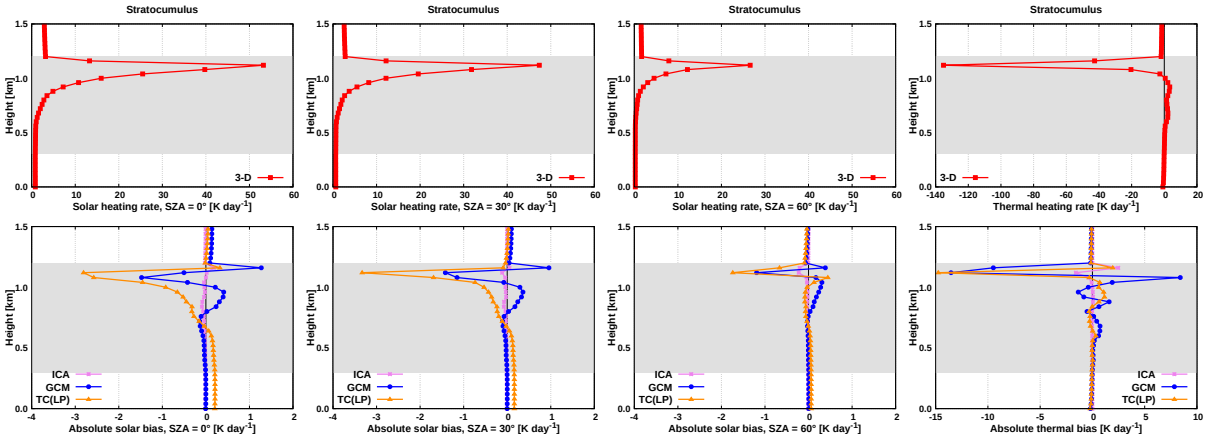

Figure 4.10: *Radiative heating rate for the stratocumulus cloud. The grey-shaded area denotes the cloud layer.*

3.9 K day^{-1} to only 2.1 K day^{-1}. The largest daytime improvement is observed at SZA of 60°, where RMSE is reduced from 4.1 K day^{-1} to solely 1.8 K day^{-1}.

Cirrus

Figure 4.11 (top row) shows the radiative heating rate in the benchmark 3-D experiment for the cirrus cloud. The solar absorption in the ice layer results in a maximum heating rate of about 3.6, 3.3 and 2.2 K day^{-1} at SZAs of 0°, 30° and 60°, respectively. The height where this maximum heating is reached stays the same for all SZAs and corresponds to the height of maximum cloud fraction (7.6 km). In the thermal spectral range a peak cooling of −2.9 K day^{-1} is attained higher up in the cloud layer (at 8.7 km; effective cloud top; above this height cloud fraction rapidly decreases), followed by a peak warming of 1.5 K day^{-1} located at the height of maximum IWC (7.1 km; effective cloud base; below this height IWC is sharply reduced). In contrast to the stratocumulus, solar heating and thermal cooling observed on the cirrus is generally more evenly distributed throughout the cloud layer, whereas thermal warming remains confined to a shallow region at cloud base. The daytime heating rate is governed by the stronger thermal effect, although solar heating largely compensates thermal cooling. Compared to the stratocumulus, the heating rate observed on the cirrus is overall much lower. Nevertheless, it should be kept in mind that the net heating rate in the upper troposphere and lower stratosphere (UTLS) is close to zero (Haigh, 1984), which makes this region highly sensitive to small radiative biases.

The 3-D solar effects (Fig. 4.11, bottom row) are present at all SZAs and maximized at 60° (cloud side illumination), where the ICA bias of −0.1 K day^{-1} is observed throughout the majority of the cloud layer. In the thermal spectral range, the ICA bias is negligible. Similar results were found by Zhong et al. (2008) (recall that the latter investigated the same midlatitude cirrus, although on coarser grid), who also showed that domain-averaged ICA and 3-D heating rates agree within 0.1 K day^{-1} in both the longwave and the shortwave.

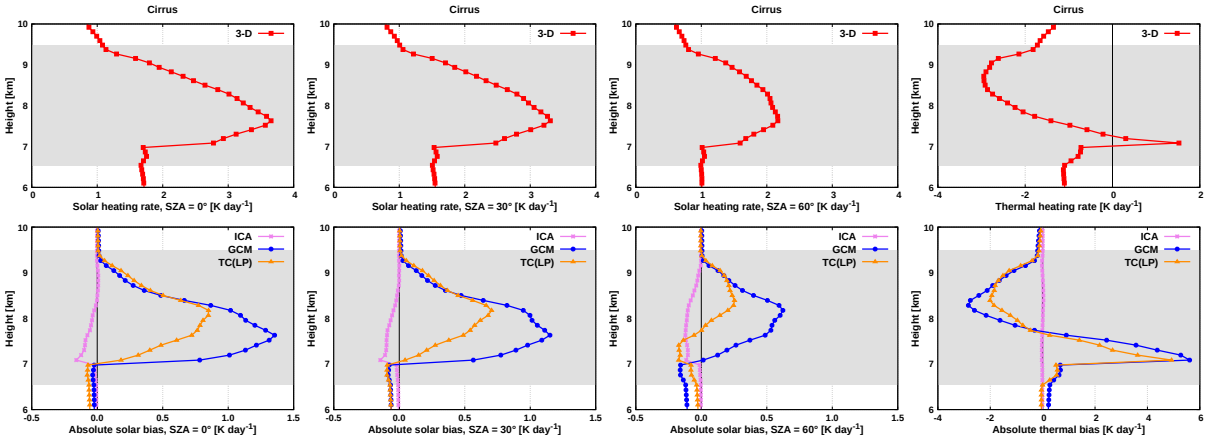

Figure 4.11: *Radiative heating rate for the cirrus cloud. The grey-shaded area denotes the cloud layer.*

In the GCM (Fig. 4.11, bottom row) the solar heating rate is overestimated by up to 1.4, 1.2 and 0.7 K day^{-1} at SZAs of 0°, 30° and 60°, respectively. The height where this maximum bias is observed corresponds with the height of maximum benchmark heating. In the thermal spectral range, the GCM bias enhances radiatively driven destabilization of the cirrus layer by an overestimation of top cooling by 2.8 K day^{-1} and a substantial overestimation of base warming (bias exceeding 5.6 K day^{-1}). The thermal GCM bias is in close agreement with that observed by Zhong et al. (2008), whereas the solar GCM bias is by a factor of 2 to 3 smaller. The latter finding indicates the potential dependence of GCM biases on the initial cloud grid resolution, which could affect the TC experiments as well and has to be more thoroughly examined in the future. The daytime GCM bias profile closely resembles that of its nighttime counterpart, such that the radiatively driven destabilization of the cirrus layer is persistently substantially escalated.

Among the various Tripleclouds experiments, the TC(LP) performs best, reducing the GCM bias in the solar, thermal and total spectral range at all SZAs (Fig. 4.13, middle). Despite that the actual IWC in each vertical layer is lognormally distributed, the TC performs best with the Gaussianity assumption. The latter implies the largest difference between the IWC pair characterizing the two cloudy regions (Fig. 3.12), partially accounting for the missing inhomogeneity provided by global FSD. Optimizations for extremely heterogeneous cases will be investigated in the next section.

Cumulonimbus

Figure 4.12 (top row) shows the radiative heating rate in the benchmark 3-D experiment for the cumulonimbus cloud. There is a strong absorption of solar radiation in the cirrus anvil, reaching a peak value of 4.4, 3.8 and 2.4 K day^{-1} at SZAs of 0°, 30° and 60°, respectively. The observed spikes in heating rate are due to the bubbling appearance of the anvil. Underneath the main absorption layer in the upper portion of the anvil, there is a shadowed region with reduced heating rate. A second, although much smaller maximum

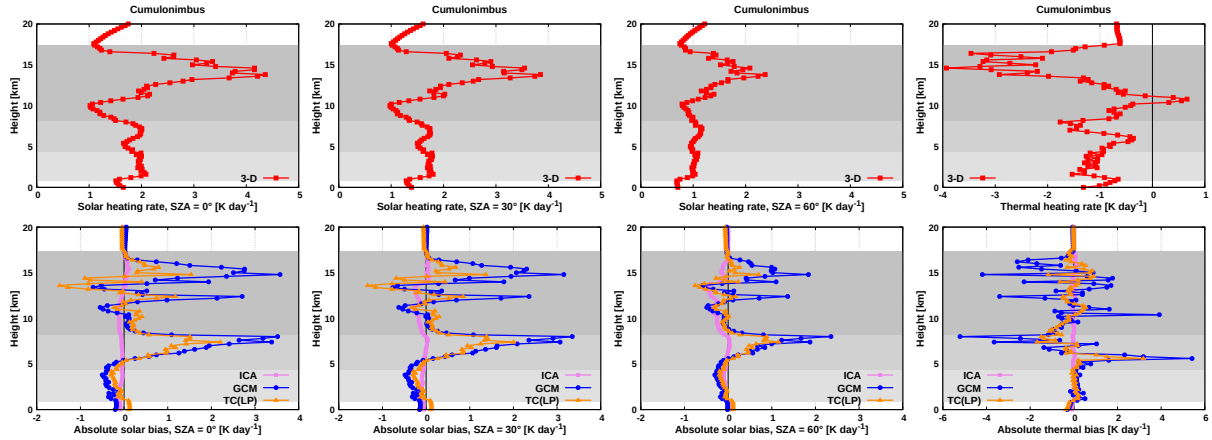

Figure 4.12: *Radiative heating rate for the cumulonimbus cloud. The grey-shaded area denotes the cloud layer. The liquid phase region is shaded light grey, the mixed-phase region is shaded middle grey and the ice phase region is shaded dark grey.*

(partially due to the aforementioned shielding effect of the anvil) of solar heating rate is observed in the mixed-phase stratiform region, followed by a third local maximum in the liquid phase region. In the thermal spectral range, there is a peak cooling of -3.9 K day^{-1} in the upper part of the anvil and a peak warming of 0.7 K day^{-1} at its bottom, driving convective destabilization within the ice layer. Similarly, a peak cooling of -1.8 K day^{-1} is observed at the top of the stratiform layer, followed by a region of locally increased heating rate at its bottom. In the liquid region the thermal profile exhibits many spikes, indicating different cloud top heights of small cumuli where cooling is maximized, followed by a region of locally increased heating rate at the uniform cumulus base height. The daytime heating rate profile is shaped by the stronger thermal radiative effect, although solar heating partially compensates thermal cooling. This solar stabilizing tendency is largest within the anvil and generally decreases with descending Sun. All in all, the three distinct maxima observed throughout the vertical extent of the present deep convective scenario are in accordance with the trimodal structure of tropical clouds (Johnson et al., 1999; Haynes and Stephens, 2007; Su et al., 2008; Fu et al., 2018).

We find that 3-D solar radiative transfer has a nonnegligible effect at all SZAs (Fig. 4.12, bottom row). In particular, heating rate differences between ICA and 3-D of about -0.5 K day^{-1} (up to -30 %) are observed at SZA of 60° and extend throughout the majority of the ice region. These differences exceed those reported by Di Giuseppe and Tompkins (2003b), which in turn surpass those previously documented by Barker et al. (1999) and Fu et al. (2000b) for solar radiation in deep convective clouds. In the underlying stratiform layer the ICA bias is comparatively small, but it increases again in the bottommost region of shallow cumuli due to their increased side area, where 3-D radiative effects are maximized. A similar picture is identified in the thermal spectral range, where the maximal ICA bias of 0.1 K day^{-1} is observed in the anvil and the cumuliform region, whereas in the stratiform layer the 3-D effect is limited.

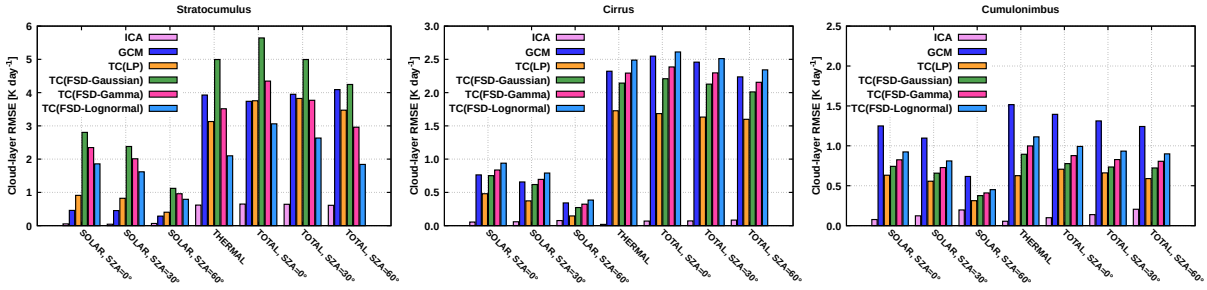

Figure 4.13: *Cloud-layer RMSE in the experiments for stratocumulus (left), cirrus (middle) and cumulonimbus (right).*

In both solar and thermal spectral range, the GCM reveals large biases within the anvil portion and even larger biases in the stratiform layer underneath (Fig. 4.12, bottom row). The latter are as expected a manifestation of considerable horizontal inhomogeneity observed in the stratiform region (recall that its actual FSD is two times larger than that of the anvil), which implies that the horizontally homogeneous cloud assumption is violated more in the stratiform region than in the anvil. If the stratiform layer had not been partially shielded by the anvil, the biases therein would be even larger. For overhead Sun, for example, we observe an overestimation of solar heating by up to 3.6 K day^{-1} in the anvil region and 3.5 K day^{-1} in the stratiform region. Thermal GCM bias of cloud top cooling up to -4.2 K day^{-1} and that of cloud base warming up to 3.9 K day^{-1} is observed within the anvil. Within the stratiform region, thermal cooling is overestimated with a bias of up to -5.2 K day^{-1} and thermal warming is overestimated by 5.4 K day^{-1} in the GCM configuration. This indicates a significant need for proper TC usage when treating deep convection.

All Tripleclouds experiments yield a significant reduction of solar, thermal and total heating rate bias when compared to conventional GCM (Fig. 4.13, right). The TC(LP) experiment performs best, generally reducing cloud-layer RMSE two- to threefold. As an illustration, thermal RMSE of 1.5 K day^{-1} is reduced to solely 0.6 K day^{-1}. Although the actual LWC and IWC are better approximated with either lognormal or gamma distribution, the assumption of Gaussianity works best in practice. The reason for this is similar as was for the cirrus case study: the actual FSD of the cumulonimbus is mostly larger than the global estimate. As the assumed Gaussianity implies the largest difference between the LWC/IWC pair, it partially accounts for the missing inhomogeneity degree introduced by global FSD. Noteworthy, within the stratiform layer (the liquid phase of which is markedly heterogeneous with FSD similar to that of the cirrus case), TC(FSD) experiments represent a considerable improvement compared to the GCM. This could be partially due to radiatively important effect of ice within the stratiform mixed-phase region: the actual FSD of ice is in close proximity to the global estimate, thus acting to reduce the overall TC error in this region.

4.2.2 Net surface flux

Shallow cumulus, stratocumulus and cumulonimbus clouds are a vital part of the planetary boundary layer, where the atmosphere is directly influenced by the presence of the Earth's surface. The net surface radiative flux is the critical component of surface energy budget and is the subject of this section. The radiative biases at the surface, stemming from the inaccurate treatment of clouds, need to be properly understood and possibly best eliminated, as they generally feed back on the biases in cloudy layers, when the radiation scheme is coupled to a dynamical model.

Cumulus

Figure 4.14 (first row) shows the net surface flux underneath the cumulus. The behavior of surface biases is partially consistent with the findings gained when examining the cloud-layer heating rate error. In the ICA the daytime net surface flux is underestimated compared to 3-D at all SZAs (maximal bias of -22 W m^{-2} or -3 % at overhead Sun). This is primarily due to well-acknowledged cloud side escape effect, where the realistic scattering of radiation through cloud side areas increases 3-D downward surface radiation. Even when the Sun is lower in the sky (SZA of 60°) this mechanism overcomes the opposing cloud side illumination effect, where an elongated surface shadow reduces the 3-D net surface flux. The strength of nocturnal surface cooling is overestimated in the ICA (bias of -4 W m^{-2} or 7 %), since realistic cloud side emission is neglected.

The daytime GCM net flux bias at comparatively high Sun (SZAs of 0° and 30°) is by a factor of 2 larger than the ICA bias. This is attributed to the fact that the horizontally homogeneous GCM cloudiness leads to an increased solar absorption and hence reduced cloud-layer transmittance. The latter reduces downward flux reaching the surface and profoundly underestimates the net flux. During nighttime, the homogeneous cloud in the GCM emits a greater amount of radiation towards the surface compared to heterogeneous cloud in the ICA, leading to a reduction of surface net flux bias.

When Tripleclouds is applied either with the LP or the FSD method instead of conventional GCM radiation scheme, the daytime net surface flux bias of -55 W m^{-2} (or -8 %) is substantially reduced to -5 W m^{-2} (or -1 %) at overhead Sun and similarly for SZA of 30° (assuming Gaussianity of cloud condensate). At SZA of 60° and especially during nighttime, radiative bias in the various TC experiments increases compared to the GCM bias. This indicates that the TC in its current configuration should be taken with caution when applied to surface thermal flux, as its usage can lead to degradation of the nocturnal surface budget compared to simple GCM model.

Stratocumulus

Figure 4.14 (second row) shows the net surface flux underneath the stratocumulus. The ICA bias is small during daytime and nighttime, maximized at overhead Sun (up to -5 W m^{-2} or -2 %). This is primarily attributed to the photon cloud side escape effect, where preferential forward scattering on cloud droplets increases 3-D downward radiation at the

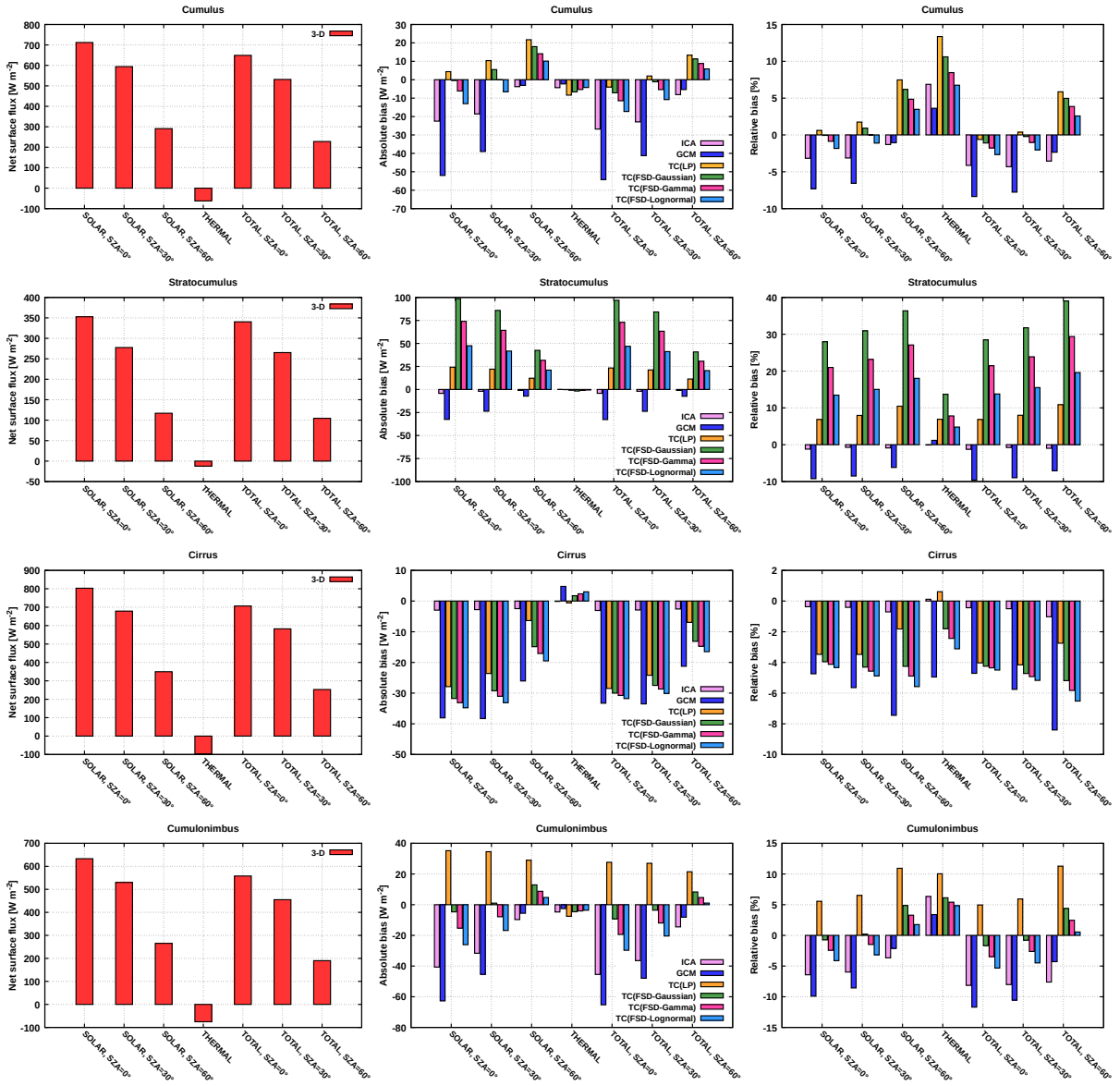

Figure 4.14: *Net surface radiative flux for cumulus (first row), stratocumulus (second row), cirrus (third row) and cumulonimbus (fourth row).*

surface. An increased solar absorption in the homogeneous GCM cloudiness implies reduced transmittance and hence underestimated daytime net surface flux. The bias is largest at overhead Sun (-33 W m^{-2} or -9 %) and decreases with increasing SZA, whereas during nighttime the GCM bias is minor.

When the TC(LP) is applied, the net flux bias is mostly slightly reduced, whereas in TC(FSD) experiments the bias is increased compared to the conventional GCM, therefore optimizations are tested in Section 4.2.3.

Cirrus

Figure 4.14 (third row) shows the net surface flux underneath the cirrus. The ICA underestimates the 3-D benchmark during daytime, primarily due to the aforementioned cloud side escape, which is prohibited in the ICA, although this phenomenon is less noticeable for optically thin cirrus (bias held below -3 W m^{-2} or -1 %). The GCM, on the contrary, reveals large biases. Whereas the absolute bias is largest at high Sun (-33 W m^{-2} at SZA of 0° and 30° during daytime), the relative bias is maximized at SZA of 60° on account of strongly reduced benchmark. Insufficient surface nighttime cooling in the GCM implies a bias of 5.5 W m^{-2} (-6 %).

All Tripleclouds experiments perform better than the GCM. The largest amelioration is observed during nighttime, where the TC(LP) practically depletes the entire bias, while TC(FSD) experiments generally halve the GCM bias. Nevertheless, alternative arrangements for better TC utilization are investigated in Section 4.2.3.

Cumulonimbus

Figure 4.14 (fourth row) shows the net surface flux underneath the cumulonimbus. The 3-D radiative effects at the surface are by far largest for the cumulonimbus case, which is a consequence of its large aspect ratio. The daytime net flux in the ICA is underestimated at all SZAs (maximal bias of -45 W m^{-2} or -8 % at overhead Sun), primarily due to the cloud side escape mechanism. The opposing 3-D effect is related to side illumination, where the effective cloud cover increases with descending Sun. This casts an elongated shadow, reducing the 3-D net flux, although for the towering cumulonimbus geometry the side escape dominates also at SZA of 60°. This extensive role of 3-D radiative transfer is consistent with the findings of Di Giuseppe and Tompkins (2005), who showed that the solar bias is an asymmetrical function of cloud cover, with the maximum attained at anvil coverage of 30$-$40 %. The majority of previous studies on deep convective systems documented smaller surface ICA bias, mostly due to a vast anvil representative of organized convection. For isolated thunderstorms or largely unorganized convection, the greater ICA bias as reported herein and previously indicated by Tompkins and Di Giuseppe (2003) is presumably more appropriate. According to Rickenbach and Rutledge (1998) such cases constituted about 50 % of all convective events observed during TOGA COARE (Webster and Lukas, 1992). The nighttime surface cooling in the ICA is stronger than in the 3-D (bias of -5 W m^{-2} or 6 %), since realistic cloud side emission increases downward radiation at the surface.

All shortcomings of the ICA manifest in the GCM as well. Nevertheless, the daytime GCM bias is even larger (-65 W m^{-2} or -12 % at overhead Sun). The horizontally homogeneous GCM cloud emits a greater radiation amount towards the surface compared to the heterogeneous cloudiness in the ICA, leading to a reduced nighttime bias.

The Tripleclouds method leads to a significantly improved daytime net flux compared to its representation in the GCM, especially in conjunction with the FSD method. In particular, the GCM bias at overhead Sun is reduced by a factor of up to 6. At SZA of 60°

the daytime GCM bias is practically entirely depleted as it is reduced by a factor of 8 when TC is applied with the lognormal assumption. The TC slightly degrades nocturnal surface budget compared to the GCM, although for the lognormal assumption this degradation is marginal (relative bias increased by 1 %).

4.2.3 Parameter optimizations

In summary, Tripleclouds in its baseline configurations proved to perform well for cumulus and the apparently most complex deep convective scenario, where it depleted the majority of GCM biases. In the case of stratocumulus and cirrus a refined TC realization is highly desired.

Optimization for overcast cloud scenarios

It was previously pointed out that in the uppermost overcast part of the stratocumulus, the actual FSD is smaller than the introduced global estimate. This might be partially attributed to the fact that overcast grid boxes do not contain cloud edges, which generally contribute to increased variability. Mixing of cloudy and cloud-free air at the edges of clouds, namely, tends to decrease the mean LWC as well as to increase the spread of LWC, both acting to increase the FSD. A grid box excluding cloud edges will therefore have lower FSD. To that end, we test the parametric FSD relationship proposed by Boutle et al. (2014), denoted as B14, for liquid cloud inhomogeneity, developed based on a rich combination of satellite, in situ and ground-based observations. This parameterization takes into account that variability is generally dependent on grid box size and cloud fraction and exhibits a discontinuity at C=1 capturing the aforementioned cloud edge effect. Thus the FSD of liquid phase for a grid box of horizontal size x [km] and cloud fraction C is given by:

$$FSD = \begin{cases} (0.45 - 0.25C)\Phi_c(x, C), & \text{if } C < 1. \\ 0.11\Phi_c(x, C), & \text{if } C = 1. \end{cases} \tag{4.1}$$

where:

$$\Phi_c(x, C) = (xC)^{1/3}\big((0.06xC)^{1.5} + 1\big)^{-0.17}.$$

Figure 4.15 shows the results of the conventional GCM calculation, Tripleclouds in its baseline lognormal configuration with the global FSD estimate (abbreviated as "G" on the graphs in the remainder of this section), as well as the corresponding refined TC experimentation where the FSD within the stratocumulus layer is parameterized according to B14. The nighttime and daytime cloud-layer RMSE (Fig. 4.15, left) in the refined TC experiment is generally slightly reduced (except at low Sun) compared to its counterpart in the baseline configuration and remains considerably lower than that in the GCM for all nighttime/daytime conditions. Most importantly, the net surface flux bias (Fig. 4.15, middle and right), which in the baseline TC setup was even larger than in the conventional GCM, is practically entirely depleted in the refined Tripleclouds venture.

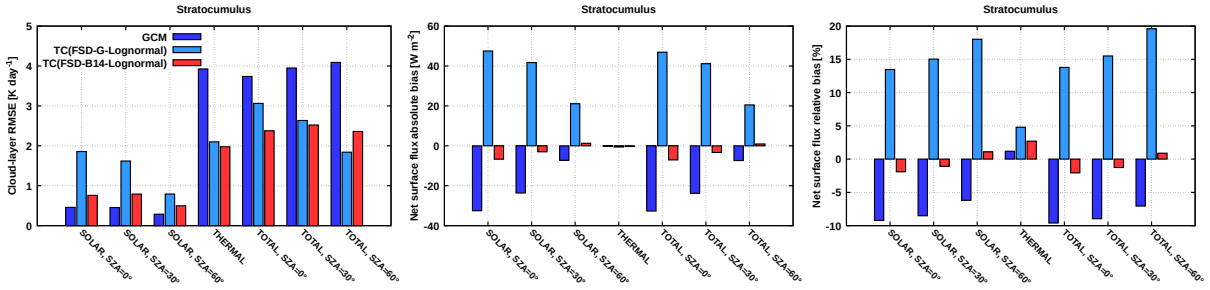

Figure 4.15: *Optimization for stratocumulus (same experiment labeling on all panels).*

Optimization for highly heterogeneous cloud scenarios

The key point worth mentioning when highly heterogeneous scenes as is the cirrus cloud are tackled with the Tripleclouds solver, is that the split percentile (SP) of 50 (geometrically halving layer cloudiness when allocating optically thin and thick portions of the cloud) is not the best choice (Hogan et al., 2019). The examination of IWC distribution in each vertical layer of the present cirrus indeed reveals that these are highly skewed (with modal value close to zero and a long tail with rarely occurring high IWC). Therefore it seems reasonable to allocate a larger portion of the cloud to the optically thinner region. This concurrently implies increasing the weighting of IWC^{cn} and decreasing the weighting of IWC^{ck}, whereby the latter is shifted to a higher value to conserve the layer mean. In order to discern the optimum geometrical partitioning of the cirrus into two parts, we carry out multiple experiments with global FSD, gradually increasing the SP from 50 to 99 (the limit of 100 coincides to the horizontally homogeneous cloud representation). Further, we aim to assess the advantage of more sophisticated FSD parameterizations. We thus evaluate the parameterization for ice cloud inhomogeneity of Hill et al. (2015) [H15], developed on the basis of CloudSat (Stephens et al., 2002, 2008) data products. All TC experiments presented in this section model the subgrid IWC distribution as lognormal.

Figure 4.16 (top row) shows the cloud-layer RMSE and net surface flux bias using TC with different FSD parameterizations for three selected splitting events, characterized by the SP of 50 (baseline), 75 and 90 (allocating 3/4 and 9/10 of layer cloudiness to the optically thinner region). For comparison the GCM experiment is shown as well. It is apparent that there is a considerable sensitivity to the choice of geometrical splitting, with the most asymmetrical split (matching the SP of 90) performing best in all cases. Noteworthy, at a given splitting event, the experiments where the FSD is parameterized according to H15 mostly lead to degraded results compared to those with global FSD (in particular at best-split scenario with SP of 90). Thus although the parameterization of H15 incorporates height dependence of horizontal variability (via cloud fraction), it underestimates the actual FSD being even smaller than the global estimate (Fig. 4.16, middle row, left), which brings the aforementioned radiative degradation. To that end, further research oriented towards advanced retrievals of high cloud inhomogeneity is firmly advocated. Vertical profiles of solar and thermal heating rate in TC experiments with global FSD for the aforementioned splitting events are further compared with the GCM

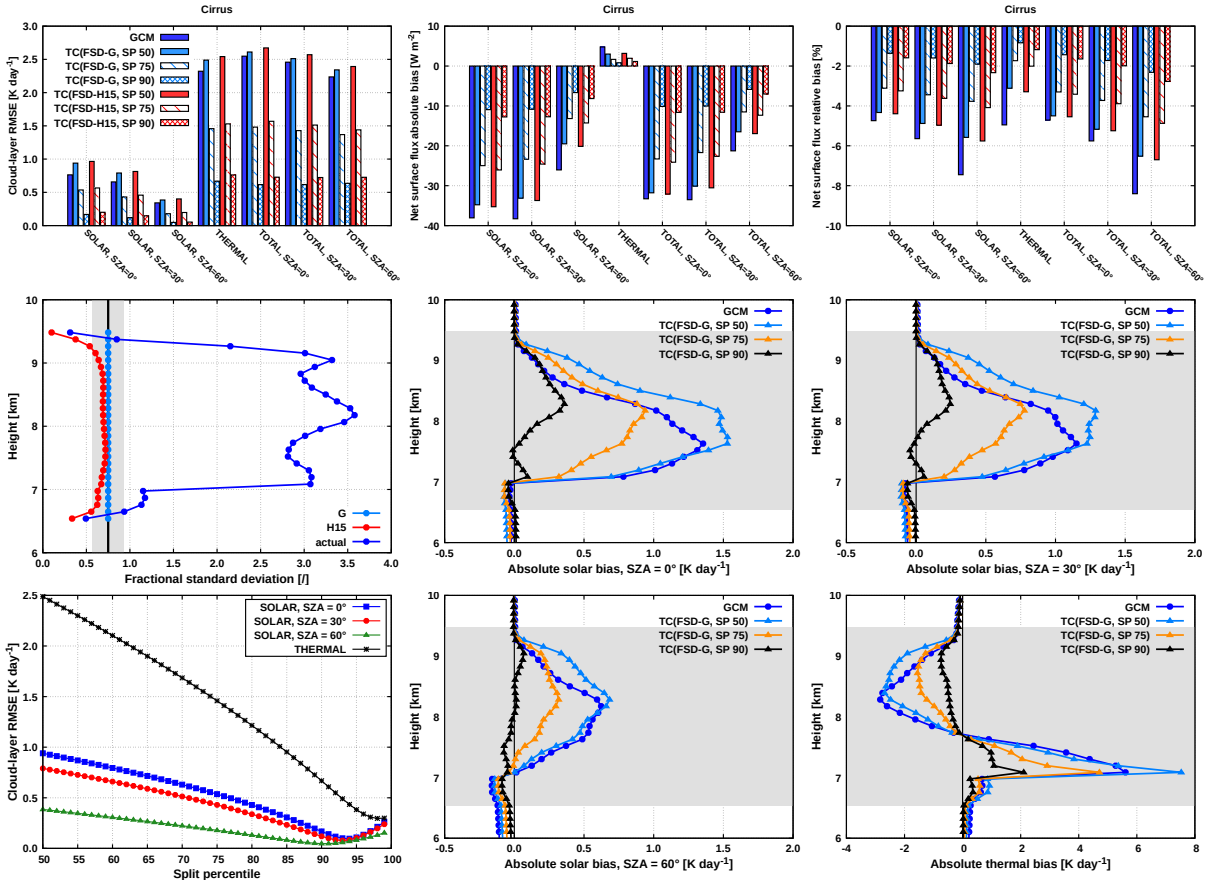

Figure 4.16: *Optimizations for cirrus (subgrid variability is modeled lognormal in all TC experiments shown).*

in Fig. 4.16. For highly asymmetrical splitting, the cloud-radiative bias throughout the majority of the cirrus layer is significantly reduced.

Finally, Fig. 4.16 (bottom left) shows the cloud-layer RMSE of TC experiments with global FSD for the entire range of splitting events. In the solar part of the spectrum, the optimum SP minimizing radiative bias indeed lies around 90 (the exact value depends on SZA). Increasing the SP beyond this optimum value degrades the heating rate in the cirrus layer. In the thermal part, on the contrary, the RMSE practically monotonically decreases as the SP is increased. Hence, the thermal RMSE exhibits a minimum when the TC is configured so that the entire layer cloudiness is attributed to the optically thinner region (horizontally homogeneous cloud representation with an effective IWC equal to IWC^{cn}). This indicates that for extremely heterogeneous scenes, as is the present cirrus, the radiation scheme employed in a weather or climate model could alternate between the Tripleclouds scheme in the solar spectral range and the computationally more efficient conventional GCM solver in the thermal spectral range, albeit with scaled IWC (effectively the traditional *scaling factor method*).

Chapter 5

Summary and Conclusions

The skillful coupling of three-dimensional heterogeneous cloud structures with the complex radiative field has long been recognized as extraordinary challenging for atmospheric scientists. This thesis took two decisive steps towards an improved treatment of unresolved cloud-radiation interaction in weather and climate models, summarized in the following paragraphs.

Quantifying the radiative bias in regional models for shallow cumulus clouds

The interaction between radiation and clouds represents a source of uncertainty in numerical weather and climate prediction due to both intrinsic constraints of 1-D radiation schemes and poor representation of unresolved clouds. The underlying question addressed in this study is how large is the bias of radiative heating rates and surface fluxes in regional (limited-area) atmospheric models for shallow cumulus clouds and how does it scale with various input parameters of radiation schemes, such as solar zenith angle, surface albedo, cloud cover and liquid water path. Further, the relative contribution of misrepresented cloud structure and neglected horizontal photon transport to the overall radiative bias was of major interest, as it has not yet been systematically quantified at regional scale. In order to tackle these queries, a set of radiative transfer calculations was carried out for a realistically evolving LES shallow cumulus cloud field, where cloud cover and cloud optical thickness increase with simulation time. For the study we extracted ten scenes with total cloud cover between ∼10 % and ∼100 %, encompassing a broad period of cumulus cloud field life cycle.

The radiative transfer experiments were conducted within the scope of comprehensive *libRadtran* radiative library. The benchmark experiment was performed on the LES highly resolved cloud field using a 3-D Monte Carlo radiation model (denoted as "3-D" experiment), which is the main advantage of the library. In order to mimic poor representation of shallow cumulus in regional numerical models, each cloud field was horizontally smeared (averaged) over boxes with dimensions comparable to regional-scale model grid spacing (several km), creating a suite of homogeneous partially cloudy layers. Subsequently, the common δ-Eddington two-stream method with maximum-random overlap assumption for

partial cloudiness was applied (denoted as "1-D" experiment), which was implemented in *libRadtran* in the framework of this dissertation. An additional experiment was conducted with the same parameter settings as 3-D, except that the Monte Carlo model was run in Independent Column Approximation mode (denoted as "ICA" experiment). In other words, the ICA experiment preserves the detailed high-resolution cloud structure and only misses horizontal photon transport, whereas the 1-D experiment misrepresents the real cloud structure and lacks horizontal photon transport as well. The comparison between 1-D and 3-D experiments was used to assess the overall bias of regional-scale model radiative quantities (focus of this study), while the comparison between ICA and 3-D experiments allowed to separate the effects of horizontal photon transport from those of cloud structure. Each trio (3-D, 1-D, ICA) of experiments was performed in both solar and thermal spectral range. Furthermore, SZA was varied from 0° to 80° with a fine angular resolution of 10°. Different values of shortwave surface albedo representing land and ocean were applied.

The vertical profile of the radiative heating rate directly influences atmospheric stratification. Systematic differences in cloud-layer heating rate were found between 1-D and 3-D experiments. In the solar experiments at higher Sun elevations (SZA less than 60°, although this depends slightly on cloud cover) as well as in the thermal experiment, the bias of the 1-D heating rate profile shows pronounced vertical gradient within the cloud layer and changes its sign approximately at the height of maximal cloud fraction. In the top part of the cloud layer (above maximal cloud fraction) the 1-D solar heating rate is too high, while in the bottom part of the cloud layer it is too low, compared to its 3-D counterpart. In the thermal spectral range the opposite is the case, but the effect is quantitatively larger and dominates the total effect of solar and thermal radiation (at all SZAs). Thus, during nighttime and daytime, the radiative bias of the 1-D heating rate enhances destabilization of the cloud layer by an overestimation of the cooling at cloud top and an overestimation of the warming at cloud bottom (a maximum bias of about -15 K day^{-1} is observed locally for fully covered cloud scenarios). The RMSE between the pair (1-D, 3-D) of heating rate profiles within the cloud layer generally increases with cloud cover, whereby this increase is approximately linear for thermal radiation. In addition, the net surface radiative flux was investigated, since it constitutes a crucial component of the surface energy budget. The daytime radiative bias at the surface is governed by the solar fluxes, where the 1-D solar net flux overestimates (underestimates) the corresponding benchmark at low (high) Sun. The overestimation at low Sun (bias up to 80 %) is largest at intermediate cloud cover, while the underestimation at high Sun (bias up to -40 %) peaks at larger cloud cover (80 % and beyond). At nighttime, the 1-D experiment overestimates the amount of benchmark surface cooling with the maximal bias of about 50 % peaked at intermediate cloud cover. Overall, the absolute bias of 1-D cloud-layer heating rate and the relative bias of 1-D net surface flux are practically insensitive to the shortwave albedo variation (land versus oceanic value). Finally, the additional dependence on liquid water path calls for further investigation, as it was strongly correlated with cloud cover in the present data set.

On the whole, the ICA experiment performs better than the 1-D experiment (with respect to the same benchmark). One can therefore conclude that resolving horizontally heterogeneous clouds leads to more accurate radiative heating rates than using overlap-

ping fractional horizontally homogeneous cloudiness even at regional scale. Since there is a long way to go before shallow cumulus clouds will be resolved within numerical weather and climate prediction, the aforementioned conclusion implies that the current development of regional model radiation schemes should go hand in hand with the development of advanced cloud schemes generating subgrid-scale cloud structure as realistically as possible. Taken together, the results of the present study hint that among most promising 1-D radiation schemes even for regional-scale modeling applications could be the McICA algorithm, the Tripleclouds method or any other approach accounting for unresolved cloud variability. Nevertheless, full solution for the multiple issues of radiation schemes and their cloud-related problems in weather and climate models remains a demanding task. This is especially true at the resolution of today's regional models, where a potential 3-D radiation parameterization should take both grid-scale and subgrid-scale radiative effects into account. This is beyond the scope of the present study, but should be perceived as a stimulator for further research on radiation-cloud interactions.

Exploring the potential of the Tripleclouds method for various cloud types

The study within the second part of this dissertation advances the conceptual understanding of radiative transfer in shallow cumulus, marine stratocumulus, midlatitude cirrus and tropical deep convective clouds. The focus is laid on the issues related to misrepresentation of cloud horizontal inhomogeneity in coarse-resolution (large-scale) atmospheric weather and climate models, which are tackled with the aid of the Tripleclouds (TC) radiative solver. The Tripleclouds method, primarily introduced by Shonk and Hogan (2008), is an approach which accounts for horizontal cloud inhomogeneity by using two regions in each vertical model layer to represent the cloud (as opposed to one, which is the convention of traditional cloud models). One of these regions is used to represent the optically thicker part of the cloud, whereas the other region represents the remaining optically thinner part. The challenge is to optimally set the pair of liquid/ice water content characterizing the two cloudy regions and geometrically split the layer cloudiness in the corresponding two parts. The answer to this research question is crucially dependent on the properties of subgrid cloud horizontal variability, characterized by the fractional standard deviation (FSD) of cloud condensate and the shape of its distribution. Since this information is generally not available within a large-scale numerical model (or, if it is, it might be poorly estimated), Shonk et al. (2010) derived a global estimate of FSD on the basis of multiple observational studies. The primary objective of the present study was to test the validity of the global FSD estimate in conjunction with different assumptions for subgrid cloud condensate distribution, which are commonly applied in models (Gaussian, gamma and lognormal). The Tripleclouds concept was incorporated into the efficient δ-Eddington two-stream radiation scheme and was used herein to answer these questions within the scope of *libRadtran* radiative software. For our study we chose four intrinsically contrasting cloud types generated by different cloud models, which should reflect diverse cloud conditions occurring globally. These high-resolution cloud field data allow to gain important insights about small-scale cloud variability and give the opportunity to compare the actual modeled variability with

the global estimate or other existing parameterizations. For each cloud type, various TC experiments were evaluated against a 3-D benchmark radiation calculation. These results were compared with the conventional GCM calculation utilizing homogeneous layer cloudiness, which can be viewed as the upper bound for the tolerable TC error. Moreover, the ICA approximation was compared with the 3-D benchmark to quantify the bias related to neglected horizontal photon transport. A systematic investigation of radiative biases of cloud-layer heating rate and net surface flux was provided for each selected cloud case. These biases were examined in the solar and thermal part of the spectrum, and in the solar spectral range additionally as a function of solar zenith angle.

It was found that in the majority of applications, the ICA is significantly more accurate than the conventional GCM experiment, indicating a large potential for Tripleclouds, which reduces the bias related to unresolved cloud structure, but not to horizontal photon transport. Regarding the optimal TC configuration, which aims to minimize radiative biases, the exact conclusions drawn depend on each particular cloud type case study. In general, the simplest TC arrangement using a globally constant FSD parameter and geometrically halving the layer cloudiness, worked best for the shallow cumulus and the apparently most complex deep convective scenario. In the case of stratocumulus and cirrus, an improved TC performance was highly desired. To that end, the second objective of the present study was to assess recent advanced FSD parameterizations, characterizing systematic departures from global mean cloud variability observed for liquid and ice phase. For the stratocumulus cloud, an optimization in terms of a parametric FSD relationship portraying reduced horizontal variability at overcast conditions lead to a substantially improved TC realization. For extremely heterogeneous cirrus case, on the other hand, allocating the greater portion to the optically thinner part of the cloud (e.g., approximately 9/10 of layer cloudiness in the solar part of the spectrum), proved to be of crucial importance in the TC settings, eliminating the vast majority of GCM biases. All in all, these findings are in support of cloud-regime dependent approaches, which ought to be further boosted to be used in radiation schemes of next-generation atmospheric models. Whereas current GCMs do not explicitly predict cloud meteorological regimes (i.e., whether model cloudiness appears in the form of cumulus or stratocumulus), they have the ability to diagnose cloud type based on temperature and humidity fields (Norris, 1998). An alternative is to consider the physical processes responsible for cloud formation as imprinted in the parameterization schemes activated to generate cloudiness within a model grid box (e.g., shallow convection as opposed to large-scale saturation). We thereby propose that the TC configuration should be adequately adjusted according to cloud type. To that end, this pilot study exposing the potential of the Tripleclouds method for four essential, yet fundamentally different cloud types demonstrates the feasibility of a full-scale research project investigating a broad spectrum of cloud morphology, cloud inhomogeneity, cloud cover and optical thickness. Some ideas on how to extend the present study in the light of these conclusions are outlined in the next chapter.

Chapter 6

Outlook

Extension of the present Tripleclouds study to a broad cloud data spectrum

The acquired physical understanding of radiative biases, in particular those stemming from neglected cloud horizontal heterogeneity, for four fundamentally contrasting cloud case studies as highlighted in this work, is a necessary first step for properly setting the Tripleclouds parameters in its possible future operational usage. A more comprehensive documentation of radiative biases, however, would necessitate the examination of the full parameter space of in-cloud horizontal variability and cloud geometry. As an illustration, the first part of this dissertation investigated the radiative transfer for an evolving shallow cumulus cloud field and showed that radiative biases depend on the stage of cloud field life cycle (which can be to a first approximation characterized in terms of cloud cover). Although this part examined radiative biases at the resolution of regional atmospheric models, similar problematics is expected at coarser resolution of larger-scale models as well. The question that therefore needs to be addressed next is to what extent do our Tripleclouds findings for a particular cloud type case study apply to a larger set of the same cloud type scenarios comprising a wide range of cloud cover. This question is relevant, because horizontal variability essentially depends on cloud fraction. Similarly, the degree of cloud horizontal variability might depend on the GCM grid resolution, which has to be investigated in more detail in the future. More specific suggestions on how to expand the present Tripleclouds research to a wider scope of cloud data are outlined in subsequent paragraphs.

Organizational aspects of shallow convection

Organizational aspects of shallow convection should be further addressed in the context of the present study. Mesoscale shallow convection sometimes occurs in the form of uniformly scattered cumuli, but is also frequently organized into cloud streets, clusters or mesoscale arcs (Agee et al., 1973; Atkinson and Zhang, 1996; Wood and Hartmann, 2006; Seifert and Heus, 2013). The robustness of the present results on the nature of cloud organization should be examined next. Recently, Stevens et al. (2019) proposed four mesoscale cloud patterns frequently observed in trade wind regions, which they labeled “Sugar”, “Flower”,

"Fish" and "Gravel". A follow-up study of Rasp et al. (2019) proved that the four patterns correspond to physically meaningful cloud regimes, each of them being associated with specific large-scale environmental conditions. These climatologically distinct environments should exhibit a highly variable cloud water variance. If this proves true and if the internal cloud variability is properly quantified, a regime-dependent fractional standard deviation could be passed into the Tripleclouds scheme in the next generation of global models.

Stratocumulus-to-cumulus transition in clean and polluted environments

A natural extension of the present study similarly appears to be the examination of the full ASTEX data set. The transition from solid stratocumulus to trade cumulus or *stratocumulus breakup* (Albrecht et al., 1995a,b; Bretherton and Wyant, 1997) seems appealing to study with Tripleclouds, since it is often associated with increased horizontal heterogeneity (Wang and Lenschow, 1995; Wood and Hartmann, 2006; Wood, 2012). Whereas in the current study a single stratocumulus was investigated, the future work should distinguish between clean (marine) and polluted (continental) cases. For the ASTEX field experiment (Albrecht et al., 1995a), namely, substantial variations in clear and polluted air masses were reported, which affected both cloud properties and drizzle. These topics are of interest to the author of this dissertation and will be addressed in forthcoming study.

Vertical overlap generalization

In order to carry out the analysis for clouds of large vertical growth, such as deep convective clouds, in a strongly sheared environment, the present vertical overlap rules have to be generalized (Fig. 6.1). Finally, if the subgrid-scale horizontal photon transport is to be accounted for in a more sophisticated manner, the two-stream equations need to be extended to include terms representing in-layer horizontal radiative energy exchange between the cloud and the cloud-free part of the grid box as well as that between the optically thicker and thinner parts of the cloud. Some of these issues are currently investigated by the author of this dissertation and will be discussed in detail in upcoming studies as well.

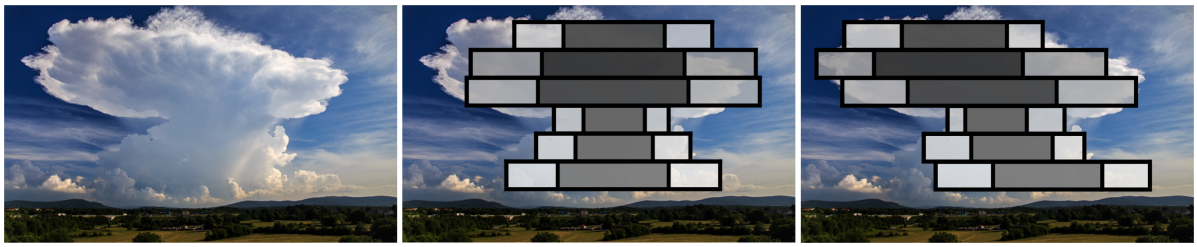

Figure 6.1: *Vertical overlap generalization challenge: the present Tripleclouds implementation (middle panel) and desired generalized form (right panel).*

Appendix A

Analytical probability density functions

In the following we outline the relationship between $\overline{LWC}$, the fractional standard deviation of LWC (herein denoted as f_{LWC}) and the parameters used to describe lognormal and gamma distributions, which were applied to fit the actual LWC distributions.

A.1 Lognormal distribution

A lognormal distribution of LWC is defined as:

$$p(LWC) = \frac{1}{\sqrt{2\pi}\sigma_0 LWC} \exp\left[- \frac{\ln(LWC/LWC_0)^2}{2\sigma_0^2} \right]. \tag{A.1}$$

The parameters of the lognormal distribution, LWC_0 and σ_0, can be defined in terms of $\overline{LWC}$ and f_{LWC} in the following fashion:

$$LWC_0 = \frac{\overline{LWC}}{\sqrt{f_{LWC} + 1}}, \tag{A.2}$$

$$\sigma_0^2 = \ln(f_{LWC} + 1). \tag{A.3}$$

A.2 Gamma distribution

A gamma distribution of LWC is defined as:

$$p(LWC) = \frac{1}{\Gamma(\nu)} \left(\frac{\nu}{\overline{LWC}} \right)^{\nu} LWC^{\nu-1} \exp\left[-\frac{\nu LWC}{\overline{LWC}} \right], \tag{A.4}$$

where $\Gamma(\nu)$ denotes the gamma function and the parameter of the distribution ν is related to f_{LWC} as follows:

$$\nu = \left(\frac{1}{f_{LWC}}\right)^2. \tag{A.5}$$

Appendix B

Technical instructions for *libRadtran* users

The *libRadtran* radiative transfer package is still under steady, continuous development. The latter goes hand in hand, inter alia, with its plenty satisfied users worldwide. The core of the *libRadtran* package is the *uvspec* radiative transfer model, which contains several radiative transfer equation (RTE) solvers. To promote the usage of both recently implemented two-stream solvers (termed "`twomaxrnd`" and "`twomaxrnd3C`"; Fig. B.1), which are coded in C programming language, basic guidelines are given below. For a complete description on how to set up the background atmosphere and other input parameters, the reader is referred to the *libRadtran* user manual, which is included in the software package. The output quantities of both algorithms include either radiative fluxes (default) [W m^{-2}] or heating rates [K day^{-1}]. Whereas the examples provided below illustrate the treatment of water clouds, both RTE solvers can be applied to ice clouds in a similar fashion.

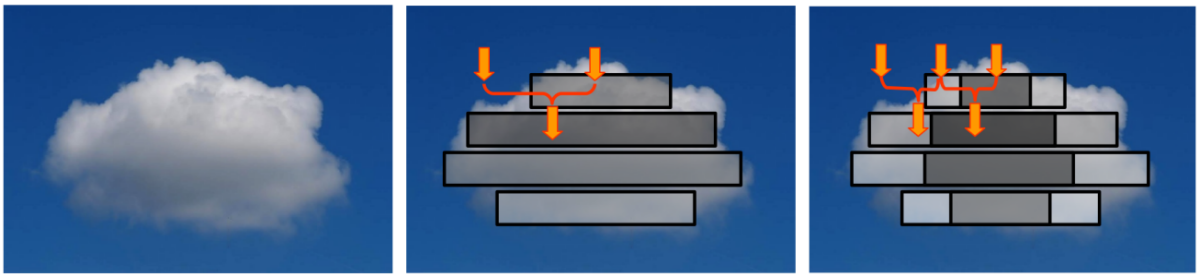

Figure B.1: *Illustrating the RTE solvers "twomaxrnd" (middle panel) and "twomaxrnd3C" (right panel).*

B.1 RTE solver: "twomaxrnd"

The δ-Eddington two-stream method with maximum-random overlap assumption for partial cloudiness, in the configuration as documented in Section 3.2.2, is called as follows:

```
rte_solver twomaxrnd
cloud_fraction_file cf.dat
wc_file 1D wc.dat
```

where `cf.dat` is the standard *libRadtran* file containing cloud fraction vertical profile and `wc.dat` is the standard 1-D file defining water cloud properties.

B.2 RTE solver: "twomaxrnd3C"

The Tripleclouds radiative solver, effectively the δ-Eddington two-stream method for one cloud-free and two cloudy regions at each height with maximum^2-random overlap assumption, as described in Section 3.2.3, is invoked as follows:

```
rte_solver twomaxrnd3C
cloud_fraction_file cf.dat
twomaxrnd3C_scale_cf 0.4
profile_file wck 1D wck.dat
profile_file wcn 1D wcn.dat
```

where `cf.dat` is again the standard file containing the vertical profile of cloud fraction. It is important to note that this file determines the cloud fraction of the entire layer cloudiness (sum of optically thick and thin cloudy regions). The division of the latter into two components is managed via newly introduced parameter `twomaxrnd3C_scale_cf`, which corresponds to the parameter α in Eqs. 3.32 and 3.33. The split of averaged cloud water properties into two components is not yet automated; rather, the user is asked to preprocess both cloud files depending on his/her specific needs. The resulting `wck.dat` and `wcn.dat` are 1-D water cloud files, defining properties of optically thick and thin cloudy regions, respectively (note that the option `profile_file` is solely the generalization of the `wc_file` command).

Appendix C

List of abbreviations

1-D	One-Dimensional
2-D	Two-Dimensional
3-D	Three-Dimensional
A	Albedo
ALADIN-SI	Regional Numerical Weather Prediction model of Slovenian Meteorological Service
ARPEGE	Global Numerical Weather Prediction model of French Meteorological Service
ASTEX	Atlantic Stratocumulus Transition Experiment
CC	Cloud Cover
COSMO	Consortium for Small-scale Modeling
COSMO-D2	Regional Numerical Weather Prediction model of German Meteorological Service (current version)
COSMO-DE	Regional Numerical Weather Prediction model of German Meteorological Service (former version)
CRM	Cloud Resolving Model
ECMWF	European Centre for Medium-Range Weather Forecasts
ECMWF-IFS	The ECMWF Integrated Forecast System
ECHAM5	Atmospheric General Circulation Model developed at the Max Planck Institute for Meteorology, version 5
ENS	ENSemble atmospheric model of ECMWF-IFS
FSD	Fractional Standard Deviation
GCE-CRM	Goddard Cumulus Ensemble Cloud Resolving Model
GCM	General Circulation Model
GFS	Global Forecast System
GEM	Global Environmental Multiscale model
HRES	High RESolution atmospheric model of ECMWF-IFS
I3RC	Intercomparison of 3-D Radiation Codes
ICA	Independent Column Approximation
ICRCCM	Intercomparison of Radiation Codes in Climate Models

ICON	ICOsahedral Nonhydrostatic model
IWC	Ice Water Content
IWP	Ice Water Path
LES	Large Eddy Simulation
LP	Lower Percentile
LSAM	Large-Scale Atmospheric Model
LWC	Liquid Water Content
LWP	Liquid Water Path
McICA	Monte Carlo integration of Independent Column Approximation
MYSTIC	Monte Carlo code for the phYSically correct Tracing of photons In Cloudy atmospheres
NWP	Numerical Weather Prediction
PDF	Probability Density Function
RH	Relative Humidity
RICO	Rain In Cumulus over the Ocean
RMSE	Root Mean Square Error
RRTMG	Rapid Radiative Transfer Model for GCMs
RT	Radiative Transfer
RTE	Radiative Transfer Equation
SHDOM	Spherical Harmonic Discrete Ordinate Method
SP	Split Percentile
STBL	Stratocumulus-Topped Boundary Layer
SZA	Solar Zenith Angle
TC	TripleClouds
TOA	Top Of Atmosphere
TOGA COARE	Tropical Ocean-Global Atmosphere program, Coupled Ocean-Atmosphere Response Experiment
TRMM-LBA	Tropical Rainfall Measuring Mission Large-Scale Biosphere-Atmosphere Experiment in Amazonia
TSM	Two-Stream Method
UCLA-LES	University of California, Los Angeles Large Eddy Simulation model
UKMO	United Kingdom Meteorological Office
UTLS	Upper Troposphere and Lower Stratosphere

Bibliography

Agee, E. M., Chen, T. S., and Dowell, K. E. (1973). A review of mesoscale cellular convection. *Bull. Am. Meteorol. Soc.*, **54** (**10**), 1004–1012, doi: 10.1175/1520-0477(1973)054⟨1004:AROMCC⟩2.0.CO;2.

Ahlgrimm, M. and Forbes, R. M. (2016). Regime dependence of cloud condensate variability observed at the Atmospheric Radiation Measurement Sites. *Q. J. R. Meteorol. Soc.*, **142** (**697**), 1605–1617, doi: 10.1002/qj.2783.

Ahlgrimm, M. and Forbes, R. M. (2017). Regime dependence of ice cloud heterogeneity – a convective life-cycle effect? *Q. J. R. Meteorol. Soc.*, **143** (**709**), 3259–3268, doi: 10.1002/qj.3178.

Albrecht, B. A., Randall, D. A., and Nicholls, S. (1988). Observations of marine stratocumulus clouds during FIRE. *Bull. Am. Meteorol. Soc.*, **69** (**6**), 618–626, doi: 10.1175/1520-0477(1988)069⟨0618:OOMSCD⟩2.0.CO;2.

Albrecht, B. A., Bretherton, C. S., Johnson, D., Scubert, W. H., and Frisch, A. S. (1995a). The Atlantic Stratocumulus Transition Experiment – ASTEX. *Bull. Am. Meteorol. Soc.*, **76** (**6**), 889–904, doi: 10.1175/1520-0477(1995)076⟨0889:TASTE⟩2.0.CO;2.

Albrecht, B. A., Jensen, M. P., and Syrett, W. J. (1995b). Marine boundary layer structure and fractional cloudiness. *J. Geophys. Res.*, **100** (**D7**), 14209–14222, doi: 10.1029/95JD00827.

Anderson, G., Clough, S., Kneizys, F., Chetwynd, J., and Shettle, E. (1986). AFGL Atmospheric Constituent Profiles (0-120 km). *Tech. Rep. AFGL-TR-86-0110, AFGL (OPI), Hanscom AFB, MA 01736.*

Arabas, S., Pawlowska, H., and Grabowski, W. W. (2009). Effective radius and droplet spectral width from in-situ aircraft observations in trade-wind cumuli during RICO. *Geophys. Res. Lett.*, **36** (**11**), doi: 10.1029/2009GL038257.

Arakawa, A. (2004). The cumulus parameterization problem: Past, present, and future. *J. Climate*, **17** (**13**), 2493–2525, doi: 10.1175/1520-0442(2004)017⟨2493:RATCPP⟩2.0.CO;2.

Atkinson, B. W. and Zhang, J. W. (1996). Mesoscale shallow convection in the atmosphere. *Rev. Geophys.*, **34** (**4**), 403–431, doi: 10.1029/96RG02623.

Austin, P. H., Baker, M. B., Blyth, A. M., and Jensen, J. B. (1985). Small-scale variability in warm continental cumulus clouds. *J. Atmos. Sci.*, **42** (**11**), 1123–1138, doi: 10.1175/1520-0469(1985)042⟨1123:SSVIWC⟩2.0.CO;2.

Barker, H. W. (2008). Overlap of fractional cloud for radiation calculations in GCMs: A global analysis using CloudSat and CALIPSO data. *J. Geophys. Res.*, **113** (**D8**), doi: 10.1029/2007JD009677.

Barker, H. W., Wielicki, B. A., and Parker, L. (1996). A parameterization for computing grid-averaged solar fluxes for inhomogeneous marine boundary layer clouds. Part II: Validation using satellite data. *J. Atmos. Sci.*, **53** (**16**), 2304–2316, doi: 10.1175/1520-0469(1996)053⟨2304:APFCGA⟩2.0.CO;2.

Barker, H. W., Stephens, G. L., and Fu, Q. (1999). The sensitivity of domain averaged solar fluxes to assumptions about cloud geometry. *Q. J. R. Meteorol. Soc.*, **125** (**558**), 2127–2152, doi: 10.1002/qj.49712555810.

Barker, H. W., Pincus, R., and Morcrette, J.-J. (2002). The Monte Carlo Independent Column Approximation: Application within large-scale models. *Extended Abstracts, GCSS-ARM Workshop on the representation of cloud systems in large-scale models, Kananaskis, Canada*, pages 1–10.

Barker, H. W. et al. (2003). Assessing 1D atmospheric solar radiative transfer models: Interpretation and handling of unresolved clouds. *J. Climate*, **16** (**16**), 2676–2699, doi: 10.1175/1520-0442(2003)016⟨2676:ADASRT⟩2.0.CO;2.

Bauer, P., Thorpe, A., and Brunet, G. (2015). The quiet revolution of numerical weather prediction. *Nature*, **525** (**7567**), 47–55, doi: doi:10.1038/nature14956.

Baur, F., Keil, C., and Craig, G. C. (2018). Soil moisture–precipitation coupling over Central Europe: Interactions between surface anomalies at different scales and the dynamical implication. *Q. J. R. Meteorol. Soc.*, **144** (**717**), 2863–2875, doi: 10.1002/qj.3415.

Bergman, J. W. and Rasch, P. J. (2002). Parameterizing vertically coherent cloud distributions. *J. Atmos. Sci.*, **59** (**14**), 2165–2182, doi: 10.1175/1520-0469(2002)059⟨2165:PVCCD⟩2.0.CO;2.

Blyth, A. and Latham, J. (1991). A climatological parameterization for cumulus clouds. *J. Atmos. Sci.*, **48** (**21**), 2367–2372, doi: 10.1175/1520-0469(1991)048⟨2367:ACPFCC⟩2.0.CO;2.

Bony, S. and Emanuel, K. A. (2001). A Parameterization of the cloudiness associated with cumulus convection; Evaluation using TOGA COARE data. *J. Atmos. Sci.*, **58** (**21**), 3158–3183, doi: 10.1175/1520-0469(2001)058⟨3158:APOTCA⟩2.0.CO;2.

Bony, S., Stevens, B., Frierson, D. M. W., Jakob, C., Kageyama, M., Pincus, R., Shepherd, T. G., Sherwood, S. C., Siebesma, A. P., Sobel, A. H., Watanabe, M., and Webb., M. J. (2015). Clouds, circulation and climate sensitivity. *Nature Geoscience*, **8** (**4**), 261–268, doi: 10.1038/ngeo2398.

Boucher, O. et al. *Clouds and aerosols*. In: Climate Change 2013: The Physical Science Basis. Contribution of Working Group I to the Fifth Assessment Report of the Intergovernmental Panel on Climate Change. Cambridge University Press, Cambridge, UK, (2013), doi: 10.1017/CBO9781107415324.016.

Boutle, I. A., Abel, S. J., Hill, P. G., and Morcrette, C. J. (2014). Spatial variability of liquid cloud and rain: Observations and microphysical effects. *Q. J. R. Meteorol. Soc.*, **140** (**679**), 583–594, doi: 10.1002/qj.2140.

Brenguier, J.-L., Pawlowska, H., Schüller, L., Preusker, R., Fischer, J., and Fouquart, Y. (2000). Radiative properties of boundary layer clouds: Droplet effective radius versus number concentration. *J. Atmos. Sci.*, **57** (**6**), 803–821, doi: 10.1175/1520-0469(2000)057⟨0803:RPOBLC⟩2.0.CO;2.

Bretherton, C. S. and Khairoutdinov, M. F. (2015). Convective self-aggregation feedbacks in near-global cloud-resolving simulations of an aquaplanet. *J. Adv. Model. Earth Syst.*, **7** (**4**), 1765–1787, doi: 10.1002/2015MS000499.

Bretherton, C. S. and Wyant, M. C. (1997). Moisture transport, lower-tropospheric stability, and decoupling of cloud-topped boundary layers. *J. Atmos. Sci.*, **54** (**1**), 148–167, doi: 10.1175/1520-0469(1997)054⟨0148:MTLTSA⟩2.0.CO;2.

Bugliaro, L., Zinner, T., Keil, C., Mayer, B., Hollmann, R., Reuter, M., and Thomas, W. (2011). Validation of cloud property retrievals with simulated satellite radiances: A case study for SEVIRI. *Atmos. Chem. Phys.*, **11** (**12**), 5603–5624, doi: 10.5194/acp-11-5603-2011.

Cahalan, R. F., Ridgway, W., Wiscombe, W. J., Bell, T. L., and Snider, J. B. (1994a). The albedo of fractal stratocumulus clouds. *J. Atmos. Sci.*, **51** (**16**), 2434–2455, doi: 10.1175/1520-0469(1994)051⟨2434:TAOFSC⟩2.0.CO;2.

Cahalan, R. F., Ridgway, W., Wiscombe, W. J., Gollmer, S., and Harshvardhan. (1994b). Independent pixel and Monte Carlo estimates of stratocumulus albedo. *J. Atmos. Sci.*, **51** (**24**), 3776–3790, doi: 10.1175/1520-0469(1994)051⟨3776:IPAMCE⟩2.0.CO;2.

Cahalan, R. F., Silberstein, D., and Snider, J. B. (1995). Liquid water path and plane-parallel albedo bias during ASTEX. *J. Atmos. Sci.*, **52** (**16**), 3002–3012, doi: 10.1175/1520-0469(1995)052⟨3002:LWPAPP⟩2.0.CO;2.

Cahalan, R. F. et al. (2005). The I3RC: Bringing together the most advanced radiative transfer tools for cloudy atmospheres. *Bull. Am. Meteorol. Soc.*, **86** (**9**), 1275–1294, doi: 10.1175/BAMS-86-9-1275.

Cairns, B., Lacis, A. A., and Carlson, B. E. (2000). Absorption within inhomogeneous clouds and its parameterization in general circulation models. *J. Atmos. Sci.*, **57** (**5**), 700–714, doi: 10.1175/1520-0469(2000)057⟨0700:AWICAI⟩2.0.CO;2.

Carlin, B., Fu, Q., Lohmann, H., Mace, G. G., Sassen, K., and Comstock, J. M. (2002). High-cloud horizontal inhomogeneity and solar albedo bias. *J. Climate*, **15** (**17**), 2321–2339, doi: 10.1175/1520-0442(2002)015⟨2321:HCHIAS⟩2.0.CO;2.

Chandrasekhar, S. *Radiative transfer*. Oxford University Press, (1950).

Chen, T., Rossow, W. B., and Zhang, Y.-C. (2000). Radiative effects of cloud-type variations. *J. Climate*, **13** (**1**), 264–286, doi: 10.1175/1520-0442(2000)013⟨0264:REOCTV⟩2.0.CO;2.

Childs, H., Brugger, E., Whitlock, B., Meredith, J., Ahern, S., and Pugmire, D. (2012). VisIt: An end-user tool for visualizing and analyzing very large data. *In: High-performance visualization-enabling extreme-scale scientific insight*, pages 357–372.

Conover, J. W. *Practical nonparametric statistics*. John Wiley & Sons, New York, USA, (1971).

Craig, G. et al. (2010). Weather Research in Europe. A THORPEX European Plan. *WMO/TD-No. 1513, WWRP/THORPEX No. 14.*

Črnivec, N. and Mayer, B. (2019). Quantifying the bias of radiative heating rates in numerical weather prediction models for shallow cumulus clouds. *Atmos. Chem. Phys.*, **19** (**12**), 8083–8100, doi: 10.5194/acp-19-8083-2019.

Črnivec, N. and Mayer, B. (2020a). The incorporation of the Tripleclouds concept into the δ-Eddington two-stream radiation scheme: solver characterization and its application to shallow cumulus clouds. *Atmos. Chem. Phys.*, **20** (**17**), 10733–10755, doi: 10.5194/acp-20-10733-2020.

Črnivec, N. and Mayer, B. (2020b). Towards improved treatment of cloud-radiation interaction in weather and climate models: exploring the potential of the Tripleclouds method for various cloud types. *Geosci. Model Dev., in review.*

Davies, R. (1978). The effect of finite geometry on the three-dimensional transfer of solar irradiance in clouds. *J. Atmos. Sci.*, **35** (**9**), 1712–1725, doi: 10.1175/1520-0469(1978)035⟨1712:TEOFGO⟩2.0.CO;2.

Deardorff, J. W. (1981). On the distribution of mean radiative cooling at the top of a stratocumulus-capped mixed layer. *Q. J. R. Meteorol. Soc.*, **107** (**451**), 191–202, doi: 10.1002/qj.49710745112.

Di Giuseppe, F. and Tompkins, A. M. (2003a). Effect of spatial organization on solar radiative transfer in three-dimensional idealized stratocumulus cloud fields. *J. Atmos. Sci.*, **60** (**15**), 1774–1794, doi: 10.1175/1520-0469(2003)060⟨1774:EOSOOS⟩2.0.CO;2.

Di Giuseppe, F. and Tompkins, A. M. (2003b). Three-dimensional radiative transfer in tropical deep convective clouds. *J. Geophys. Res.*, **108** (**D23**), 4741–4756, doi: 10.1029/2003JD003392.

Di Giuseppe, F. and Tompkins, A. M. (2005). Impact of cloud cover on solar radiative biases in deep convective regimes. *J. Atmos. Sci.*, **62** (**6**), 1989–2000, doi: 10.1175/JAS3442.1.

Di Giuseppe, F. and Tompkins, A. M. (2015). Generalizing cloud overlap treatment to include the effect of wind shear. *J. Atmos. Sci.*, **72** (**8**), 2865–2876, doi: 10.1175/JAS-D-14-0277.1.

Edwards, J. M. and Slingo, A. (1996). Studies with a flexible new radiation code. I: Choosing a configuration for a large-scale model. *Q. J. R. Meteorol. Soc.*, **122** (**531**), 689–719, doi: 10.1002/qj.49712253107.

Emde, C. and Mayer, B. (2007). Simulation of solar radiation during a total eclipse: A challenge for radiative transfer. *Atmos. Chem. Phys.*, **7** (**9**), 2259–2270, doi: 10.5194/acp-7-2259-2007.

Emde, C. et al. (2016). The libRadtran software package for radiative transfer calculations (version 2.0.1). *Geosci. Model Dev.*, **9** (**5**), 1647–1672, doi: 10.5194/gmd-9-1647-2016.

Evans, K. F. (1998). The spherical harmonics discrete ordinate method for three-dimensional atmospheric radiative transfer. *J. Atmos. Sci*, **55** (**3**), 429–446, doi: 10.1175/1520-0469(1998)055⟨0429:TSHDOM⟩2.0.CO;2.

Evans, K. F. and Wiscombe, W. (2004). An algorithm for generating stochastic cloud fields from radar profile statistics. *Atmos. Res.*, **72**, 263–289, doi: 10.1016/j.atmosres.2004.03.016.

Ewald, F. *Retrieval of vertical profiles of cloud droplet effective radius using solar reflectance from cloud sides.* PhD thesis, Ludwig-Maximilians-Universität München, (2016).

Fauchez, T., Cornet, C., Szczap, F., Dubuisson, P., and Rosambert, T. (2014). Impact of cirrus clouds heterogeneities on top-of-atmosphere thermal infrared radiation. *Atmos. Chem. Phys.*, **14** (**11**), 5599–5615, doi: 10.5194/acp-14-5599-2014.

Forster, L. *Information content of halo displays for remote sensing of ice crystal properties.* PhD thesis, Ludwig-Maximilians-Universität München, (2017).

Fu, Q., Carlin, B., and Mace, G. (2000a). Cirrus horizontal inhomogeneity and OLR bias. *Geophys. Res. Lett.*, **27** (**20**), 3341–3344, doi: 10.1029/2000GL011944.

Fu, Q., Cribb, M. C., Barker, H. W., Krueger, S. K., and Grossman, A. (2000b). Cloud geometry effects on atmospheric solar absorption. *J. Atmos. Sci.*, **57** (**8**), 1156–1168, doi: 10.1175/1520-0469(2000)057⟨1156:CGEOAS⟩2.0.CO;2.

Fu, Q., Smith, M., and Yang, Q. (2018). The impact of cloud radiative effects on the tropical tropopause layer temperatures. *Atmosphere*, **9** (**10**), 377, doi: 10.3390/atmos910037.

Fu, Q. and Liou, K. N. (1992). On the correlated k-distribution method for radiative transfer in nonhomogeneous atmospheres. *J. Atmos. Sci.*, **49** (**22**), 2139–2156, doi: 10.1175/1520-0469(1992)049⟨2139:OTCDMF⟩2.0.CO;2.

Geleyn, J. F. and Hollingsworth, A. (1979). An economical analytical method for the computation of the interaction between scattering and line absorption of radiation. *Contrib. Atmos. Phys.*, **52**, 1–16.

Grabowski, W. W. (2001). Coupling cloud processes with the large-scale dynamics using the Cloud-Resolving Convection Parameterization (CRCP). *J. Atmos. Sci.*, **58** (**9**), 978–997, doi: 10.1175/1520-0469(2001)058⟨0978:CCPWTL⟩2.0.CO;2.

Grabowski, W. W. (2003). MJO-like coherent structures: Sensitivity simulations using the Cloud-Resolving Convection Parameterization (CRCP). *J. Atmos. Sci.*, **60** (**6**), 847–864, doi: 10.1175/1520-0469(2003)060⟨0847:MLCSSS⟩2.0.CO;2.

Grabowski, W. W. (2016). Towards global large eddy simulation: Super-parameterization revisited. *J. Meteorol. Soc. Japan*, **94** (**4**), 327–344, doi: 10.2151/jmsj.2016-017.

Guichard, F. and Couvreux, F. (2017). A short review of numerical cloud-resolving models. *Tellus A: Dynamic Meteorology and Oceanography*, **69** (**1**), 1373578, doi: 10.1080/16000870.2017.1373578.

Haigh, J. D. (1984). Radiative heating in the lower stratosphere and the distribution of ozone in a two-dimensional model. *Q. J. R. Meteorol. Soc.*, **110** (**463**), 167–185, doi: 10.1002/qj.49711046312.

Hansen, J. E. and Travis, L. D. (1974). Light scattering in planetary atmospheres. *Space Sci. Rev.*, **16**, 527–610, doi: 10.1007/BF00168069.

Harrington, J. Y., Feingold, G., and Cotton, W. R. (2000). Radiative impacts on the growth of a population of drops within simulated summertime arctic stratus. *J. Atmos. Sci*, **57** (**5**), 766–785, doi: 10.1175/1520-0469(2000)057⟨0766:RIOTGO⟩2.0.CO;2.

Hartmann, D. L., Gasparini, B., Berry, S. E., and Blossey, P. N. (2018). The life cycle and net radiative effect of tropical anvil clouds. *J. Adv. Model. Earth Syst.*, **10** (**12**), 3012–3029, doi: 10.1029/2018MS001484.

Haynes, J. M. and Stephens, G. L. (2007). Tropical oceanic cloudiness and the incidence of precipitation: Early results from CloudSat. *Geophys. Res. Lett.*, **34** (**L09811**), doi: 10.1029/2007GL029335.

He, T., Liang, S., and Song, D.-X. (2014). Analysis of global land surface albedo climatology and spatial-temporal variation during 1981–2010 from multiple satellite products. *J. Geophys. Res. Atmos.*, **119** (**10**), 10,281–10,298, doi: 10.1002/2014JD021667.

Heiblum, R. H., Pinto, L., Altaratz, O., Dagan, G., and Koren, I. (2019). Core and margin in warm convective clouds – Part 1: Core types and evolution during a cloud's lifetime. *J. Atmos. Sci.*, **34** (**16**), 367–381, doi: 10.5194/acp-19-10717-2019.

Henyey, L. and Greenstein, J. (1941). Diffuse radiation in the galaxy. *Astrophys. J.*, **93**, 70–83, doi: 10.1086/144246.

Heus, T. and Jonker, H. J. J. (2008). Subsiding shells around shallow cumulus clouds. *J. Atmos. Sci.*, **65** (**3**), 1003–1018, doi: 10.1175/2007JAS2322.1.

Heus, T., Pols, C. F. J., Jonker, H. J. J., den Akker, V., A., H. E., and Lenschow, D. H. (2009). Observational validation of the compensating mass flux through the shell around cumulus clouds. *Q. J. R. Meteorol. Soc.*, **135** (**638**), 101–112, doi: 10.1002/qj.358.

Heymsfield, A. J. (1977). Precipitation development in stratiform ice clouds: A microphysical and dynamical study. *J. Atmos. Sci.*, **34** (**2**), 367–381, doi: 10.1175/1520-0469(1977)034⟨0367:PDISIC⟩2.0.CO;2.

Hill, P. G., Hogan, R. J., Manners, J., and Petch, J. C. (2012). Parametrizing the horizontal inhomogeneity of ice water content using CloudSat data products. *Q. J. R. Meteorol. Soc.*, **138** (**668**), 1784–1793, doi: 10.1002/qj.1893.

Hill, P. G., Morcrette, C. J., and Boutle, I. A. (2015). A regime-dependent parameterization of subgrid-scale cloud water content variability. *Q. J. R. Meteorol. Soc.*, **141** (**691**), 1975–1986, doi: 10.1002/qj.2506.

Hinkelman, L. M., Evans, K. F., Clothiaux, E. E., Ackerman, T. P., and Stackhouse, P. W. (2007). The effect of cumulus cloud field anisotropy on domain-averaged solar fluxes and atmospheric heating rates. *J. Atmos. Sci.*, **64** (**10**), 3499–3520, doi: 10.1175/JAS4032.1.

Hogan, R. et al. (2017). Radiation in numerical weather prediction. *ECMWF Technical Memorandum*, **816**, doi: 10.21957/2bd5dkj8x.

Hogan, R. J. and Bozzo, A. (2015). Mitigating errors in surface temperature forecasts using approximate radiation updates. *J. Adv. Model. Earth Syst.*, **7** (**2**), 836–853, doi: 10.1002/2015MS000455.

Hogan, R. J. and Bozzo, A. (2016). ECRAD: A new radiation scheme for the IFS. *ECMWF Technical Memorandum*, **787**, doi: 10.21957/whntqkfdz.

Hogan, R. J. and Bozzo, A. (2018). A flexible and efficient radiation scheme for the ECMWF model. *J. Adv. Model. Earth Syst.*, **10** (**8**), 1990–2008, doi: 10.1029/2018MS001364.

Hogan, R. J. and Illingworth, A. J. (2000). Deriving cloud overlap statistics from radar. *Q. J. R. Meteorol. Soc.*, **126** (**569**), 2903–2909, doi: 10.1002/qj.49712656914.

Hogan, R. J. and Illingworth, A. J. (2003). Parameterizing ice cloud inhomogeneity and the overlap of inhomogeneities using cloud radar data. *J. Atmos. Sci.*, **60** (**5**), 756–767, doi: 10.1175/1520-0469(2003)060⟨0756:PICIAT⟩2.0.CO;2.

Hogan, R. J. and Kew, S. F. (2005). A 3D stochastic cloud model for investigating the radiative properties of inhomogeneous cirrus clouds. *Q. J. R. Meteorol. Soc.*, **131** (**611**), 2585–2608, doi: 10.1256/qj.04.144.

Hogan, R. J. and Shonk, J. K. P. (2013). Incorporating the effects of 3D radiative transfer in the presence of clouds into two-stream multilayer radiation schemes. *J. Atmos. Sci.*, **70** (**2**), 708–724, doi: 10.1175/JAS-D-12-041.1.

Hogan, R. J., Bouniol, D., Ladd, D. N., O'Connor, E. J., and Illingworth, A. J. (2003). Absolute calibration of 94/95-GHz radars using rain. *J. Atmos. Ocean. Technol.*, **20** (**4**), 572–580, doi: 10.1175/1520-0426(2003)20⟨572:ACOGRU⟩2.0.CO;2.

Hogan, R. J., Schäfer, S. A. K., Klinger, C., and Mayer, B. (2016). Representing 3-D cloud radiation effects in two-stream schemes: 2. Matrix formulation and broadband evaluation. *J. Geophys. Res. Atmos.*, **121** (**14**), 8583–8599, doi: 10.1002/2016JD024875.

Hogan, R. J., Fielding, M. D., Barker, H. W., Villefranque, N., and Schäfer, S. A. K. (2019). Entrapment: An important mechanism to explain the shortwave 3D radiative effect of clouds. *J. Atmos. Sci.*, **76** (**7**), 2123–2141, doi: 10.1175/JAS-D-18-0366.1.

Houze, R. A. *Cloud Dynamics*. Academic Press, San Diego, California, (1993).

Hu, Y. X. and Stamnes, K. (1993). An accurate parameterization of the radiative properties of water clouds suitable for use in climate models. *J. Climate*, **6** (**4**), 728–742, doi: 10.1175/1520-0442(1993)006⟨0728:AAPOTR⟩2.0.CO;2.

IPCC. *Climate Change 2014: Synthesis Report*. Contribution of Working Groups I, II and III to the Fifth Assessment Report of the Intergovernmental Panel on Climate Change, Geneva, Switzerland, (2014).

IPCC. *Global Warming of 1.5˚C*. An IPCC Special Report on the impacts of global warming of 1.5°C above pre-industrial levels and related global greenhouse gas emission pathways, in the context of strengthening the global response to the threat of climate change, sustainable development, and efforts to eradicate poverty, Geneva, Switzerland, (2018).

Jakub, F. *On the impact of three dimensional radiative transfer on cloud evolution*. PhD thesis, Ludwig-Maximilians-Universität München, (2016).

Jakub, F. and Mayer, B. (2015). A three-dimensional parallel radiative transfer model for atmospheric heating rates for use in cloud resolving models – The TenStream solver. *J. Quant. Spectrosc. Radiat. Transfer*, **163**, 63–71, doi: 10.1016/j.jqsrt.2015.05.003.

Jakub, F. and Mayer, B. (2016). 3-D radiative transfer in large-eddy simulations – experiences coupling the TenStream solver to the UCLA-LES. *Geosci. Model Dev.*, **9** (**4**), 1413–1422, doi: 10.5194/gmd-9-1413-2016.

Jakub, F. and Mayer, B. (2017). The role of 1-D and 3-D radiative heating in the organization of shallow cumulus convection and the formation of cloud streets. *Atmos. Chem. Phys.*, **17** (**21**), 13317–13327, doi: 10.5194/acp-17-13317-2017.

Johnson, R. H., Rickenbach, T. M., Rutledge, S. A., Ciesielski, P. E., and Schubert, W. H. (1999). Trimodal characteristics of tropical convection. *J. Atmos. Sci.*, **12** (**8**), 2397–2418, doi: 10.1175/1520-0442(1999)012⟨2397:TCOTC⟩2.0.CO;2.

Jonker, H. J. J., Heus, T., and Sullivan, P. P. (2008). A refined view of vertical mass transport by cumulus convection. *Geophys. Res. Lett.*, **35** (**L07810**), doi: 10.1029/2007GL032606.

Joseph, J. H., Wiscombe, W. J., and Weinman, J. A. (1976). The delta-Eddington approximation for radiative flux transfer. *J. Atmos. Sci.*, **33** (**12**), 2452–2459, doi: 10.1175/1520-0469(1976)033⟨2452:TDEAFR⟩2.0.CO;2.

Kablick, G. P., Ellingson, R. G., Takara, E. E., and Gu, J. (2011). Longwave 3D benchmarks for inhomogeneous clouds and comparisons with approximate methods. *J. Climate*, **24** (**8**), 2192–2205, doi: 10.1175/2010JCLI3752.1.

Kato, S., Ackerman, T. P., Mather, J. H., and Clothiaux, E. E. (1999). The k-distribution method and correlated-k approximation for a shortwave radiative transfer model. *J. Quant. Spectrosc. Radiat. Transfer*, **62** (**1**), 109–121, doi: 10.1016/S0022-4073(98)00075-2.

Khairoutdinov, M. F. and Randall, D. A. (2003). Cloud resolving modeling of the ARM summer 1997 IOP: Model formulation, results, uncertainties, and sensitivities. *J. Atmos. Sci.*, **60** (**4**), 607–625, doi: 10.1175/1520-0469(2003)060⟨0607:CRMOTA⟩2.0.CO;2.

Kirchhoff, G. (1890). Über das Verhältniss zwischen dem Emissionsvermögen und dem Absorptionsvermögen der Körper für Wärme und Licht. *Annalen der Physik*, **109**, 275–301, doi: 10.1002/andp.18601850205.

Klemp, J. B. and Wilhelmson, R. B. (1978). The simulation of three-dimensional convective storm dynamics. *J. Atmos. Sci.*, **35** (**6**), 1070–1096, doi: 10.1175/1520-0469(1978)035⟨1070:TSOTDC⟩2.0.CO;2.

Klinger, C. and Mayer, B. (2014). Three-dimensional Monte Carlo calculation of atmospheric thermal heating rates. *J. Quant. Spectrosc. Radiat. Transfer*, **144**, 123–136, doi: 10.1016/j.jqsrt.2014.04.009.

Klinger, C. and Mayer, B. (2016). The Neighboring Column Approximation (NCA) – A fast approach for the calculation of 3D thermal heating rates in cloud resolving models. *J. Quant. Spectrosc. Radiat. Transfer*, **168**, 17–28, doi: 10.1016/j.jqsrt.2015.08.020.

Klinger, C., Mayer, B., Jakub, F., Zinner, T., Park, S.-B., and Gentine, P. (2017). Effects of 3-D thermal radiation on the development of a shallow cumulus cloud field. *Atmos. Chem. Phys.*, **17** (**8**), 5477–5500, doi: 10.5194/acp-17-5477-2017.

Klinger, C., Feingold, G., and Yamaguchi, T. (2019). Cloud droplet growth in shallow cumulus clouds considering 1-D and 3-D thermal radiative effects. *Atmos. Chem. Phys.*, **19** (**9**), 6295–6313, doi: 10.5194/acp-19-6295-2019.

Kobayashi, T. (1988). Parameterization of reflectivity for broken cloud fields. *J. Atmos. Sci.*, **45** (**21**), 3034–3045, doi: 10.1175/1520-0469(1988)045⟨3034:PORFBC⟩2.0.CO;2.

Kurucz, R. (1992). Synthetic infrared spectra. *Proc. Int. Astron. Union*, **154**, doi: 10.1017/S0074180900124805.

Lacis, A. and Hansen, J. E. (1974). A parameterization for the absorption of solar radiation in the Earth's atmosphere. *J. Atmos. Sci.*, **31** (**1**), 118–133, doi: 10.1175/1520-0469(1974)031⟨0118:APFTAO⟩2.0.CO;2.

Lamb, D. and Verlinde, J. *Physics and chemistry of clouds*. Cambridge University Press, Cambridge, UK, (2011).

Lang, S., Tao, W.-K., Ciffeli, R., Olson, W., Halverson, J., Rutledge, S., and Simpson, J. (2007). Improving simulations of convective systems from TRMM LBA: Easterly and westerly regimes. *J. Atmos. Sci.*, **64** (**4**), 1141–1164, doi: 10.1175/JAS3879.1.

Li, J., Scinocca, J., Lazare, M., McFarlane, N., von Salzen, K., and Solheim, L. (2006). Ocean surface albedo and its impact on radiation balance in climate models. *J. Climate*, **19** (**24**), 6314–6333, doi: 10.1175/JCLI3973.1.

Lohmann, U. and Roeckner, E. (1996). Design and performance of a new cloud microphysics scheme developed for the ECHAM general circulation model. *Clim. Dyn.*, **12** (**8**), 557–572, doi: 10.1007/BF00207939.

Lohmann, U., Lüönd, F., and Mahrt, F. *An introduction to clouds: from the microscale to climate*. Cambridge University Press, Cambridge, UK, (2016).

Lüthi, D. et al. (2008). High-resolution carbon dioxide concentration record 650,000–800,000 years before present. *Nature*, **453** (**7193**), 379–382, doi: 10.1038/nature06949.

Mace, G. G. and Benson-Troth, S. (2002). Cloud-layer overlap characteristics derived from long-term cloud radar data. *J. Climate*, **15** (**17**), 2505–2515, doi: 10.1175/1520-0442(2002)015⟨2505:CLOCDF⟩2.0.CO;2.

Manabe, S. (1969). Climate and the ocean circulation: I. The atmospheric circulation and the hydrology of the Earth's surface. *Mon. Wea. Rev.*, **97** (**11**), 739–774, doi: 10.1175/1520-0493(1969)097⟨0739:CATOC⟩2.3.CO;2.

Manabe, S. and Strickler, R. (1964). Thermal equilibrium of the atmosphere with a convective adjustment scheme. *J. Atmos. Sci.*, **21** (**4**), 361–385, doi: 10.1175/1520-0469(1964)021⟨0361:TEOTAW⟩2.0.CO;2.

Marshak, A. and Davis, A. *3D radiative transfer in cloudy atmospheres*. Springer, Berlin, Heidelberg, New York, (2005).

Marshak, A., Davis, A., Wiscombe, W., and Cahalan, R. (1985). Radiative smoothing in fractal clouds. *J. Geophys. Res.*, **100** (**D12**), 26247–26261, doi: 10.1029/95JD02895.

Mayer, B. (1999). I3RC phase 1 results from the MYSTIC Monte Carlo model. *In: Intercomparison of three-dimensional radiation codes: Abstracts of the first and second international workshops, University of Arizona Press*, pages 49–54.

Mayer, B. (2000). I3RC phase 2 results from the MYSTIC Monte Carlo model. *In: Intercomparison of three-dimensional radiation codes: Abstracts of the first and second international workshops, University of Arizona Press*, pages 107–108.

Mayer, B. (2009). Radiative transfer in the cloudy atmosphere. *Eur. Phys. J. Confer.*, **1**, 75–99, doi: 10.1140/epjconf/e2009-00912-1.

Mayer, B. and Kylling, A. (2005). Technical note: The libRadtran software package for radiative transfer calculations - description and examples of use. *Atmos. Chem. Phys.*, **5** (**7**), 1855–1877, doi: 10.5194/acp-5-1855-2005.

Mie, G. (1908). Beiträge zur Optik trüber Medien, speziell kolloidaler Metallösugen. *Annalen der Physik*, **25** (**3**), 377–445.

Mitchell, D. L. (1994). A model predicting the evolution of ice particle size spectra and radiative properties of cirrus clouds. Part I: Microphysics. *J. Atmos. Sci.*, **51** (**6**), 797–816, doi: 10.1175/1520-0469(1994)051⟨0797:AMPTEO⟩2.0.CO;2.

Mlawer, E. J., Taubman, S. J., Brown, P. D., Iacono, M. J., and Clough, S. A. (1997). Radiative transfer for inhomogeneous atmospheres: RRTM, a validated correlated-k model for the longwave. *J. Geophys. Res.*, **102** (**D14**), 16663–16682, doi: 10.1029/97JD00237.

Morcrette, J.-J. and Fouquart, Y. (1986). The overlapping of cloud layers in shortwave radiation parameterizations. *J. Atmos. Sci.*, **43** (**4**), 321–328, doi: 10.1175/1520-0469(1986)043⟨0321:TOOCLI⟩2.0.CO;2.

Morcrette, J.-J., Barker, H. W., Cole, J. N. S., Iacono, M. J., and Pincus, R. (2008). Impact of a new radiation package, McRad, in the ECMWF Integrated Forecasting System. *Mon. Wea. Rev.*, **136** (**12**), 4773–4798, doi: 10.1175/2008MWR2363.1.

Naud, C. M., Del Genio, A., Mace, G. G., Benson, S., Clothiaux, E. E., and Kollias, P. (2008). Impact of dynamics and atmospheric state on cloud vertical overlap. *J. Climate*, **21** (**8**), 1758–1770, doi: 10.1175/2007JCLI1828.1.

Neggers, R. A. J., Duynkerke, P. G., and Rodts, S. M. A. (2003). Shallow cumulus convection: A validation of large-eddy simulation against aircraft and Landsat observations. *Q. J. R. Meteorol. Soc.*, **129** (**593**), 2671–2696, doi: 10.1256/qj.02.93.

Neokum, R., Steiger, N., Gómez-Navarro, J. J., Wang, J., and Werner, J. P. (2019a). No evidence for globally coherent warm and cold periods over the preindustrial Common Era. *Nature*, **571** (**7766**), 550–554, doi: 10.1038/s41586-019-1401-2.

Neokum, R. et al. (2019b). Consistent multidecadal variability in global temperature reconstructions and simulations over the Common Era. *Nature Geoscience*, **12** (**8**), 643–649.

Norris, J. R. (1998). Low cloud type over the ocean from surface observations. Part I: Relationship to surface meteorology and the vertical distribution of temperature and moisture. *J. Atmos. Sci.*, **11** (**3**), 369–382, doi: 10.1175/1520-0442(1998)011⟨0369:LCTOTO⟩2.0.CO;2.

Oreopoulos, L. and Barker, H. W. (1999). Accounting for subgrid-scale cloud variability in a multi-layer 1d solar radiative transfer algorithm. *Q. J. R. Meteorol. Soc.*, **125** (**553**), 301–330, doi: 10.1002/qj.49712555316.

Oreopoulos, L. and Cahalan, R. F. (2005). Cloud inhomogeneity from MODIS. *J. Climate*, **18** (**23**), 5110–5124, doi: 10.1175/JCLI3591.1.

O'Hirok, W. and Gautier, C. (1998a). A three-dimensional radiative transfer model to investigate the solar radiation within a cloudy atmosphere. Part I: Spatial effects. *J. Atmos. Sci.*, **55** (**12**), 2162–2179, doi: 10.1175/1520-0469(1998)055⟨2162:ATDRTM⟩2.0.CO;2.

O'Hirok, W. and Gautier, C. (1998b). A three-dimensional radiative transfer model to investigate the solar radiation within a cloudy atmosphere. Part II: Spectral effects. *J. Atmos. Sci.*, **55** (**19**), 3065–3076, doi: 10.1175/1520-0469(1998)055⟨3065:ATDRTM⟩2.0.CO;2.

O'Hirok, W. and Gautier, C. (2005). The impact of model resolution on differences between Independent Column Approximation and Monte Carlo estimates of shortwave surface irradiance and atmospheric heating rate. *J. Atmos. Sci.*, **62** (**8**), 2939–2951, doi: 10.1175/JAS3519.1.

Petters, J. L., Harrington, J. Y., and Clothiaux, E. E. (2012). Radiative-dynamical feedbacks in low liquid water path stratiform clouds. *J. Atmos. Sci.*, **69** (**5**), 1498–1512, doi: 10.1175/JAS-D-11-0169.1.

Pincus, R., McFarlane, S. A., and Klein, S. A. (1999). Albedo bias and the horizontal variability of clouds in subtropical marine boundary layers: Observations from ships and satellites. *J. Geophys. Res.*, **104** (**D6**), 6183–6191, doi: 10.1029/2002JD003322.

Pincus, R., Barker, H. W., and Morcrette, J.-J. (2003). A fast, flexible, approximate technique for computing radiative transfer in inhomogeneous cloud fields. *J. Geophys. Res.*, **108** (**D13**), 1463–1478, doi: 10.1029/2002JD003322.

Planck, M. *Zur Theorie des Gesetzes der Energieverteilung im Normalspektrum.* In: Verhandlungen der Deutschen physikalischen Gesellschaft, (1900).

Quaas, J. (2012). Evaluating the critical relative humidity as a measure of subgrid-scale variability of humidity in general circulation model cloud cover parameterizations using satellite data. *J. Geophys. Res.*, **117** (**D9**), doi: 10.1029/2012JD017495.

Räisänen, P. (2002). Two-stream approximations revisited: A new improvement and tests with GCM data. *Mon. Wea. Rev.*, **120** (**585**), 303–325, doi: 10.1256/qj.01.161.

Räisänen, P. (2004). Stochastic generation of subgrid-scale cloudy columns for large-scale models. *Q. J. R. Meteorol. Soc.*, **130** (**601**), 2047–2067, doi: 10.1256/qj.03.99.

Randall, D., Khairoutdinov, M., Arakawa, A., and Grabowski, W. W. (2003). Breaking the Cloud Parameterization Deadlock. *Bull. Am. Meteorol. Soc.*, **84** (**11**), 1547–1564, doi: 10.1175/BAMS-84-11-1547.

Randall, D. A. (1980). Conditional Instability of the First Kind Upside-Down. *J. Atmos. Sci.*, **37** (**1**), 125–130, doi: 10.1175/1520-0469(1980)037⟨0125:CIOTFK⟩2.0.CO;2.

Randall, D. A., Coakley, J. A., Fairall, C. W., Kropfli, R. A., and Lenschow, D. H. (1984). Outlook for research on subtropical marine stratiform clouds. *Bull. Am. Meteorol. Soc.*, **65** (**12**), 1290–1301, doi: 10.1175/1520-0477(1984)065⟨1290:OFROSM⟩2.0.CO;2.

Randall, D. A. et al. *Climate models and their evaluation.* In: Climate Change 2007: The Physical Science Basis. Contribution of Working Group I to the Fourth Assessment Report of the Intergovernmental Panel on Climate Change. Cambridge University Press, Cambridge, UK and New York, USA, (2007).

Rasp, S., Schulz, H., Bony, S., and Stevens, B. (2019). Combining crowd-sourcing and deep learning to understand meso-scale organization of shallow convection. *arXiv:1906.01906*.

Rauber, R. M. et al. (2007). Rain in Shallow Cumulus Over the Ocean: The RICO Campaign. *Bull. Am. Meteorol. Soc.*, **88** (**12**), 1912–1928, doi: 10.1175/BAMS-88-12-1912.

Rickenbach, T. M. and Rutledge, S. A. (1998). Convection in TOGA COARE: Horizontal scale, morphology, and rainfall production. *J. Atmos. Sci.*, **55** (**17**), 2715–2729, doi: 10.1175/1520-0469(1998)055⟨2715:CITCHS⟩2.0.CO;2.

Ritter, B. and Geleyn, J. F. (1992). A comprehensive radiation scheme for numerical weather prediction models with potential applications in climate simulations. *Mon. Wea. Rev.*, **120** (**2**), 303–325, doi: 10.1175/1520-0493(1992)120⟨0303:ACRSFN⟩2.0.CO;2.

Rodts, S. M., Duynkerke, P. G., and Jonker, H. J. (2003). Size distributions and dynamical properties of shallow cumulus clouds from aircraft observations and satellite data. *J. Atmos. Sci.*, **60** (**16**), 1895–1912, doi: 10.1175/1520-0469(2003)0601895:SDADPO2.0.CO;2.

Roeckner, E. et al. (2003). The atmospheric general circulation model ECHAM5. Part I: Model description. *Max Planck Institute for Meteorology Rep. 349, 127 pp.*

Rossow, W. B., Delo, C., and Cairns, B. (2002). Implications of the observed mesoscale variations of clouds for the Earth's radiation budget. *J. Climate*, **15** (**6**), 557–585, doi: 10.1175/1520-0442(2002)015⟨0557:IOTOMV⟩2.0.CO;2.

Räisänen, P. and Barker, H. W. (2004). Evaluation and optimization of sampling errors for the Monte Carlo Independent Column Approximation. *Q. J. R. Meteorol. Soc.*, **130** (**601**), 2069–2085, doi: 10.1256/qj.03.215.

Räisänen, P., Barker, H. W., and Cole, J. N. S. (2005). The Monte Carlo Independent Column Approximation's conditional random noise: Impact on simulated climate. *J. Climate*, **18** (**22**), 4715–4730, doi: 10.1175/JCLI3556.1.

Räisänen, P., Järvenoja, S., Järvinen, H., Giorgetta, M., Roeckner, E., Jylhä, K., and Ruosteenoja, K. (2007). Tests of Monte Carlo Independent Column Approximation in the ECHAM5 atmospheric GCM. *J. Climate*, **20** (**19**), 4995–5011, doi: 10.1175/JCLI4290.1.

Schmetz, J. (1984). On the parameterization of the radiative properties of broken clouds. *Tellus A: Dynamic Meteorology and Oceanography*, **36** (**5**), 417–432, doi: 10.3402/tellusa.v36i5.11644.

Schneider, T., Teixeira, J., Bretherton, C. S., Brient, F., Pressel, K. G., Schär, C., and Siebesma, A. P. (2017). Climate goals and computing the future of clouds. *Nature Climate Change*, **7** (**1**), 3–5, doi: 10.1038/nclimate3190.

Schuster, A. (1905). Radiation through a foggy atmosphere. *Astrophys. J.*, **21** (**1**), 1–22.

Schwarzschild, K. (1906). Über das Gleichgewicht der Sonnenatmosphäre. Nachrichten von der Königlichen Gesellschaft der Wissenschaften zu Göttingen. *Math.-phys. Klasse*, **195**, 41–53.

Schäfer, S. A. K., Hogan, R., Klinger, C., Chiu, J. C., and B., M. (2016). Representing 3-D cloud radiation effects in two-stream schemes: 1. Longwave considerations and effective cloud edge length. *J. Geophys. Res. Atmos.*, **121** (**14**), 8567–8582, doi: 10.1002/2016JD024876.

Seifert, A. and Heus, T. (2013). Large-eddy simulation of organized precipitating trade wind cumulus clouds. *Atmos. Chem. Phys.*, **13** (**11**), 5631–5645, doi: 10.5194/acp-13-5631-2013.

Seigel, R. B. (2014). Shallow cumulus mixing and subcloud-layer responses to variations in aerosol loading. *J. Atmos. Sci.*, **71** (**7**), 2581–2603, doi: 10.1175/JAS-D-13-0352.1.

Shonk, J. K. P. and Hogan, R. J. (2008). Tripleclouds: An efficient method for representing horizontal cloud inhomogeneity in 1D radiation schemes by using three regions at each height. *J. Climate*, **21** (**11**), 2352–2370, doi: 10.1175/2007JCLI1940.1.

Shonk, J. K. P. and Hogan, R. J. (2010). Effect of improving representation of horizontal and vertical cloud structure on the Earth's global radiation budget. Part II: The global effects. *Q. J. R. Meteorol. Soc.*, **136** (**650**), 1205–1215, doi: 10.1002/qj.646.

Shonk, J. K. P., Hogan, R. J., Edwards, J. M., and Mace, G. G. (2010). Effect of improving representation of horizontal and vertical cloud structure on the Earth's global radiation budget. Part I: Review and parameterization. *Q. J. R. Meteorol. Soc.*, **136** (**650**), 1191–1204, doi: 10.1002/qj.647.

Simpson, J., Adler, R. F., and Gerald, N. (1988). A proposed Tropical Rainfall Measuring Mission (TRMM) satellite. *Bull. Am. Meteorol. Soc.*, **69** (**3**), 278–295, doi: 10.1175/1520-0477(1988)069⟨0278:APTRMM⟩2.0.CO;2.

Simpson, J., Kummerow, C., Tao, W.-K., and Adler, R. F. (1996). On the Tropical Rainfall Measuring Mission (TRMM). *Meteor. Atmos. Phys.*, **60** (**1**), 19–36.

Slingo, J. M. (1980). A cloud parametrization scheme derived from GATE data for use with a numerical model. *Q. J. R. Meteorol. Soc.*, **106** (**450**), 747–770, doi: 10.1002/qj.49710645008.

Smith, S. A. and Del Genio, A. D. (2001). Analysis of aircraft, radiosonde, and radar observations in cirrus clouds observed during FIRE II: The interactions between environmental structure, turbulence, and cloud. *J. Atmos. Sci.*, **58** (**5**), 451–461, doi: 10.1175/1520-0469(2001)058⟨0451:AOARAR⟩2.0.CO;2.

Sommeria, G. and Deardorff, J. W. (1977). Subgrid-scale condensation in models of nonprecipitating clouds. *J. Atmos. Sci.*, **34** (**2**), 344–355, doi: 10.1175/1520-0469(1977)034⟨0344:SSCIMO⟩2.0.CO;2.

Stefan, J. (1879). Über die Beziehung zwischen der Wärmestrahlung und der Temperatur. *Sitzungsberichte der Kaiserlichen Akademie der Wissenschaften in Wien*, **79**, 391–428.

Stensrud, D. J. *Parameterization schemes: Keys to understanding numerical weather prediction models*. Cambridge University Press, Cambridge, UK, (2007).

Stephens, G. L. (1984). The parameterization of radiation for numerical weather prediction and climate models. *Mon. Wea. Rev.*, **112** (**4**), 826–867, doi: 10.1175/1520-0493(1984)112⟨0826:TPORFN⟩2.0.CO;2.

Stephens, G. L. and Webster, P. J. (1981). Clouds and climate: Sensitivity of simple systems. *J. Atmos. Sci.*, **38** (**2**), 235–247, doi: 10.1175/1520-0469(1981)038⟨0235:CACSOS⟩2.0.CO;2.

Stephens, G. L., Gabriel, P. M., and Tsay, S.-C. (1991). Statistical radiative transport in one-dimensional media and its application to the terrestrial atmosphere. *Transport Theor. Stat.*, **20** (**2-3**), 139–175, doi: 10.1080/00411459108203900.

Stephens, G. L., Gabriel, P. M., and Partain, P. T. (2001). Parameterization of atmospheric radiative transfer. Part I: Validity of simple models. *J. Atmos. Sci.*, **58** (**22**), 3391–3409, doi: 10.1175/1520-0469(2001)058⟨3391:POARTP⟩2.0.CO;2.

Stephens, G. L. et al. (2002). The CloudSat mission and the A-Train: A new dimension of space-based observations of clouds and precipitation. *Bull. Am. Meteorol. Soc.*, **83**, 1771–1790, doi: 10.1175/BAMS-83-12-1771.

Stephens, G. L. et al. (2008). CloudSat mission: Performance and early science after the first year of operation. *J. Geophys. Res.*, **113** (**D00A18**), doi: 10.1029/2008JD009982.

Stevens, B. (2007). On the growth of layers of nonprecipitating cumulus convection. *J. Atmos. Sci.*, **64** (**8**), 2916–2931, doi: 10.1175/JAS3983.1.

Stevens, B. and Bony, S. (2013). What are climate models missing? *Science*, **340** (**6136**), 1053–1054, doi: 10.1126/science.1237554.

Stevens, B., Moeng, C.-H., and Sullivan, P. P. (1999). Large-eddy simulations of radiatively driven convection: Sensitivities to the representation of small scales. *J. Atmos. Sci.*, **56** (**23**), 3963–3984, doi: 10.1175/1520-0469(1999)056⟨3963:LESORD⟩2.0.CO;2.

Stevens, B. et al. (2005). Evaluation of large-eddy simulations via observations of nocturnal marine stratocumulus. *Mon. Wea. Rev.*, **133** (**6**), 1443–1462, doi: 10.1175/MWR2930.1.

Stevens, B. et al. (2019). Sugar, gravel, fish, and flowers: Mesoscale cloud patterns in the tradewinds. *Q. J. R. Meteorol. Soc.*, **146** (**726**), 141–152, doi: 10.1002/qj.3662.

Strutt, J. W. (1871). On the scattering of light by small particles. *The London, Edinburgh and Dublin Philosophical Magazine and Journal of Science*, **41** (**275**), 447–454, doi: 10.1080/14786447108640507.

Su, H., Jiang, J. H., Vane, D. G., and Stephens, G. L. (2008). Observed vertical structure of tropical oceanic clouds sorted in large-scale regimes. *Geophys. Res. Lett.*, **35** (**L24704**), doi: 10.1029/2008GL035888.

Sundqvist, H., Berge, E., and Kristjánsson, J. E. (1989). Condensation and cloud parameterization studies with a mesoscale numerical weather prediction model. *Mon. Wea. Rev.*, **117** (**8**), 1641–1657, doi: 10.1175/1520-0493(1989)117⟨1641:CACPSW⟩2.0.CO;2.

Tao, W.-K. and Simpson, J. (1993). The Goddard Cumulus Ensemble model. Part I: Model description. *Terr. Atmos. Oceanic Sci.*, **4** (**1**), 35–72, doi: 10.3319/TAO.1993.4.1.35(A).

Tao, W.-K. et al. (2003). Microphysics, radiation and surface processes in the Goddard Cumulus Ensemble (GCE) model. *Meteorol. Atmos. Phys.*, **82**, 97–137, doi: 10.1007/s00703-001-0594-7.

Thomas, G. and Stamnes, K. *Radiative transfer in the atmosphere and ocean*. Cambridge University Press, Cambridge, UK, (1999).

Tian, L. and Curry, J. A. (1989). Cloud overlap statistics. *J. Geophys. Res.*, **94** (**D7**), 9925–9935, doi: 10.1029/JD094iD07p09925.

Tiedtke, M. (1989). A comprehensive mass flux scheme for cumulus parameterization in large-scale models. *Mon. Wea. Rev.*, **117** (**8**), 1779–1800, doi: 10.1175/1520-0493(1989)117⟨1779:ACMFSF⟩2.0.CO;2.

Tiedtke, M. (1996). An extension of cloud-radiation parameterization in the ECMWF model: The representation of subgrid-scale variations of optical depth. *Mon. Wea. Rev.*, **124** (**4**), 745–750, doi: 10.1175/1520-0493(1996)124⟨0745:AEOCRP⟩2.0.CO;2.

Tompkins, A. M. (2002). A prognostic parameterization for the subgrid-scale variability of water vapor and clouds in large-scale models and its use to diagnose cloud cover. *J. Atmos. Sci.*, **59** (**12**), 1917–1942, doi: 10.1175/1520-0469(2002)059⟨1917:APPFTS⟩2.0.CO;2.

Tompkins, A. M. (2005). The parameterization of cloud cover. *ECMWF Technical Memorandum*.

Tompkins, A. M. and Di Giuseppe, F. (2003). Solar radiative biases in deep convective regimes: Possible implications for dynamical feedback. *Q. J. R. Meteorol. Soc.*, **129** (**590**), 1721–1730, doi: 10.1256/qj.02.105.

Tompkins, A. M. and Di Giuseppe, F. (2007). Generalizing cloud overlap treatment to include solar zenith angle effects on cloud geometry. *J. Atmos. Sci.*, **64** (**6**), 2116–2125, doi: 10.1175/JAS3925.1.

von Helmholtz, H. and König, A. *Handbuch der physiologischen Optik*. No. Bd. 1 in Handbuch der physiologischen Optik, L. Voss, Hamburg and Leipzig, (1896).

Várnai, T. and Davies, R. (1999). Effects of cloud heterogeneities on shortwave radiation: Comparison of cloud-top variability and internal heterogeneity. *J. Atmos. Sci.*, **56** (**24**), 4206–4224, doi: 10.1175/1520-0469(1999)056⟨4206:EOCHOS⟩2.0.CO;2.

Wallace, J. M. and Hobbs, P. V. *Atmospheric science – An introductory survey*. International Geophysics, Elsevier Science, (2006).

Wang, S. and Lenschow, D. H. (1995). An observational study of the role of penetrating cumulus in a marine stratocumulus-topped boundary layer. *J. Atmos. Sci.*, **52** (**16**), 2902–2922, doi: 10.1175/1520-0469(1995)052⟨2778:AOSOTR⟩2.0.CO;2.

Wang, Y., Geerts, B., and French, J. (2009). Dynamics of the cumulus cloud margin: An observational study. *J. Atmos. Sci.*, **66** (**12**), 3660–3677, doi: 10.1175/2009JAS3129.1.

Wapler, K. and Mayer, B. (2008). A fast three-dimensional approximation for the calculation of surface irradiance in large-eddy simulation models. *J. Appl. Meteor. Climatol.*, **47** (**12**), 3061–3071, doi: 10.1175/2008JAMC1842.1.

Warner, J. (1955). The water content of cumuliform cloud. *Tellus*, **7** (**4**), 449–457, doi: 10.1111/j.2153-3490.1955.tb01183.x.

Warner, T. T. *Numerical weather and climate prediction*. Cambridge University Press, Cambridge, UK, (2011).

Webster, P. J. and Lukas, R. (1992). TOGA COARE: The Coupled Ocean–Atmosphere Response Experiment. *Bull. Am. Meteorol. Soc.*, **73** (**9**), 1377–1416, doi: 10.1175/1520-0477(1992)073⟨1377:TCTCOR⟩2.0.CO;2.

Webster, P. J. and Stephens, G. L. (1980). Tropical upper-tropospheric extended clouds: Inferences from winter MONEX. *J. Atmos. Sci.*, **37** (**7**), 1521–1541, doi: 10.1175/1520-0469(1980)037⟨1521:TUTECI⟩2.0.CO;2.

Welch, R. M. and Wielicki, B. A. (1989). Reflected fluxes for broken clouds over a Lambertian surface. *J. Atmos. Sci.*, **46** (**10**), 1384–1395, doi: 10.1175/1520-0469(1989)046⟨1384:RFFBCO⟩2.0.CO;2.

Wien, W. (1896). Über die Energievertheilung im Emissionsspectrum eines schwarzen Körpers. *Annalen der Physik*, **294** (**8**), 662–669, doi: 10.1002/andp.18962940803.

Wilks, D. S. *Statistical methods in atmospheric sciences: An introduction*. Academic Press, San Diego, California, (1995).

Wissmeier, U., Buras, R., and Mayer, B. (2013). paNTICA: A fast 3D radiative transfer scheme to calculate surface solar irradiance for NWP and LES models. *J. Appl. Meteor. Climatol.*, **52** (**8**), 1698–1715, doi: 10.1175/JAMC-D-12-0227.1.

Wood, R. (2012). Stratocumulus clouds. *Mon. Wea. Rev.*, **140** (**8**), 2373–2423, doi: 10.1175/MWR-D-11-00121.1.

Wood, R. and Hartmann, D. L. (2006). Spatial variability of liquid water path in marine low cloud: The importance of mesoscale cellular convection. *J. Climate*, **19** (**9**), 1748–1764, doi: 10.1175/JCLI3702.1.

World Meteorological Organization. *International Cloud Atlas – Manual on the observation of clouds and other meteors*. WMO, (2017).

Wu, X. and Liang, X.-Z. (2005). Radiative effects of cloud horizontal inhomogeneity and vertical overlap identified from a monthlong cloud-resolving model simulation. *J. Atmos. Sci.*, **62** (**11**), 4105–4112, doi: 10.1175/JAS3565.1.

Yang, P., Liou, K. N., Wyser, K., and Mitchell, D. (2000). Parameterization of the scattering and absorption properties of individual ice crystals. *J. Geophys. Res.*, **105** (**D4**), 4699–4718, doi: 10.1029/1999JD900755.

Zdunkowski, W., Trautmann, T., and Bott, A. *Radiation in the atmosphere – A course in theoretical meteorology*. Cambridge University Press, Cambridge, UK, (2007).

Zhang, X., Liang, S., Wang, K., Li, L., and Gui, S. (2010). Analysis of global land surface shortwave broadband albedo from multiple data sources. *IEEE Journal of Selected Topics in Applied Earth Observations and Remote Sensing*, **3** (**3**), 296–305, doi: 10.1109/JSTARS.2010.2049342.

Zhao, M. and Austin, P. H. (2005). Life cycle of numerically simulated shallow cumulus clouds. Part I: Transport. *J. Atmos. Sci.*, **62** (**5**), 1269–1290, doi: 10.1175/JAS3414.1.

Zhong, W., Hogan, R. J., and Haigh, J. D. (2008). Three-dimensional radiative transfer in midlatitude cirrus clouds. *Q. J. R. Meteorol. Soc.*, **134** (**630**), 199–215, doi: 10.1002/qj.182.

Zinner, T., Marshak, A., Lang, S., Martins, J. V., and Mayer, B. (2008). Remote sensing of cloud sides of deep convection: Towards a three-dimensional retrieval of cloud particle size profiles. *Atmos. Chem. Phys.*, **8** (**16**), 4741–4757, doi: 10.5194/acp-8-4741-2008.

Zuidema, P. and Evans, K. F. (1998). On the validity of the Independent Pixel Approximation for boundary layer clouds observed during ASTEX. *J. Geophys. Res.*, **103** (**D6**), 6059–6074, doi: 10.1029/98JD00080.

Acknowledgements

First of all I would like to thank my both supervisors Prof. Dr. Bernhard Mayer and Prof. Dr. George Craig for giving me the opportunity and providing me with the funding to work on such an exciting and challenging research topic. I would further like to thank Prof. Dr. Bernhard Mayer for multiple insightful discussions and technical assistance regarding *libRadtran*. I am extremely grateful for having been offered a chance to engage myself as a teaching assistant, since I enjoy sharing knowledge with others. I would furthermore like to thank Prof. Dr. George Craig for a highly valuable and encouraging discussion at intermediate stage of this work.

I greatly thank my colleague Dr. Fabian Jakub for providing me with the UCLA-LES cloud field data sets as well as for several fruitful discussions, which gave me various new ideas − some of them were crucial for this thesis. I further thank Dr. Sophia Schäfer and Prof. Dr. Robin Hogan for the cirrus cloud data and Dr. Tobias Zinner for the cumulonimbus cloud data. Thanks to Dr. Ulrich Blahak and Dr. Jon Shonk, who shared some useful insights on subgrid cloudiness and cloud overlap issues with me.

I thank Dr. Carolin Klinger and Dr. Gerard Kilroy for their perceptive comments on an earlier version of the first ACP publication, which is an important part of this thesis. I similarly thank Dr. Audine Laurian and Mihail Manev for proofreading the drafts of the second and third publication, which as well constitute the major part of this work. I further thank Gregor Möller and Zala Mojca Jerman Kuželički for grammarly checking the thesis abstract − especially the German version.

Next, I wish to thank master students of the course "Clouds: Microphysics and Convection" that I was teaching for three consecutive years. I was constantly looking forward to coming to the class and discussing all sort of problems with you. I would concurrently like to thank both course lecturers and the previous teaching assistant, namely Dr. Tobias Zinner, Prof. Dr. Markus Rapp and Dr. Linda Forster, who all the time kindly advised me on any question. Special thanks to bachelor student Ilona Lerner whom I supervised and Annette Jungblut who brought her to me. I always enjoyed helping and guiding you. Thanks also to many other inspiring MIM researchers.

I would further like to thank the entire tropical cyclone research group at MIM, which I was part of during my master thesis studies. I especially want to thank my former supervisor Prof. Dr. Roger Smith and colleague Dr. Gerard Kilroy for showing me support when most needed.

I wish to acknowledge Waves To Weather (W2W) project for organizing many internal

conferences and workshops as well as other W2W scientists − some of you are really doing an amazingly inspiring science. Many thanks to Dr. Robert Redl for the IT support. Thanks also to Dr. Tobias Selz, who was ready to help me with the ICON model, perhaps this initiated collaboration will be realized one day.

Special thanks to my further doctoral committee members − Prof. Dr. Ralf Bender and Prof. Dr. Andreas Burkert.

I acknowledge Marko Korošec Weather Photography (www.markokorosec.net) for the stunning thunderstorm photo.

I further thank my awesome Slovene meteorology buddies for general advice − Dr. Lina Boljka, Dr. Žiga Zaplotnik and Aljoša Slameršak. I'm happy seeing us reuniting and I'm looking forward to our future joint work experiences. I similarly thank the entire team at Slovenian Environment Agency for providing me a friendly and cooperative work environment during the final phase of dissertation writing.

Finally, I would like to thank my dearest friends and family for their vital support and all free-time adventures!

The research leading to these results has been done within the subproject "B4: Radiative heating and cooling at cloud scale and its impact on dynamics" of the Transregional Collaborative Research Center SFB/TRR 165 "Waves To Weather" funded by German Research Foundation (DFG).